Diese Dissertation haben begutachtet

Prof. Dr. Ulrich Schubert

Prof. Dr. Silke Bühler-Paschen

DISSERTATION

Nanostructured Transition Metal Silicides

ausgeführt zum Zwecke der Erlangung des akademischen Grades eines Doktors der Naturwissenschaften unter der Leitung von

O.Univ.Prof. Dipl.-Ing. Dr.rer.nat. Ulrich Schubert

E165

Institut für Materialchemie

eingereicht an der Technischen Universität Wien

Fakultät für Technische Chemie

von

Van An Du

Mat.Nr. 0727830

Gassergasse 29/8, 1050 Wien

Wien, am 11. April 2011

"I could tell you my adventures – beginning from this morning", said Alice a little timidly: "but it's no use going back to yesterday, because I was a different person then."

"Explain all that", said the Mock Turtle.

"No, no! The adventures first", said the Gryphon in an impatient tone: "explanations take such a dreadful time."

– From *"Alice in Wonderland"* by Lewis Carroll (1865) –

Acknowledgements

During my "life at the university", I met numerous people who have been great company: they made me laugh, shared a friendly chat (sometimes for hours), spent a lot of time with me in courses and on writing reports, taught me how to work in the lab and with all the fancy instruments and how to journalise my findings (or experiments which did not work out as expected....very, very often), how to read and write scientific articles and how to present my work and eventually, they opened my mind towards such wisdoms as: never be afraid to try something new (or again).

First of all, I thank Prof. Schubert, who gave me the opportunity to work in his group during my thesis, for his support and lots of freedom for all my scientific activities: a really pleasant atmosphere without too much pressure helped to develop my appreciation for independent work.

Prof. Bühler-Paschen I thank for her willingness to serve as the second examiner of my thesis.

Without the help of the following people, major parts of this work would not have been possible:

- the USTEM staff: Sabine Schwarz, Lawrence Withmore, Michael Stöger-Pallach and Johannes Bernardi, who helped me to operate the TEM and EDX.
- Michael Puchberger, who never declined to help characterise my samples by NMR, but often complained afterwards (rightfully so, I have to admit).
- Phillip Baloh, who performed some of the Raman measurements and Bernhard Zachhuber, who offered us to use the instrument.
- the ever fearless Stefan O. Baumann, without whom some single-crystals would have never been measured and solved and Majka Bendová, who shared this surely pleasurable and exciting task with him.
- Andrey Sidorenko, who performed SQUID measurements and tried to introduce me to the "world of magnetism".
- Silvia Gross, who invested a lot of her time into the XPS analyses.
- Christina Artner, Christian Maurer, Berthold Stöger and Gerhard Wieser, who performed powder XRD measurements and Johannes Zbiral, who carried out the

X-Ray fluorescence measurements.

- Gregor Stipicic, who introduced me to computational chemistry.
- Marcello Rigutto, who was a fantastic mentor outside of university.
- all the people at Shell research center Amsterdam I had the pleasure to work with: Arend-Jan van Welsens (DBT tests), Ali Azghay (catalyst preparation), Jandirk Dortmundt, Gerrt Bakker (TPR and $SiEt_4$ experiments), Marco de Ridder (TEM and EDX).

To my (*former*) colleagues Angelika, Bernhard (with his special kind of humour), Christian M. (with his enthusiasm for doing things which noone else likes to do), Christine A. (with her delightful habit of delivering chocolate and the newest gossip to me), *Christian Mar.*, *Christoph L.*, *Christoph R.*, *Claudia*, *Denisa*, *Denise*, *Doris*, *Fatmir*, *Giedrius*, Harald, Hongzhi (Dankesch!), Jakob (for sharing the lab and office), Jasmin (for being the other German), *Jingxia*, Maia, Majka, Matthias, Marco (despite his constant use of sign language and because of his constant availability for after work beer), *Marina*, Melitta, Michael, *Mirka*, *Mohsin*, *Nele*, *Phillip*, *Robert L. (the best bench-mate ever)*, Robert P., Rupali, Rupert (for repairing everything and his attempts to speak "Hochdeutsch" with me), Sarah, *Simas*, *Sorin*, *Stefan B. (for being an "excellent" reminder)*, *Stefan E.*, Stephan R., *Stephan K.* and Sven: you all made my time here really enjoyable.

Thanks to Elmar and Isabella, who did a great job during their stay in our lab.

Thanks also go to my "non-chemist" friends, especially Peter who successfully demonstrated that a real mathematician is also able to socialise (even better than me). Andi, Tobi M. and Martin from my times in Ulm: meeting you always makes me feel five years younger.

To my mother and father: I really appreciate your support throughout my whole studies and that you learned to accept the open mind of your daughter, although I am always too many kilometres away from you.

This work is dedicated to you, Gregor. You motivated me to be a researcher and you took your time for long discussions (even in our free time). Thank you for your love; with you my life is perfect.

Kurzfassung

Die Anwendbarkeit verschiedener Ausgangsverbindungen für die Bildung von Übergangsmetallsilizid-Nanopartikeln, verteilt in einer amorphen Matrix, und deren Verwendung in der Hydrodesulfurierung von Dibenzothiophen werden untersucht.

Reaktion von Hexamethylphosphortriamid (HMPA) mit *cis*-$Fe(CO)_4(SiCl_3)_2$ führt zur Bildung des neuen Komplexes $[SiCl_3(HMPA)_3]^+$ $[Fe(CO)_4SiCl_3]^-$. Aus der Thermolyse von *cis*-$Fe(CO)_4(SiCl_3)_2$ resultiert die neue Verbindung $Fe_2(CO)_6(\mu_2{-}SiCl_2)_3$. Für beide Reaktionen werden Dichtefunktionaltheorie (DFT) Rechnungen zur Aufklärung möglicher Reaktionsschritte verwendet.

Die ^{29}Si NMR chemischen Verschiebungen von 41 Silizium-haltigen Verbindungen (14 tetra-, 10 penta- und 17 hexakoordiniert) werden mithilfe von DFT und dem "gauge including atomic orbital" (GIAO) Formalismus berechnet und mit experimentellen Werten verglichen. Das hybride B3LYP Funktional, das "generalised gradient approximation" (GGA) Funktional BPW91 and das meta-GGA Funktional HCTH407 werden in Verbindung mit den Basissätzen 6-31G(d,p) und 6-311+G(2d) und einem lokal dichten Basis Satz (6-311G+(2d) für Si, 6-31G(d,p) für alle anderen Atomen) angewendet. Das theoretische Modell HCTH407/6-311+G(2d) arbeitet in dieser Studie durchgängig am Besten.

Es wird gezeigt, dass bei der thermischen Zersetzung von auf Siliziumdioxid adsorbiertem $Co(CO)_4SiCl_3$ in einer Wasserstoffatmosphäre anstatt Kobaltsilizidnanopartikeln, metallische Kobaltnanopartikel bedeckt von einer Co_2SiO_4/CoO Hülle gebildet werden. Die Übertragung auf andere Trägermaterialien, wie Graphit oder Aktivkohle, führt zu Kobaltnanopartikeln. Der Versuch, Kobaltnanopartikel verteilt in Siliziumdioxid mithilfe eines Sol-Gel Prozesses zu synthetisieren, resultiert in $CoSiO_4$ und CoO.

Die Thermolyse von linearem Poly(ferrocenylsilan) bei 1000°C und Poly[dimethylsilyl)ferrocenyldiacetylen] bei 850°C, führt zu weichmagnetischen Nanopartikeln, die gleichmäßig in einer SiC/C Matrix verteilt sind. Sowohl die durchschnittliche Größe der gebildeten Nanopartikel (sie liegt zwischen 10 und 100 nm) als auch die Größenverteilung hängt von der Wahl des Polymers und den Thermolysebedingungen ab. Die magnetischen Eigenschaften der Nanopartikel werden als Funktion ihrer Grösse mithilfe von SQUID-Messungen analysiert. Die kleinsten Fe_3Si Nanopartikel (10–30 nm) sind Nanopartikel mit einer einzelnen magnetischen Domäne.

Weitere Thermolyseexperimente mit Eisen-oder Kobaltcarbonyl-Fragmenten koordinierten Poly[(dimethylsilylen)diacetylen] und einer Mischung aus $Mn_2(CO)_{10}$ und Poly-[(dimethylsilylen)diacetylen führen jeweils zu Fe_3Si-, Co_2Si/Co- und Mn_5Si_3-Nanopartikeln, die ebenfalls gleichmäßig in einer SiC/C Matrix verteilt sind. SQUID Messungen von Co_2Si/Co zeigen ferromagnetisches Verhalten in einem Temperaturbereich von 3–300 K.

Mit den synthetisierten Nanokompositen werden Hydrodesulfurierungstests von Dibenzothiophen durchgeführt. Kinetische Studien zeigen, dass das durch einen Sol-Gel Prozess erhaltenes Co_2SiO_4/CoO am besten von allen eingesetzten Katalysatoren arbeitet und eine direkte Entschwefelungsroute bevorzugt wird.

Es werden verschiedene Metalle auf Aluminiumoxid (Kobalt, Nickel, Mangan und Molybdän) mit Tetraethylsilan bei 400°C behandelt. Diese Syntheseroute wandelt das inaktive molybdänhaltige Material in einen aktiven Katalysator für die Hydrierung von Ethylen um. Weitere Wasserstoffentschwefelungstests von Dibenzothiophen zeigen eine verbesserte Umsetzung mit einem Faktor von 1,2–2 im Vergleich zu den unbehandelten Materialien.

Abstract

Applicability of different single-source precursors for the formation of transition metal silicide nanoparticles in an amorphous matrix and their application in hydrodesulphurisation of dibenzothiophene are investigated.

Addition of excess hexamethylphosphoric triamide (HMPA) to *cis*-$Fe(CO)_4(SiCl_3)_2$ leads to the formation of the new complex $[SiCl_3(HMPA)_3]^+$ $[Fe(CO)_4SiCl_3]^-$. Thermolysis of *cis*-$Fe(CO)_4(SiCl_3)_2$ results in the formation of the new compound $Fe_2(CO)_6(\mu_2\text{-}SiCl_2)_3$. Density functional theory (DFT) calculations are carried out for both reactions to elucidate possible reaction steps.

^{29}Si NMR chemical shifts of 41 silicon-containing compounds (14 tetra-, 10 penta- and 17 hexacoordinated) are calculated employing DFT, using the gauge including atomic orbital (GIAO) formalism, and compared to experimental values. The hybrid B3LYP functional, the generalised gradient approximation (GGA) functional BPW91 and the meta-GGA functional HCTH407 are used in conjunction with the 6-31G(d,p) and the 6-311+G(2d) basis set and a locally dense basis set (6-311G+(2d) on Si, 6-31G(d,p) on all other atoms). The HCTH407/6-311+G(2d) level of theory consistently performs best in this study.

Evidence is provided that thermal decomposition of $Co(CO)_4SiCl_3$ adsorbed on silica in a hydrogen atmosphere results in the formation of metallic cobalt nanoparticles covered with a Co_2SiO_4/CoO shell instead of cobalt silicide nanoparticles. The application of other supporting materials such as graphite or charcoal leads to cobalt nanoparticles. The attempt to synthesise cobalt nanoparticles in silica by a sol-gel process results in $CoSiO_4$ and CoO.

Thermolysis of linear poly(ferrocenylsilane) at 1000°C and poly[dimethylsilyl)ferrocenyldiacetylene] at 850°C results in soft magnetic nanoparticles, well distributed in a SiC/C matrix. Both the average size of the formed nanoparticles (between 10 and 100 nm) and the size distribution depend on the choice of polymer and the thermolysis conditions. The magnetic properties of the nanoparticles are analysed as a function of their size by SQUID-measurements. The smallest Fe_3Si nanoparticles (10–30 nm) are single magnetic domain particles.

Further thermolysis experiments with poly[(dimethylsilylene)diacetylene] to which iron and cobalt carbonyl moieties are coordinated, and a mixture of $Mn_2(CO)_{10}$ and poly[(di-

methylsilylene)diacetylene] result in Fe_3Si, Co_2Si/Co and Mn_5Si_3 nanoparticles, respectively, which are also well-distributed in a SiC/C matrix. SQUID measurements of Co_2Si/Co nanocomposite reveal ferromagnetism in a temperature range of 3–300 K.

Hydrodesulphurisation of dibenzothiophene using the synthesised nanocomposites as catalysts are performed. Kinetic studies show that the sol-gel process derived Co_2SiO_4/CoO performs best and all catalysts favour a direct desulphurisation route.

Tetraethylsilane treatment of different metals supported on alumina (cobalt, nickel, manganese or molybdenum) at 400°C is performed. This preparation route turns the inactive molybdenum-containing material into an active catalyst towards ethylene hydrogenation. Further hydrodesulphurisation tests with dibenzothiophene reveal an improvement of the conversion by factors of 1.2–2 as compared to the untreated materials.

Parts of this work have been published

1. "Cleavage of an iron-silicon bond by hexamethylphosphoric triamide: synthesis and characterization of $[SiCl_3(HMPA)_3]^+[Fe(CO)_4SiCl_3]^-$", Du, V. A.; Baumann, S. O.; Stipicic, G. N.; Schubert, U. *Zeitschrift für Naturforschung Section B - A Journal of Chemical Sciences*, **2009**, *64b*, 1553–1557.

2. "Formation of the silylene-bridged complex $Fe_2(CO)_6(\mu_2{-}SiCl_2)_3$ from *cis*-$Fe(CO)_4(SiCl_3)_2$: an experimental and computational study", Du, V. A.; Stipicic, G. N.; Bendová, M.; Schubert, U. *Monatshefte für Chemie - Chemical Monthly*, **2010**, *6*, 671–675.

3. "Re-investigation of the thermal decomposition of $Co(CO)_4SiCl_3$ adsorbed on silica", Du, V. A.; Gross, S.; Schubert, U. *Chemical Communications*, **2010**, *46*, 8549–8551.

4. "^{29}Si NMR shielding calculations employing density functional theory, with focus on hypervalent silicon compounds", Du, V. A.; Stipicic, G. N.; Schubert, U. *European Journal of Inorganic Chemistry*, **2011**, *accepted*.

Parts of this work have been submitted for publication

5. "Iron silicide nanoparticles in a SiC/C matrix from organometallic polymers: characterization and magnetic properties", Du, V. A.; Sidorenko, A.; Paschen, S.; Schubert, U.; **2011**, *submitted*.

Abbreviations

BE	binding energy
BET	Brunauer, Emmett and Teller
BJH	Barrett, Joyner and Halenda
B3LYP	Becke 3 parameter Lee-Yang-Parr density functional
BPW91	Perdew-Wang 91 gradient correlation functional
n-BuLi	*n*-butyllithium
Cp	cyclopentadienyl
CVD	chemical vapour deposition
CVT	chemical vapour transport
DBT	dibenzothiophene
DDS	direct desulphurisation
ΔG_V	change in free energy per unit volume
DFT	density functional theory
2Θ	diffraction angle
ECOTA	environmental catalyst optimising testing apparatus
EDX	energy-dispersive X-ray spectroscopy
emu	electromagnetic unit
Fc	ferrocene
FC	field-cooled
γ	interfacial free energy
GGA	generalized gradient approximation
GPC	gel permeation chromatography
HAADF	high-angle annular dark-field imaging
H_c	coercive force
HCTH	Hamprecht, Cohen, Tozer and Handy GGA exchange-correlation functional
HDS	hydrodesulphurisation
HMPA	hexamethylphosphoric triamide
HYD	prehydrogenation
IFQC	International Fuel Quality Center
IUPAC	International Union of Pure and Applied Chemistry
λ	wavelength
LDBS	locally dense basis set
LPCVD	low pressure chemical vapour deposition

MFC	mass flow controllers
M_n	number average molecular weight
M_r	remanent magnetisation
M_s	saturation magnetisation
MS	mass spectrometer
M_w	weight average molecular weight
MOSFET	metal oxide semiconductor field effect transistor
NMR	nuclear magnetic resonance
Oe	Oersted
PVI	pore volume impregnation
RT	room temperature
SEC	size exclusion chromatography
SCR	self consistent renormalisation
STEM	scanning transmission electron microscopy
SQUID	superconducting quantum interference device
TEOS	tetraethoxysilane
T	Tesla
T_B	blocking temperature
THF	tetrahydrofurane
TMEDA	tetramethylethylenediamine
TMS	tetramethylsilane
TNPS	ditertiononylpentasulphid
VLS	vapour liquid solid
VSS	vapour solid solid
UV/Vis	ultraviolet/visible
wt	weight
XPS	X-ray photoelectron spectroscopy
XRD	X-ray diffraction
XRF	X-ray fluorescence
ZFC	zero-field-cooled

Contents

1 Introduction

1.1 Nanostructured Materials

The immense interest in nanostructured materials increased steadily over the last decade. The terminology of "nanostructure" originates from structures with size scales in a range of 1–100 nm. The progress in synthetic procedures and suitable analytic methods increased rapidly within the recent years. Chemistry, physics, biology and medicine are going hand in hand to synthesise and investigate new materials with novel properties and applications. There is a great variety of classes and forms of those structures with reduced size. They can be distinguished by the number of their dimensions: zero (clusters, particles), one (*e.g.* nanowires) and two (layers).

According to R. W. Siegel, the vast collection of nanostructured materials features unifying and characteristic attributes, which have a decisive impact on their properties: atomic domains are defined to be smaller than 100 nm and have significant boundaries, while interaction between the atoms in the particular domains occurs.[1]

Radical changes in the physical properties of materials are a consequence of the size reduction. An inspiring and traditional quote, which describes the possibilities that open up for potential applications is R. P. Feynman's *"There is plenty of room at the bottom"*.[2]

Nanoparticles can be classified according to three different morphologies. Isolated particles with nanoscaled diameter are notated as type **A** (Figure 1.1). To form type **A** nanoparticles, aggregation has to be avoided, which can be achieved by organic molecules (*e.g.* thioles, carboxylates, surfactants) attached to the particle surfaces. For instance, well-separated iron nanoparticles in ferrofluids can be stabilised by modification with tetramethylammonium hydroxide.[3] Nanoparticles covered with a shell of another material are known as core-shell particles (type **B**). Another intermediate phase is characterised by nanoparticles distributed in a matrix which are known as

nanocomposites, type **C**. In both cases, the interaction of the particles is inhibited. The array of non-interacting and separated particles is different from already known bulk materials.

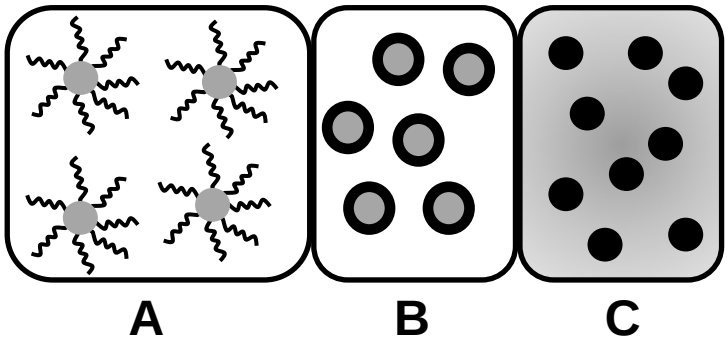

Figure 1.1: Schematic representation of different morphologies.[4]

The focus of this work will be on two interesting properties of metal-containing nanocomposites: the magnetic behaviour of the obtained transition metal silicide nanocomposites and their applicability as a heterogeneous catalyst.

The correlation between morphology and magnetic properties has been studied to great extent.[3–8] The superparamagnetism of nanoparticles of type **A**, where the interaction of the particles is sufficiently weak, is explained by the Néel-Brown theory,[9,10] which is supported by experimental evidence obtained by magnetisation measurements of individual ferromagnetic nanoparticles (10–39 nm).[11] It is possible to tune materials between superparamagnetic, soft magnetic and regular permanent magnetic behaviour. For instance, information storage technology benefits from the manipulation of the coercivity field in magnetic nanomaterials.[12] Not only magnetic recording is an interesting application, but also high frequency electronics, magnetic refrigerants, colour imaging and bioprocessing.[13,14]

Apart from their magnetic properties, applications of nanoparticles dispersed in a matrix (type **C**) in heterogeneous catalysis continue to capture the imagination of the research community. The majority of employed catalysts consists of nanostructured metal- or metal oxide particles dispersed in a supporting material with high surface area (*e.g.* SiO_2, Al_2O_3, ZrO_2, charcoal). Intense studies have been carried out on catalysts in the automotive industry, which are built to oxidise hydrocarbons and carbon monoxide to carbon dioxide and to reduce nitrogen oxide to nitrogen. The supporting material is impregnated with Pt and Rh nanoparticles.[15,16] The size of the nanoparticles and the composition of the catalyst strongly correlates with the observed activity

and selectivity.[17] There are numerous catalysts for diverse reactions and the focus of the present work is on hydrodesulphurisation reactions (see Section 1.5).

1.2 Transition Metal Silicides

Iron Silicides

The interest in the synthesis of iron silicides stems from their promising physical properties.[18] Different phases in the iron silicide system (*i.e.* FeSi, β-$FeSi_2$, Fe_3Si and the metastable Fe_2Si, α-$FeSi_2$, Fe_5Si_3)[19] are known (Figure 1.2).

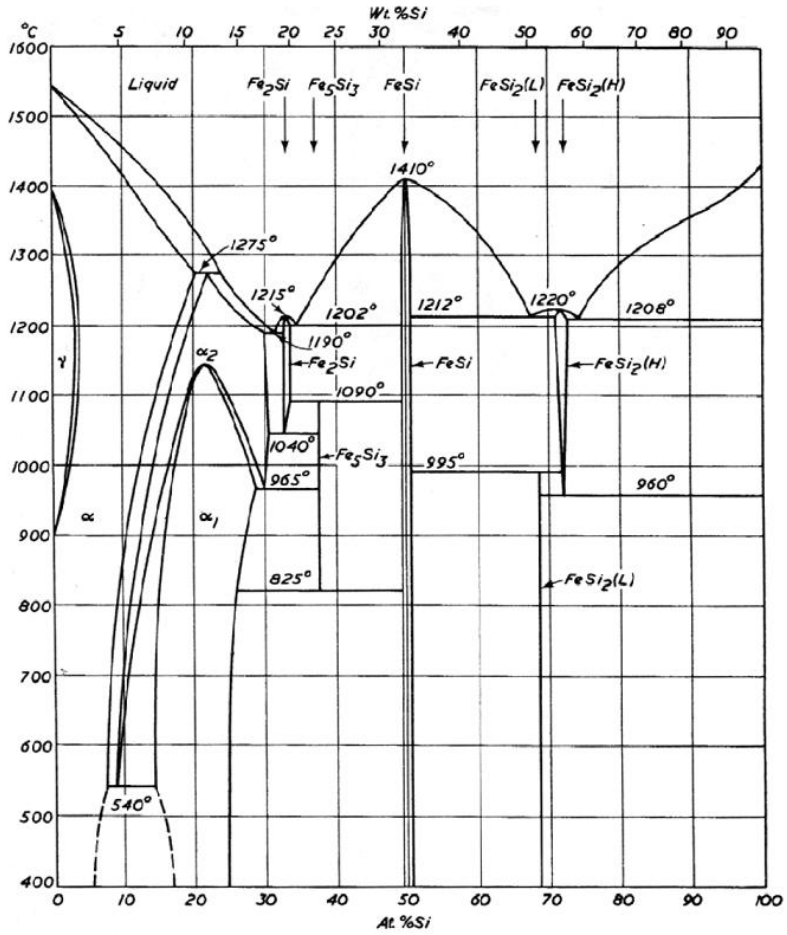

Figure 1.2: Fe–Si phase diagram.[19]

According to the phase diagram FeSi, β-$FeSi_2$ and Fe_3Si are stable at room temperature, whereas Fe_2Si, α-$FeSi_2$ and Fe_5Si_3 are metastable. During solid state reactions

of the Fe–Si couple, FeSi has been predicted to form as the first silicide because of its favourable change in free energy per unit volume. The other iron silicides are produced after the formation of FeSi. They exhibit metallic, semiconducting (α-$FeSi_2$)[20] or insulating (β-$FeSi_2$) behaviour, depending on their structure. FeSi is the only known transition metal Kondo insulator,[21] which is a class of heavy-electron compounds exhibiting Kondo lattice behaviour at room temperature, but having an insulating ground state with a narrow energy gap. Owing to the luminescence of $FeSi_2$ with a wavelength ($\sim$1.55 μm) suitable for light emitting diode operation, this compound is potentially interesting for optoelectronic devices.[22] β-$FeSi_2$ is a potential photovoltaic material.[23] Fe_5Si_3 exhibits giant magnetoresistant properties.[24] The iron-rich phases Fe_3Si and Fe_5Si_3 have ferromagnetic properties at room temperature with reported Curie temperatures (T_C) of 799 K[25] and 385 K,[26] respectively. Therefore they are potential materials for spintronics.[27]

The main focus of this thesis will be on the thermodynamically stable Fe_3Si and the metastable Fe_5Si_3 phases.

Fe_3Si crystallises in the DO_3 structure, which is best understood as a substitutional superstructure of α-Fe where a quarter of the Fe-atoms are substituted by Si in a regular way. Two oxidation states of iron are present: Fe(I) and Fe(II). The Fe(I) atoms are eightfold coordinated by Fe(II) and the Fe(I) atoms tetrahedrally coordinated by Fe(II).[28,29] Due to the Si atom being in vicinity of the iron atoms with different oxidation states, an indirect exchange – the so called double exchange mechanism – occurs, which leads to a ferromagnetic arrangement of the spins and the ferromagnetic character of Fe_3Si.[7]

Fe_5Si_3 is isostructural with Mn_5Si_3. The structure is hexagonal, with space group $P6_3/mcm$ and its projection onto the basal plane is depicted in Figure 1.3. The structure consists of two inequivalent sites of Fe. The nearest neighbours of the Fe(I) site are two Fe(I) atoms and their distance is 2.35 Å and Fe(I), Fe(II) has two Si atoms at a distance of 2.35 Å, one Si atom at 2.50 Å and two Si atoms at 2.62 Å as nearest neighbours. Four Fe(I), six Fe(II) and six Si atoms correspond to every unit cell of Fe_5Si_3; therefore the atom ratio of Fe(I):Fe(II) is 2:3 in this material.[28] This compound is stable within a narrow temperature range from 825°C to 1030°C. On this case a double exchange mechanism takes place, leading to ferromagnetism of this material.

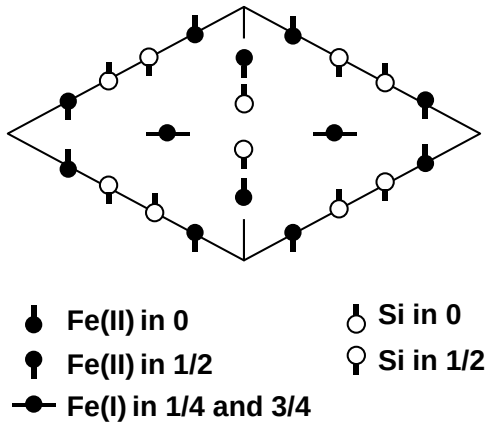

Figure 1.3: The structure of Fe_5Si_3 projected to the basal plane.

Cobalt Silicides

Besides iron as a group VIII element, cobalt is also a promising metal for silicide formation with interesting applications in a variety of research areas. Several intermediate phases have been found in this system: Co_3Si, Co_2Si, CoSi and $CoSi_2$ (Figure 1.4).[30]

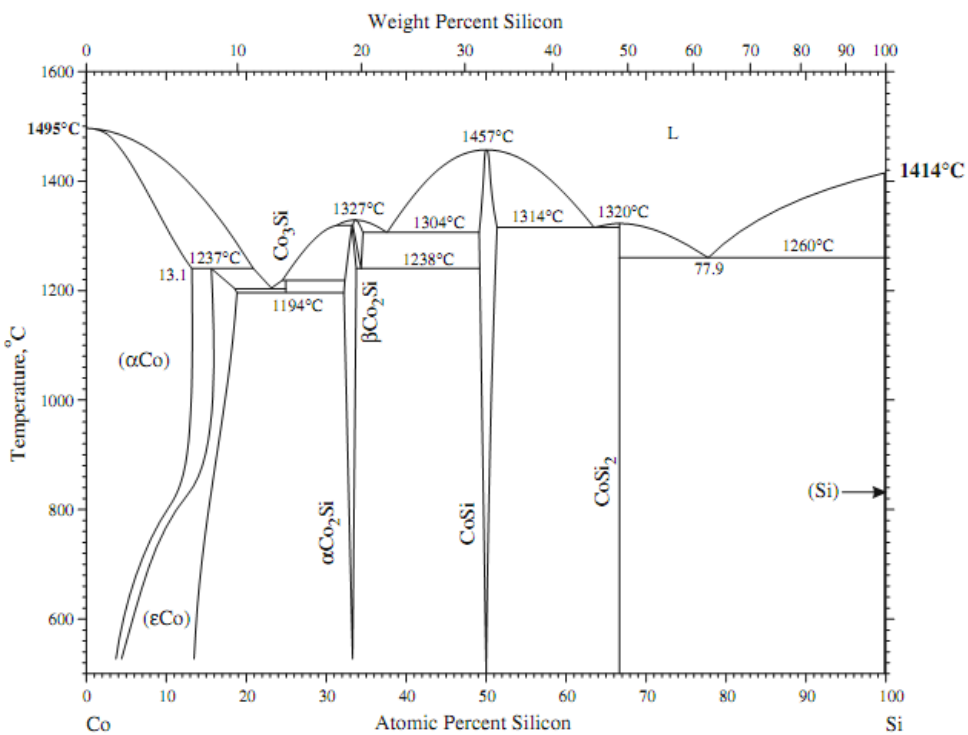

Figure 1.4: Co–Si phase diagram.[30]

$CoSi_2$ can be considered as an excellent material, due to the low mismatch of -1.2% with the Si lattice, which leads to high thermal stability and resistivity. Additionally, this property allows epitaxial growth on silicon substrates.[31] It can also be used for cold cathode materials.[32] An attractive size reduction of a metal oxide semiconductor field effect transistor (MOSFET) device has been reported by the group of Mantl[33] just by changing of the common doping material silicon to $CoSi_2$. The $CoSi_2$ phase has a superconductive transition temperature of 1.4 K and is Pauli-paramagnetic.[34] Co_2Si has also been reported to be paramagnetic.[35] The crystal structure of Co_2Si is orthorhombic with space group *Pnam.*[36] CoSi bulk material is diamagnetic and can be turned into a ferromagnetic compound by size reduction to nanowires.[37]

In a recent communication, Liang *et al.* claimed to have synthesised CoSi particles on a silica support by thermal decomposition of adsorbed $Co(CO)_4SiCl_3$, which exhibit remarkable catalytic activity towards naphthalene hydrogenation.[38] In the present work we show that this procedure results in the formation of metallic cobalt nanoparticles instead covered with a Co_2SiO_4/CoO shell, which might contain the catalytically active phase (see Section 2.4.1).[39]

Manganese Silicides

The composition of manganese silicides covers a wide range of different and potentially defect phases.[40] MnSi has attracted great attention, which is a weak itinerant-electron magnet with a cubic crystallographic structure (lattice parameter a = 0.4561 nm) at room temperature.[41] It is a weak ferromagnetic compound with a Curie temperature of T_C = 29.5 K. There are two basic theories of magnetism: localised moment theory and itinerant electron theory, which are explained by Heisenberg[42,43] and Stoner[44] models, respectively. They are not applicable for intermediate systems (*e.g.* MnSi), which are called near or weak ferromagnets and are described by self consistent renormalisation theory (SCR).[45]

The magnetic behaviour changes in the epitaxially induced strain in MnSi films. Varying the induced pressure leads to a change of the magnetic structure.[46] Apart from that phase, Mn_5Si_3 has been studied regarding its change of magnetic properties induced by carbon doping.[47] Mn_5Si_3 exhibits an antiferromagnetic nature (Néel temperature T_N = 90 K), whereas $Mn_5Si_3C_x$ is ferromagnetic for a saturation concentration of x_s = 0.22 and a Curie temperature of T_C = 152 K. The crystal structure of Mn_5Si_3 is

hexagonal with space group $P6_6/mcm$. Furthermore, higher manganese silicide phases do exist: Mn_4Si_7,[48] $Mn_{11}Si_{19}$,[49] $Mn_{15}Si_{26}$,[50] $Mn_{27}Si_{47}$.[51]

1.3 Synthesis of Metal Silicides

Transition metal silicides can be produced by various routes, typical procedures are traditional solid-state reactions, which we do not consider for formation of nanomaterials. Another complex possibility is the use of ion beam induced mixing (IBM) of alternating metal and silicon layers.[52]

The group of Lieber synthesised a transition metal silicide by starting with a backbone of Si nanowires, which was grown using the vapour-liquid-solid (VLS) method and subsequently covered with a thermally evaporated nickel thin film. Heat treatment at higher temperatures induced a solid-state reaction between nickel and silicon leading to NiSi nanowires.[53]

Silicon on Metal Films/Metal on Silicon Substrates

Another possibility is to deposit silane on a metal surface in order to induce metal silicide formation or to react anhydrous metal halides with silicon substrates.

Until present, only one successful synthesis using this procedure has been reported, using a nickel substrate treated with SiH_4 vapour ($NiSi_2$,[54] NiSi,[55–57] Ni_2Si,[54,57,58] Ni_3Si_2,[59] $Ni_{31}Si_{12}$[60] and Ni_3Si[61]). It is intriguing to note that only nickel is able to form nickel silicides by SiH_4 treatment. Besides the nickel silicide nanowires growth, the group of Liang[62] recently published the synthesis of silicide modified nickel catalysts, achieved by simple SiH_4 treatment of nickel metal dispersed in carbon.

A further suitable procedure is metal chloride deposition on a silicon substrate which is known to result in crystalline metal silicide nanowires; for instance, $FeCl_3$ was used for FeSi formation.[63] The application of this method has already led to the successful synthesis of a number of transition metal silicides: CoSi, Co_2Si,[37] FeSi,[63] Fe_5Si_3[64] and $CrSi_2$.[65]

Chemical Vapour Deposition

Extended investigations were carried out to find suitable precursors, such as compounds which act as both metal and silicon source, *i.e.* single-source precursors, as well as mixtures of two species, which separately provide the necessary metal and silicon content. The synthesis of nanostructured transition metal silicides (the focus of the present work is on iron, cobalt and manganese) can be carried out in gas-, liquid- or solid phase. The most striking advantage of using an appropriate molecular precursor is the decrease in necessary reaction temperatures and durations.

Figure 1.5 represents applicable single-source precursors for transition metal silicide formation by the chemical vapour deposition method.

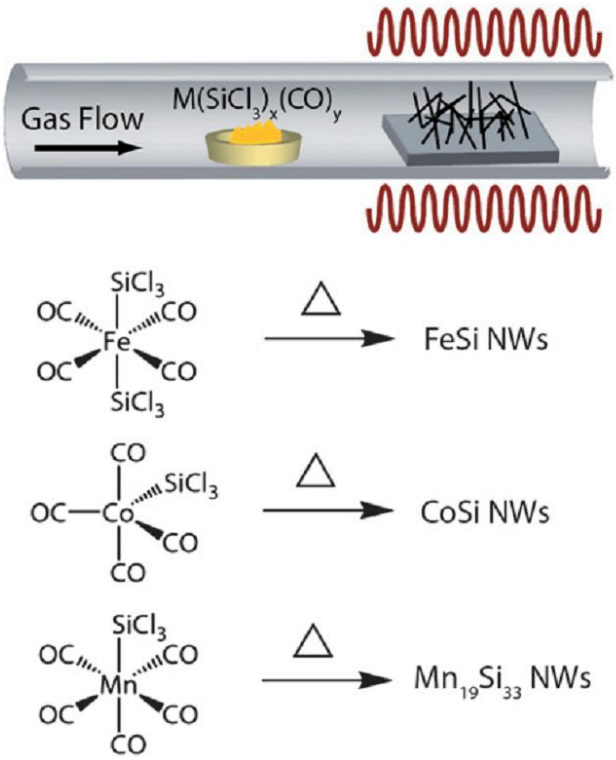

Figure 1.5: Synthesis of metal silicide nanowires using chemical vapour deposition (CVD) of single-source precursors. Single-source precursors are pyrolysed to deliver metal silicide material to the growth substrate.[66]

A demonstrative and illuminating example is the formation of bulk FeSi. This compound can be obtained by sintering the elements in equimolar ratios at 1000°C for 7 d by exclusion of oxygen, whereas iron silicide films were prepared by CVD processes from *cis*-$Fe(CO)_4(SiCl_3)_2$ under much milder conditions. Based on photoelectron spec-

tra and theoretical calculations, Zybill *et al.* proposed intramolecular $SiCl_4$ elimination and concomitant formation of an iron silylene complex as an initial mechanistic step during the generation of iron silicide.[67,68]

A further application of the single-source precursor $Fe(CO)_4(SiCl_3)_2$ is the creation of free standing single-crystal nanowires on a silicon substrate at moderate conditions (750°C for 1 h) under chemical vapour deposition (CVD) conditions (see Figure 1.6).[69] CVD conditions and the use of a substrate apparently have immense influence on the metal silicide formation as will be shown in Section 2.4 of this thesis.

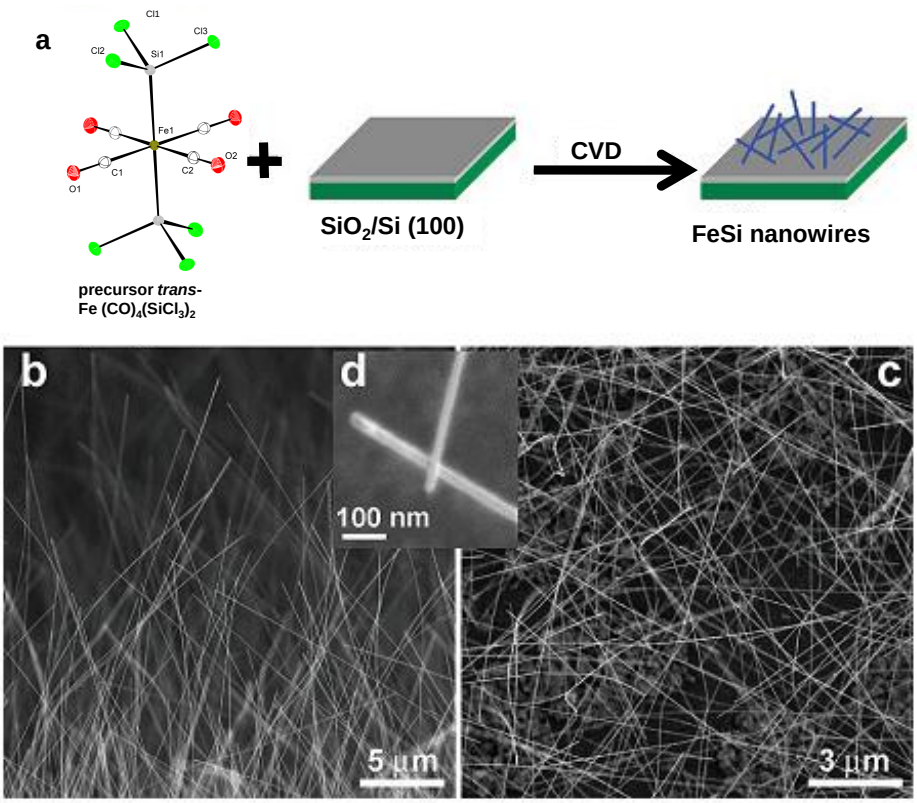

Figure 1.6: (a) FeSi nanowire growth from the single-source precursor *trans*-$Fe(CO)_4(SiCl_3)_2$ by chemical vapour deposition. Representative scanning electron microscope images of FeSi nanowires: (b) over the edge of the growth substrate; (c) over the substrate; and (d) a close up view highlighting the nanowire tips.[69]

It is mandatory that the applied precursors are not allowed to decompose during evaporation. This epitactic process is based on the strong interaction of a volatile compound on a surface and the nucleation in a supersaturated gas phase, which leads to a crystalline product. Another advantage is the easier application of single-source precursors compared to hazardous compounds like $Fe(CO)_5$ and $SiCl_4$. The same procedure can

be applied to obtain CoSi nanowire growth on a silicon substrate, $Co(CO)_4SiCl_3$ delivers cobalt and silicon.[70] Co_2Si, CoSi and $CoSi_2$ film deposition on Pyrex glass by low pressure chemical vapour deposition (LPCVD) in presence of SiH_4 was also successfully performed by Zybill and co-workers.[71] Formation of iron or cobalt silicides was not observed when the same precursor was used for nanoparticle formation (see Sections 2.2.1, 2.1 and 2.4.1).[39,72,73]

That straightforward approach was extended to higher manganese silicide nanowires of Nowotny chimney ladder phase ($MnSi_{2\text{-}x}(MnSi_{1.8})$ by application of $Mn(CO)_4SiCl_3$ as the manganese and silicon source.[74] A Nowotny chimney-ladder structure is of the general formula T_nX_m, where $2 > m/n \geq 1.25$. Further studies on its electronically transport behaviour confirm low resistivity.[75,76]

A more traditional way of metal silicide layer formation is the employment of silicon and metal sources. Classical precursors are metal carbonyls or metal chlorides and silane at low temperature, *e.g.* Zhou's group synthesised nanostructured $TiSi_2$ from $TiCl_4$ and SiH_4.[77]

Nanoparticles can as well be obtained by combining a metal and a silicon source. Dahal *et al.* prepared Fe_3Si nanoparticles in solution by high-temperature reaction of $Fe(CO)_5$ with $SiCl_4$ in the presence of 1,2-hexadecanediol.[78]

Organometallic Polymers

An organometallic polymer consists of a main group or transition metal incorporated in an organic polymer chain. There are different possibilities to attach the metal to the organic unit, either in the main chain or at the side groups. Linear, hyperbranched and dendritic organometallic polymers are also available.

Several organometallic polymers were employed to produce transition metal silicide nanoparticles. FeSi and Fe_3Si particles in SiC were formed by pyrolysis of an ill-defined oligomer or polymer obtained by photochemical reaction of $Fe(CO)_5$ with 2,5-disilahexane. The same procedure was applied to Co_2Si formation by replacement of $Fe(CO)_5$ with $Co_2(CO)_8$.[79] The attachment of volatile metal carbonyl fragments takes place by reaction with Si–H bonds of the 2,5-disilahexane. Colquhoun and his group already used this reaction for $Co(CO)_4(SiH_3)$, $Fe(CO)_4(SiH_3)_2$ and $Mn(CO)_5(SiH_3)$ production; those compounds are suitable for chemical vapour deposition of transition-

metal silicide layers.[80] It was expected that the four Si–H units of the 2,5-disilahexane react to form four Si–M bonds (M = metal). The reaction was monitored by infrared (IR) spectroscopy and it was postulated that two iron carbonyl fragments are bridged by a 2,5-disilahexane group, leaving the ability to polymerise intact, such as depicted in Figure 1.7 (structure **5**).

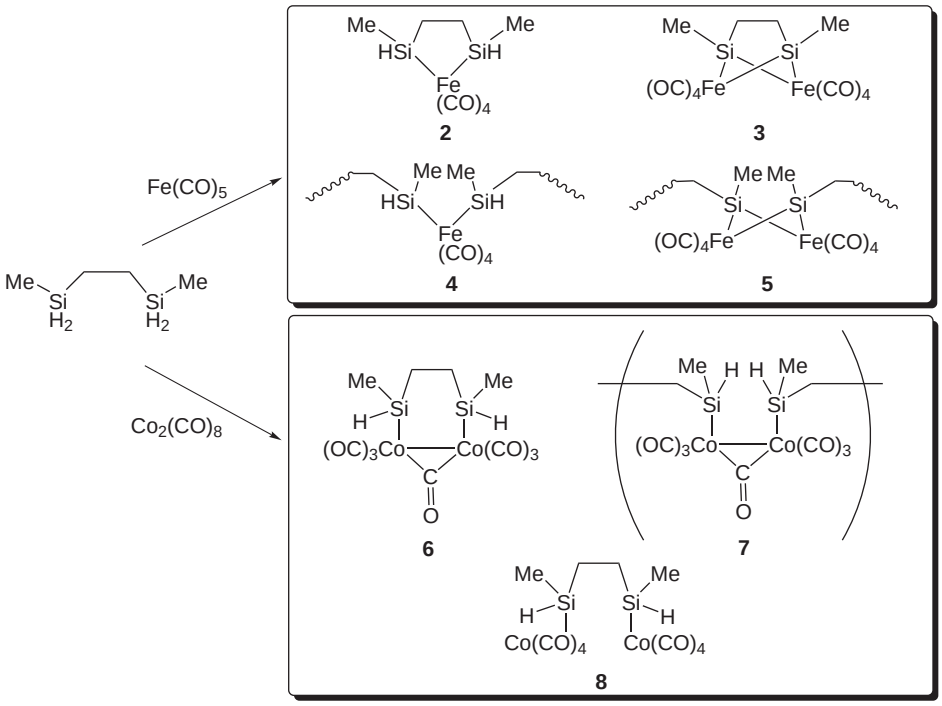

Figure 1.7: Possible reaction product structures for $Fe(CO)_5$ and $Co_2(CO)_8$ with 2,5-disilahexane, respectively. Investigated by elemental analysis and IR spectroscopy.[79]

Thermolysis of that mixture at 1000°C under argon yielded a product, which was investigated by X-ray diffraction (XRD), Raman spectroscopy and transmission electron microscopy (TEM). In the case of $Fe_3Si/FeSi$, formation of nanoparticles of about 10 nm in a $SiC/C/SiO_2$ matrix was observed. Application of the same heat treatment to the cobalt-containing polymer resulted in slightly larger particles of Co_2Si (20 nm).

Furthermore, Corriu's group performed intensive investigations on the reaction of various functional silyl acetylenes with $Co_2(CO)_8$. They obtained a series of corresponding acetylene-cobalt carbonyl complexes.[81] In another work, the chemistry of poly-[(dimethylsilylene)diacetylene] upon pyrolysis was analysed.[82] Based on those results, oligomers of metal containing poly[(silylene)diacetylene] were synthesised[83] (Figure 1.8) and tested for their suitability as precursors. Thermolysis at 1400°C under argon resulted in cobalt silicide-based ceramics.[84]

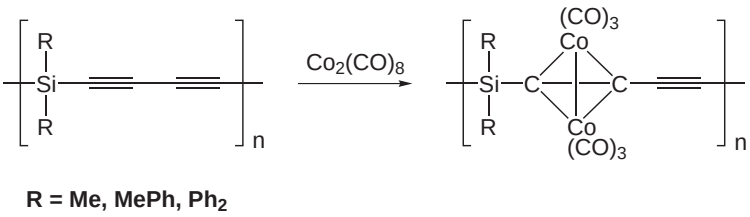

Figure 1.8: Complexation of $Co_2(CO)_8$ with poly[(silylene)diacetylene].[83]

The principle of the attachment of metals to silicon-containing polymers has also been employed for the formation of nickel and nickel silicide nanoparticles by Manners' group.[85] The synthesis of nickel-containing polycarbosilanes (in Figure 1.9, structure **4a**, **4b**) started from reaction of 1-chloro-1-methylsilacyclobutane with lithium acetylides in diethyl ether, resulting in acetylide substituted silacyclobutane, which can be polymerised by ring-opening polymerisation. In the last step of the reaction (thermal or photocatalytical) $[CpNi(CO)]_2$ can bind to the acetylene groups, which yields the nickel and silicon-containing precursor.

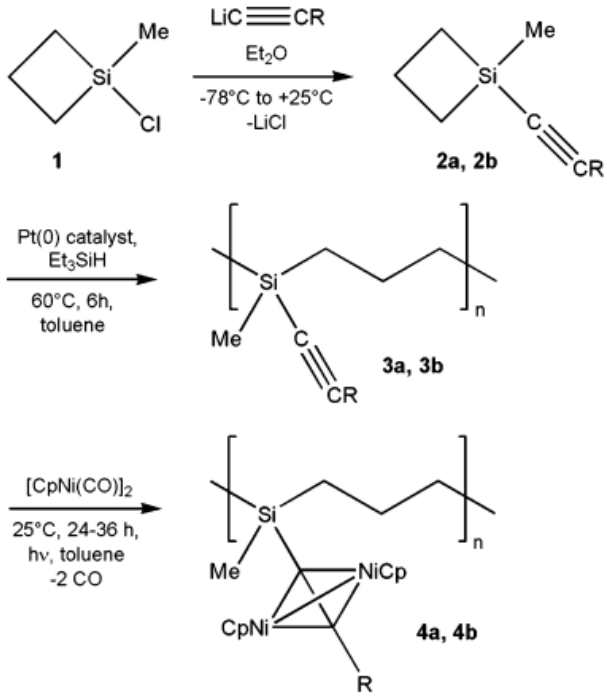

Figure 1.9: Synthesis of nickel-clustered polycarbosilanes with variable molecular weights and two substituents R = phenyl (**a**) and ^{t}butyl (**b**).[85]

Other metal-containing precursors are ferrocenyl-containing polymers. Three of them have already been studied (see Figure 1.10):

- poly[{(dimethylsiloxyl)ferrocenyl}diacetylene] (polymer **A**).
- poly[{(dimethylsilyl)ferrocenyl}diacetylene] (polymer **B**).
- poly(ferrocenylsilane) (polymer **C**).

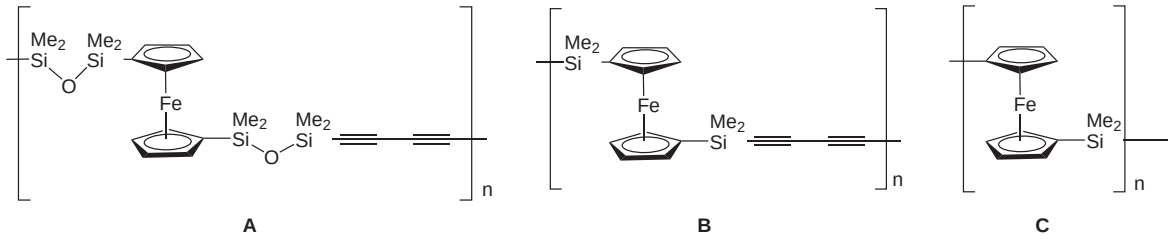

Figure 1.10: Structural formula of the ferrocenyl-containing polymers.

Slow heating of poly[{(dimethylsiloxyl)ferrocenyl}diacetylene] (polymer **A**) under nitrogen resulted in α-Fe particles in a SiC/C matrix, while fast heating led to metastable ferromagnetic Fe_5Si_3 surrounded by a carbon layer.[86]

Pyrolysis of poly[{(dimethylsilyl)ferrocenyl}diacetylene] (polymer **B**; also with SiMePh or $SiPh_2$ groups instead of $SiMe_2$), with a higher Fe:Si ratio, only resulted in $Fe_xSi_yC_z$ phases the composition of which could not be determined.[84]

The pyrolysis of easily accessible linear poly(ferrocenylsilane) (polymer **C**) was extensively investigated.[87,88] Only α-Fe was obtained in these experiments under a nitrogen atmosphere. It has been reported that the magnetic properties of this composite can be tuned between superparamagnetic and ferromagnetic behaviour by control of the pyrolysis conditions, depending on the size of iron nanoclusters homogeneously dispersed throughout the SiC/C matrix.[89] The hyperbranched organometallic polymer derived from spirocyclic-ferrocenophane formed α-Fe particles on thermolysis under nitrogen,[89] but crystalline Fe_3Si under argon.[90] An explanation of this phenomenon was offered by Manners *et al.*:[91] in an argon atmosphere, no nitrogen-mediated pathway for the production of α-Fe nanoparticles along with the formation of Si_3N_4, Fe_4N and Fe_2N is available.

Depending on the desired structure (nanoparticles, nanowires, layers, nanocomposites) the synthetic procedure differs and suitable adapted precursors and techniques are necessary. With the insights gained from research already performed, parameters can be changed leading to the discovery of additional nanomaterials.

1.4 Computational Prediction of ^{29}Si NMR Shieldings

In Section 2.3 of this work, a density functional theory study on the calculation of ^{29}Si NMR shieldings was carried out.

Predicting the observable quantities of nuclear magnetic resonance (NMR) spectra from first principles is of great interest, and numerous methods have been developed for the calculation of nuclear magnetic shielding in molecules[92,93] since the fundamental formulation by Ramsey.[94]

The gauge including atomic orbital (GIAO) approach in conjunction with the coupled Hartree-Fock (CHF) method has been a breakthrough in the field of NMR chemical shift calculations[95] and has been extended to density functional theory (DFT),[96,97] which has proven highly successful as an economic alternative to *ab initio* methods and generally yields useful results, even in more challenging cases such as transition-metal compounds,[98] which are known to exhibit strong correlation effects.[99]

^{29}Si NMR shielding calculations by *ab initio* and DFT methods were used as an accurate tool for the prediction of chemical shifts in tetracoordinated silanes,[100] silane derivatives,[101] silanols[102] and organosiloxanes.[103] Triply bonded compounds such as disilynes (RSi≡SiR) were subject of a computational study by Apeloig *et al.*,[104] where they showed that DFT with the HCTH407[105] functional exhibits a performance comparable to second-order many-body perturbation theory (MP2).[106] Recently, Rankin *et al.* demonstrated that ^{29}Si-^{1}H spin-spin coupling constants in organoalkoxysilanes can also be successfully predicted.[107]

Experimentally, ^{29}Si NMR shifts have the characteristics to display large variations with local structure, involving the first and second shells of their neighbours as pointed out by Heine and co-workers.[100] While common silicon-containing molecules such as *e.g.* silanes, silanols or siloxanes exhibit tetracoordinated silicon atoms, hypervalent (*i.e.* penta- and hexacoordinated) silicon compounds are an entirely different class of compounds. Investigations of the mechanisms of their formation and their structure both in the solid state and in solution (*e.g.* by NMR) has lead to an improved understanding of their properties.[108–110]

1.5 Hydrodesulphurisation

Crude oil used as the basis of refinery processes is a complicated mixture, consisting of hydrocarbons ranging from methane to heavier compounds (alkanes, cycloalkanes and aromatics), other organic compounds which contain nitrogen, oxygen, sulphur and metals (*e.g.* Ni, Cu, V).

Due to the variety of compounds in the crude oil and the high requirements regarding the final product, numerous refinement units are necessary to obtain clean light hydrocarbons (*e.g.* gasoline, kerosene and gasoil). A schematic representation of a typical refinery flow is depicted in Figure 1.11, but evidently, many different configurations exist of that process.

One of the many important steps is hydrodesulphurisation (HDS), whose goal is the removal from sulphur in the petroleum feedstock (see Table 1.1) by reaction with hydrogen in the presence of suitable catalysts. Temperature and pressure influence the conversion yield significantly. The HDS step has to precede the further refinement procedure, due to the subsequent application of expensive noble metals as catalysts, which can be poisoned already by a moderate amount of sulphur-containing compounds. There are also environmental restrictions which allow only a certain amount of sulphur in transportation fuels. In a similar spirit, the formation of SO_2 during combustion, which causes acid rain, forces the reduction of the sulphur content in the oil.[111]

Table 1.1: Composition of the chemical elements in crude oil.[112]

Element	Percent range (%)
Carbon	83–87
Hydrogen	10–14
Sulphur	0.5–6
Nitrogen	0.1–2
Oxygen	0.1–1.5
Metals	< 0.1

Table 1.2: Proportion of the different types of hydrocarbons in crude oil.[112]

Hydrocarbon	Range (%)
Paraffins	15–60
Naphtalenes	30–60
Aromatics	3–30
Asphaltics	remainder

In December 2010, the International Fuel Quality Center (IFQC) published a list ranking countries by low sulphur diesel limits. There is a dramatic reduction in the sulphur limit, nearing 10 ppm (2009) or even further to the "zero"-level (lower than 10 ppm).[113]

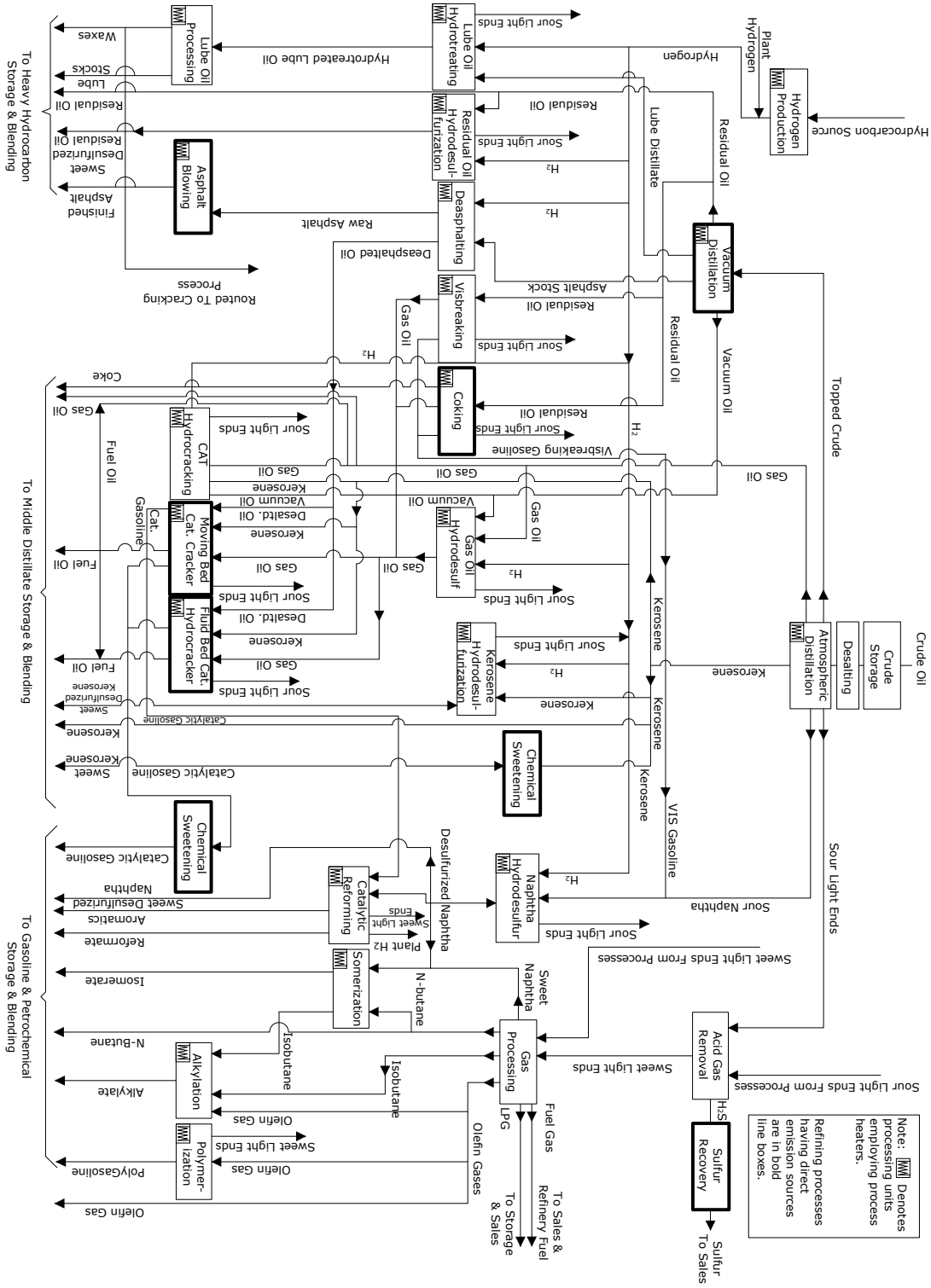

Figure 1.11: Schematic representation of an oil refinery.[114]

The major types of sulphur-containing compounds in crude oil are depicted in Figure 1.12. Removal of sulphur from thiols, sulphides and disulphides is achieved relatively easily. The level of difficulty for hydrodesulphurisation is increasing from thiophenes over benzothiophenes to dibenzothiophenes. This can be explained by their increasing aromatic character. Hydrodesulphurisation of aromatic sulphur-containing compounds is a challenging topic, as they are the most difficult molecules to degrade, a process which is also called "deep desulphurisation".[115–119]

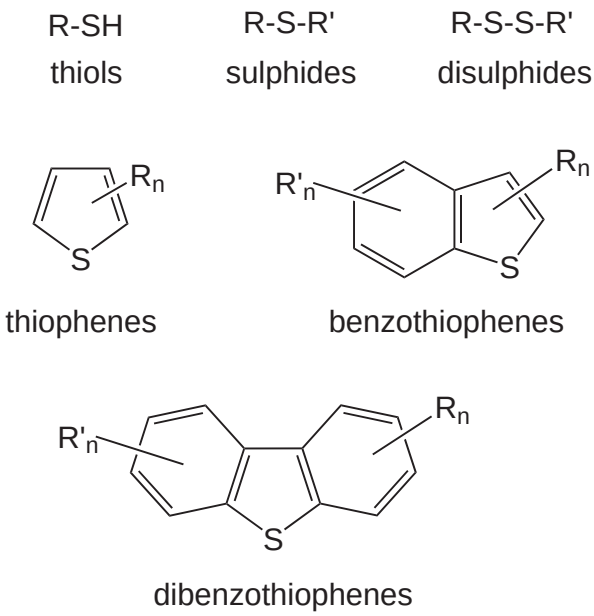

Figure 1.12: Structural formula of sulphur-containing compounds in crude oil. R_n and R'_n are short chain alkyl groups.

Hydrodesulphurisation of Dibenzothiophene

Dibenzothiophene is known to be the most difficult compound to hydrodesulphurise. Extended research results led to the postulation of two reaction routes, which are shown in Figure 1.13.[117–119] The so-called direct desulphurisation (DDS) route includes a direct removal of sulphur without previous hydrogenation. In the second route, a prehydrogenation of an aromatic ring takes place before sulphur removal (HYD). Analysis of the degradation products helped to reconstruct the reaction route.

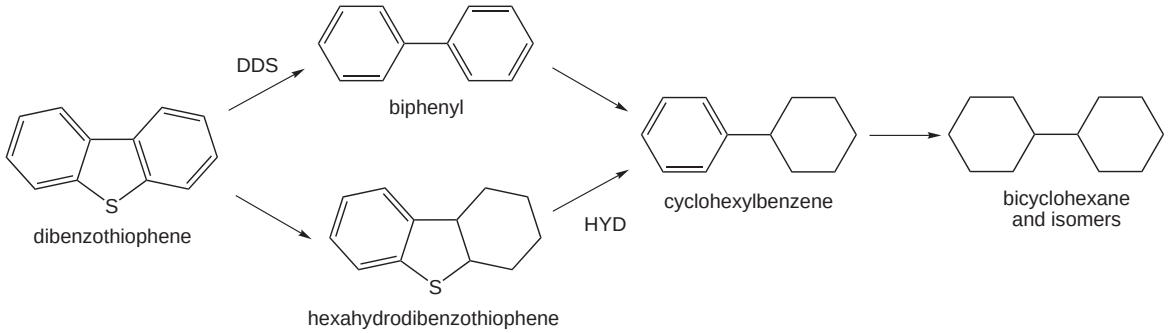

Figure 1.13: Dibenzothiophene conversion route.

Catalyst

During the hydrodesulphurisation reaction, a catalyst is necessary to decrease the activation energy and promote the degradation (Figure 1.14).

$$\text{R-S} + H_2 \xrightarrow{\text{catalyst}} \text{R-H} + H_2S$$

Figure 1.14: Hydrodesulphurisation reaction by a catalyst.

There is a large variety of suitable catalysts, which were discovered by systematic studies. The choice of catalyst must adapt to the given refinery circumstances (crude oil feed and selectivity of the products). The most conventional ones, however, are catalysts promoted by Mo or W,*e.g.* Co-Mo, Co-W, Ni-Mo and Ni-W, which are generally supported on alumina. It is known that addition of phosphorous as an additive leads to the preference of the desulphurisation (DDS) route over the hydrogenation (HYD) route (see Figure 1.13). The proportions of the different metals in the supporting material vary widely: the most efficient amounts for cobalt or nickel are between 1–5 wt%. Molybdenum in turn is contained at about 8–15 wt% and the best tungsten contribution is achieved by about 12–25 wt%.[120]

It turned out that other pure metals and additionally metal sulphides are very active catalysts towards HDS. Studies reveal that the catalytic activity of metal sulfides depends on the used metal.[121] Additionally, the position of the metal in the periodic system directly relates to the observed activity. The interpretation of these data follows a concept of Sabatier which is named "volcano-type" graph.[122] In Figure 1.15, a typical volcano-plot for transition metal sulfides is presented. This class of materials is currently one of the most successful for the catalytic hydrodesulphurisation of dibenzothiophene.

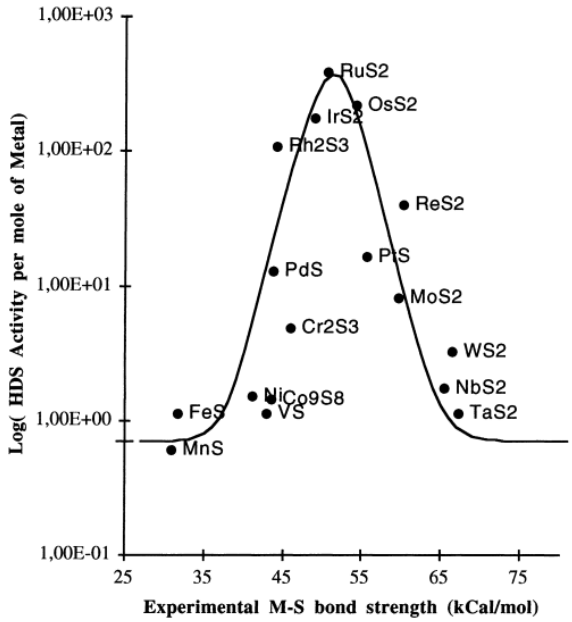

Figure 1.15: DBT HDS experimental specific activities versus M–S bond strengths of transition metal sulphides (black dots).[123] The solid line is a fit of a kinetic model.[124]

Only a few studies have been carried out on catalytic activities of transition metal silicides so far: the semihydrogenation of a propargylic alcohol over highly active amorphous $Pd_{81}Si_{19}$ in supercritical carbon dioxide has been investigated by the group of Baiker *et al.*,[125–127] while other examples are the activation of Cu/Si and Cu/Zn/Sn/Si contact masses for the synthesis of methylchlorosilanes[128] or the synthesis and catalytic properties of silicide modified nickel catalysts for phenylacetylene hydrogenation.[62]

1.6 Goal of the Work

The aim of this work is the preparation of group 6–8 metal silicide nanoparticles in a porous matrix (*e.g.* SiO_2, Al_2O_3, charcoal) and the investigation of their relevance for heterogeneous catalysis.

The focus of the first part of this work is on the synthesis and characterisation of transition metal silicide nanocomposites by use of suitable precursors.

In principle, two main routes are available for the preparation of nanostructured transition metal silicides by single-source precursors:

1. chemical vapour deposition (CVD) of transition metal carbonyl trichlorosilyl complexes, $M(CO)_n(SiCl_3)_m$.
2. thermolysis of organometallic polymers containing both the desired metal and silicon.

The first route was successfully applied to transition metal silicide nanowire growth on specific substrates.[66] The preparation of complexes with various different metal centers is a standard procedure according to the literature and yields single-source precursors with high purity.[68]

For the preparation of metal silicide nanoparticles distributed in a porous matrix, the applicability of $M(CO)_n(SiCl_3)_m$ complexes for nanoparticle formation had to be investigated in detail on different supporting materials. Additionally, subsequent in-depth characterisation of the obtained materials is a crucial part of the present work. Open questions about the possible degradation mechanism of $M(CO)_n(SiCl_3)_m$ had to be elucidated with the aid of density functional theory calculations.

The second synthetic route to the desired nanocomposites by use of organometallic polymers has been pursued only by a few groups.[79,85,86,91] Based on those results, further organometallic polymers had to be synthesised and thermolysed under different conditions (*e.g.* temperature, duration) to obtain transition metal silicide nanoparticles in a SiC/C matrix. The influence of the thermolysis parameters on shape and phase of the obtained silicides had to be investigated. Additionally, the magnetisation behaviour of the materials had to be studied as a function of the size of the obtained particles.

In the second part, the applicability of metal silicides as catalysts for hydrodesulphurisation (HDS), which constitutes an important part of the crude oil refinement process, is tested. The substrate chosen for HDS experiments is dibenzothiophene, which is known to be the most difficult to desulphurise. Such experiments have not been performed previously in any detail with metal silicides as possible catalysts. They are obvious candidates, given that metal sulphides and phosphides are known to be suitable catalysts for HDS.

The study of reaction kinetics and degradation routes is of relevance in order to understand the behaviour of the employed catalysts. The application of metal silicides to hydrodesulphurisation is an important aspect of the ongoing systematic studies to discover novel catalysts.

2 Results and Discussion

2.1 Formation of a Silylene-Bridged Iron Complex

The experiments by Zybill *et al.*[67,68] on the formation of FeSi from *cis*-$Fe(CO)_4(SiCl_3)_2$ were carried out under CVD conditions, *i.e.* the decomposition of *cis*-$Fe(CO)_4(SiCl_3)_2$ and formation of iron silicides occurred at silicon or glass surfaces. A clear dependence on the substrate surface was observed, as β-$FeSi_2$ films were formed on a Si(100) surface and polycrystalline cubic FeSi on a Pyrex glass substrate.

In an attempt to prepare iron silicide nanoparticles, we carried out thermolysis of *cis*-$Fe(CO)_4(SiCl_3)_2$ under different conditions. To this end, solid *cis*-$Fe(CO)_4(SiCl_3)_2$ was sealed in a glass vial under argon and heated to 350°C for 30 min. After cooling to room temperature, the vial was opened and $FeCl_2$ and yellow, needle-shaped crystals of $Fe_2(CO)_6(SiCl_2)_3$ were obtained as the only solid compounds.

A silicide phase or residual starting compound was not observed. Although we did not analyse the gaseous products, theoretical calculations (*vide infra*) and photoelectron spectroscopy studies by Zybill *et al.*[67,68] suggested that CO and $SiCl_4$ were also formed. Thus, the overall reaction could be:

$$5\ Fe(CO)_4(SiCl_3)_2 \longrightarrow FeCl_2 + 2\ Fe_2(CO)_6(SiCl_2)_3 + SiCl_4 + 8\ CO$$

Figure 2.1: Possible overall reaction of $Fe_2(CO)_6(SiCl_2)_3$ formation.

Complex $Fe_2(CO)_6(\mu_2{-}SiCl_2)_3$ crystallised in the highly symmetric space group $P6_3/m$ (Figure 2.2). The iron atoms were octahedrally coordinated with a facial arrangement of the carbonyl ligands and three bridging dichlorosilylene ligands connecting the two metal centers.

In comparison to the known crystal structure of $Fe_2(CO)_6(\mu_2{-}SiClMe)(\mu_2{-}SiMe_2)_2$ (Fe–Fe 270.5(1)) pm, average Fe–Si = 232.2(2) pm),[129] which has been obtained in low

yield by photochemical reaction of $Fe_2(CO)_8(SiMe_2)_2$ with $Fe(CO)_4(H)Si{-}Me_2Cl$,[130] the Fe–Fe distance (272.6(8) pm) in $Fe_2(CO)_6(\mu_2{-}SiCl_2)_3$ was only slightly longer, and the Fe–Si distance (229.7(4) pm) slightly shorter. The structure of $Fe_2(CO)_6(\mu_2{-}SiCl_2)_3$ is related to the prototypical $Fe_2(CO)_9$ with the same point group (D_{3h}). Replacement of the three silylene ligands by three bridging carbonyl ligands resulted in a significantly shorter Fe–Fe distance of 252.3(8) pm.[131] Crystal data and parameters of $Fe_2(CO)_6(SiCl_2)_3$ are shown in the Appendix (Table 5.1).

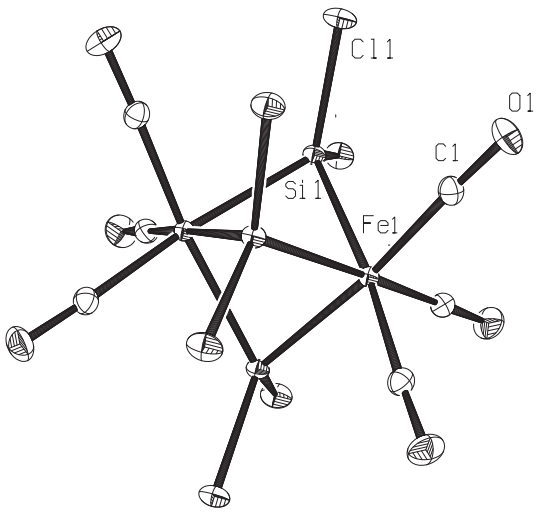

Figure 2.2: ORTEP plot of $Fe_2(CO)_6(SiCl_2)_3$. Selected bond distances (pm) and angles (deg): Fe(1)–Fe(1)* 272.6(8), Fe(1)–C(1) 181(1), Fe(1)–Si(1) 229.7(4), Si(1)–Cl(1) 204.2(6), Si(1)–Fe(1)–Si(1)* 72.805(4), Fe(1)–Si(1)–Cl(1) 120.58(1) (Atoms marked with an asterisk are symmetry–related).

The IR spectrum of $Fe_2(CO)_6(SiCl_2)_3$ showed two strong absorptions in the carbonyl region at 2022 and 2001 cm^{-1}. Frequencies scaled by a factor of 0.9945[132] obtained from calculations carried out as part of the computational study reproduced the experimental results with high accuracy (calculated values: 2029 and 2001 cm^{-1}).

The different outcome of the thermolysis reaction, compared to that reported by Zybill *et al.*,[67,68] prompted us to recalculate possible intermediates for this reaction. We first investigated CO dissociation as a possible initial step in the total reaction. The first bond dissociation energies for *cis*-$Fe(CO)_4(SiCl_3)_2$ (Table 2.1) are 29.9 kcal/mol for the CO ligand *trans* to CO and 25.9 kcal/mol for the CO ligand *trans* to $SiCl_3$.

We were also able to locate transition states for CO ligand dissociation in both cases, $\mathbf{TS_{AB}}$ and $\mathbf{TS_{AC}}$, leading to $Fe(CO)_3(SiCl_3)_2$: the energetic barriers amount to 30.5 and 23.6 kcal/mol (Figure 2.3, compound **A** in the calculations corresponds to complex

$Fe(CO)_4(SiCl_3)_2$, **B** and **C** denote the products of CO dissociation *cis* or *trans* to $SiCl_3$). This implies both thermodynamic and kinetic labilisation of the CO ligands *trans* to the $SiCl_3$ ligands, which is in excellent agreement with the experimental observation that PPh_3 exclusively substitutes the CO ligands *trans* to the SiR_3 in complexes *cis*-$Fe(CO)_4(SiR_3)_2$.[133,134]

Table 2.1: First bond dissociation energies and associated barrier heights for $Fe(CO)_4(SiCl_3)_2$.

Bond	**D_e (kcal/mol)**	**ΔG_{TS} (kcal/mol)**
Fe–$CO_{trans\ CO}$	29.9	30.5 (heterolytic dissociation)
Fe–$CO_{trans\ SiCl_3}$	25.9	23.6 (heterolytic dissocitaion)
Fe–$SiCl_3$	38.5	36.1 (homolytic dissocitaion)

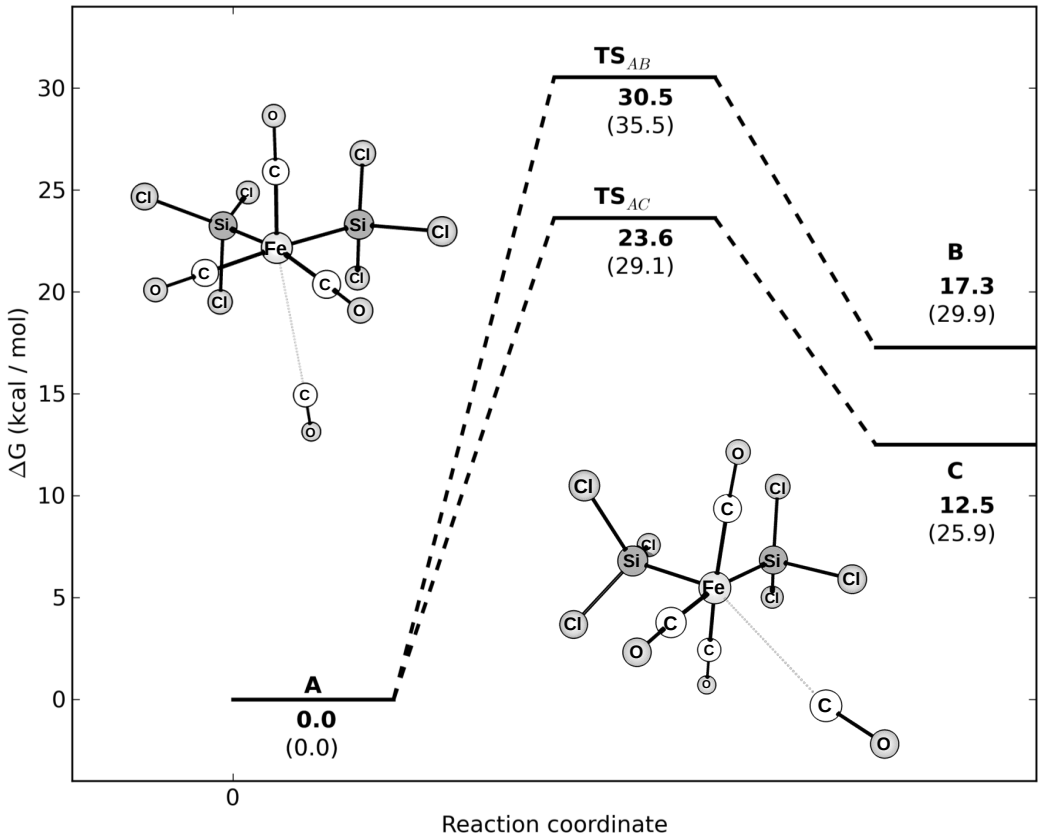

Figure 2.3: Gibbs free-energy profile for CO ligand dissociation from **A**. The numbers in parentheses are differences in uncorrected electronic energies.

As discussed later (see Section 2.2.1), the Fe–Si bond in $Fe(CO)_4(SiR_3)_2$ was heterolytically cleaved in solution in the presence of HMPA to stabilise the cleaved $SiCl_3^+$.[72] Such a charge separation is expected to be highly unfavourable in the gas phase, *i.e.*

in the absence of any stabilising agent. As a matter of fact, a stepwise lengthening of one of the Fe–Si bonds from the calculated equilibrium distance of 245 pm in **A** (with multiplicity $2S + 1 = 1$) led to a continuous increase in energy and an asymptotic approach to the energy of $[(CO)_4FeSiCl_3]^-$ and $SiCl_3^+$ at infinite separation (Figure 2.4). Consequently, the energy required for $SiCl_3^+$ dissociation (*i.e.* on the singlet surface) was very high (Figure 2.4).

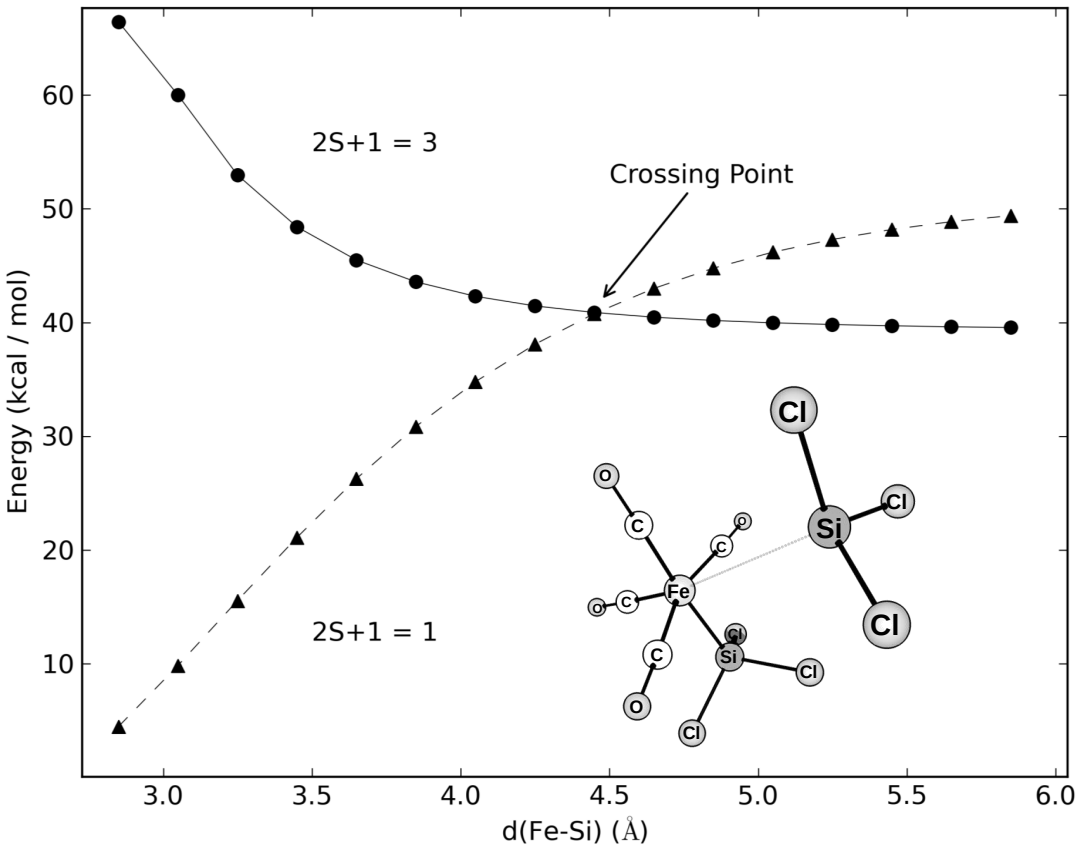

Figure 2.4: Pure electronic energy as a function of Fe–Si bond length for both singlet and triplet states (S = angular spin momentum).

We were unable to locate a transition state for unimolecular $SiCl_4$ elimination from neutral *cis*-$Fe(CO)_4(SiCl_3)_2$. This was due to an unfavourable interaction between a region of the LUMO with s-character at the silicon atom of the $SiCl_3$ group and an orbital of the HOMO with p_z-character on the chloride atom in closest proximity.

Nevertheless, Zybill *et al.* estimated an energy for $SiCl_4$ elimination by a constrained geometry optimisation, which was as high as 47 kcal/mol.[67,68] We re-evaluated this result at the present level of theory and found that a constrained optimisation led to a geometry that unsurprisingly is not a stationary point on the potential energy surface.

The vibrational mode corresponding to the observed imaginary frequency was in fact a rotation around one of the Fe–Si bonds.

In light of those findings, a different mechanism was postulated for the elimination of $SiCl_4$ during the thermolysis of $Fe(CO)_4(SiCl_3)_2$. Starting from **A**, we proposed a homolytic Fe–Si bond cleavage (Table 2.1), resulting in a $SiCl_3$ radical as a crucial participant in further mechanistic steps. Chlorine abstraction by $SiCl_3$ radicals has already been the subject of a computational study in a related context.[135]

In contrast to heterolytic Fe–Si bond cleavage on the singlet surface, homolytic Fe–Si bond cleavage on the triplet surface (multiplicity $2S+1 = 3$) was much more favourable. We were able to approximate the location of the corresponding transition state as a crossing point between the singlet and triplet state by an evaluation of the energy as a function of one of the Fe–Si bond lengths (Figure 2.4).[136]

Transition state energies for dissociation reactions are summarised in Table 2.1. We did not consider Cl_2 or Cl radicals because only $SiCl_4$ and CO were observed in photoelectron spectroscopy studies of the thermolysis reaction of $Fe(CO)_4(SiCl_3)_2$.[67,68]

In Figure 2.5 two proposed mechanistic pathways leading to the radical species $[(CO)_3Fe(SiCl_3)(SiCl_2)]^\bullet$ (**E**) are shown (for a graphical representation of the structures, see Figure 2.6). Obviously, either CO dissociation or chlorine abstraction by a $SiCl_3$ radical can initially take place. Different transition states are possible for chlorine abstraction, differing only in rotation about the Fe–Si bond. Only the transition states (**TS**) with the lowest barrier are shown in the energy profile in Figure 2.6.

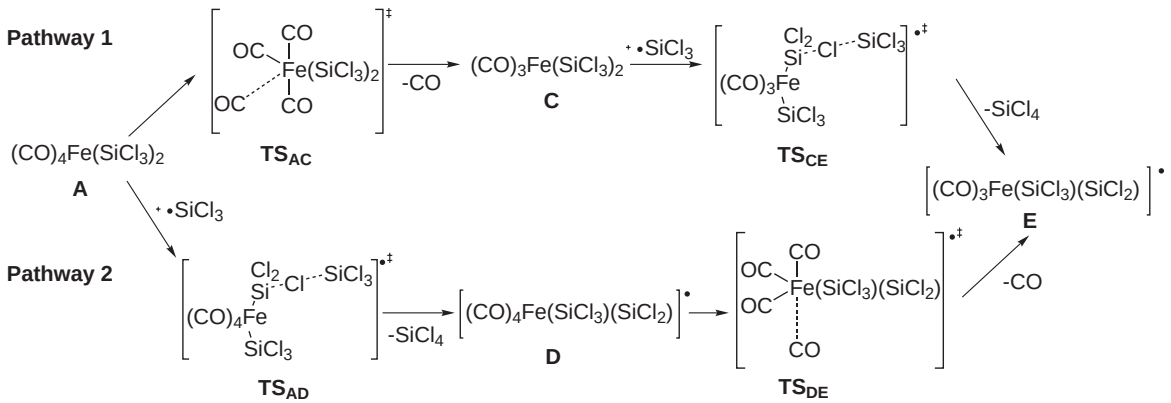

Figure 2.5: Possible pathways for formation of **E**.

The calculations led to the conclusion that CO dissociation as a first step ($\mathbf{TS_{AC}}$) was less favourable and associated with a barrier of 23.6 kcal/mol in comparison to

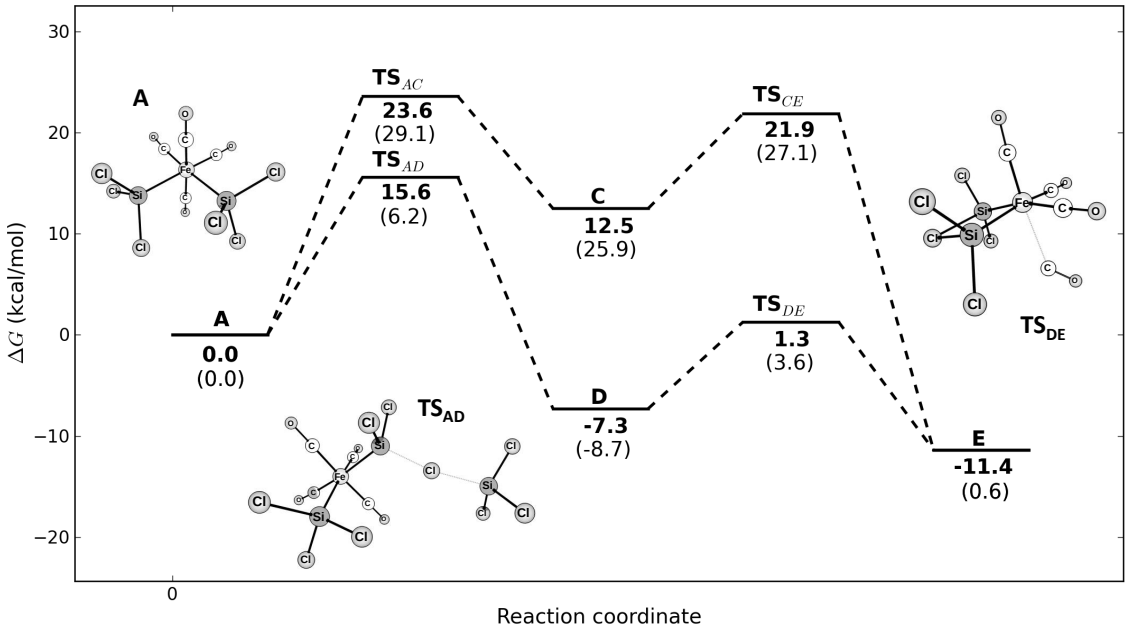

Figure 2.6: Reaction profile for two different pathways towards **E**. Gibbs free energies are shown; the numbers in parentheses are differences in uncorrected electronic energies.

transition state $\mathbf{TS_{AD}}$ leading to radical species $(CO)_4Fe(SiCl_3)(SiCl_2)$ (**D**). The second pathway, *i.e.* CO abstraction, is characterised by a low energy barrier of 8.6 kcal/mol (energy of $\mathbf{TS_{DE}}$ relative to **D** in Figure 2.6). In summary, the second pathway is more likely, and the overall reaction leading from **A** to **E** is exergonic with -11.4 kcal/mol.

We envision that **E** is a direct precursor for compound $Fe_2(CO)_6(SiCl_2)_3$ after further $SiCl_4$ elimination by recombination with itself, now involving a triplet-singlet intersystem crossing (Figure 2.7).

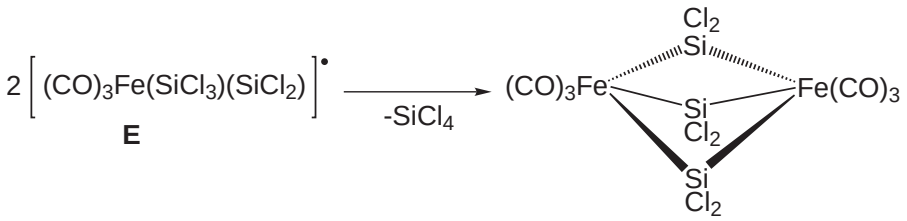

Figure 2.7: Proposed recombination of **E** to $Fe_2(CO)_6(SiCl_2)_3$.

In conclusion, the new dimeric iron complex $Fe_2(CO)_6(SiCl_2)_3$ with three bridging silylene ligands was isolated and unequivocally characterised by single crystal X-ray diffraction. An alternative mechanistic rationale for $SiCl_4$ formation during thermolysis

of $Fe(CO)_4(SiCl_3)_2$ was proposed based on DFT calculations. The proposed mechanism involved chlorine abstraction by a $SiCl_3$ radical generated from homolytic Fe–Si bond cleavage, involving a singlet-triplet intersystem crossing. We have not investigated whether further thermolysis of $Fe_2(CO)_6(SiCl_2)_3$ results in the formation of iron silicides.

2.2 Cleavage of Transition Metal-Silicon Bonds

Zybill's group proposed a mechanism for the gas-phase decomposition of *cis*-$Fe(CO)_4(SiCl_3)_2$ involving an intermediate silylene complex formed by $SiCl_4$ elimination. This silylene intermediate is considered to be a highly active species, which further decomposes and nucleates to FeSi including further CO and Cl_2 elimination. The following degradation mechanism was suggested (Figure 2.8), whose occurrence is specific to the reaction taking place on the surface of a substrate (*e.g.* glass surface).[67,68]

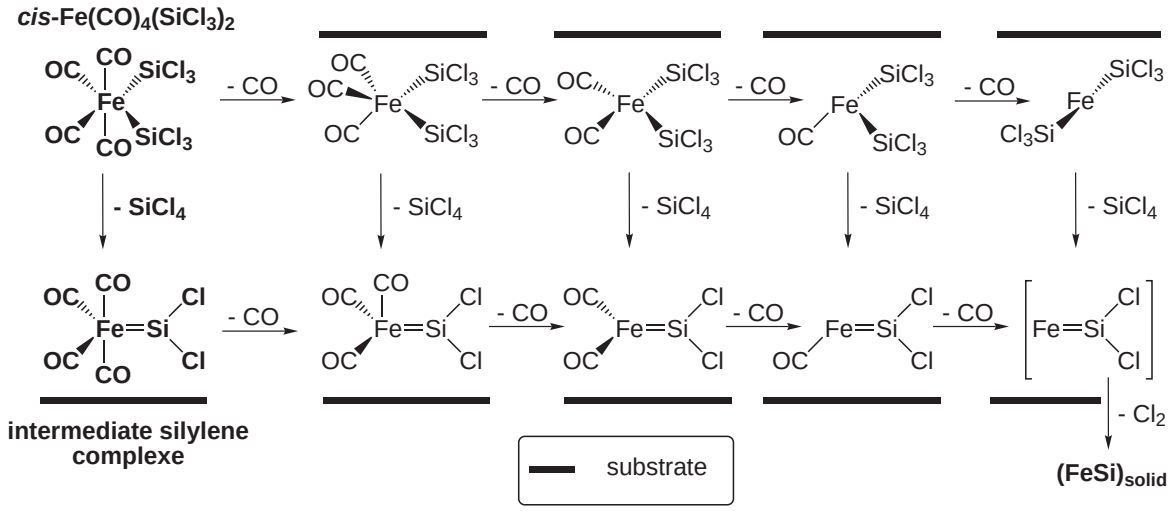

Figure 2.8: Gas-phase degradation mechanism of *cis*-$Fe(CO)_4(SiCl_3)_2$ to FeSi on a substrate.

We were interested whether a similar mechanism is feasible in solution, especially whether *cis*-$Fe(CO)_4(SiCl_3)_2$ can be transformed to the known donor-stabilised silylene complex $(CO)_4Fe{=}SiCl_2(HMPA)$ by reaction with hexamethylphosphoric triamide (HMPA). This complex has previously been obtained by treating the complex $[Fe_2(\mu\text{-}SiMe_2)_2(CO)_8]$ with an excess of the strong Lewis base HMPA in C_6D_6 (Figure 2.9).

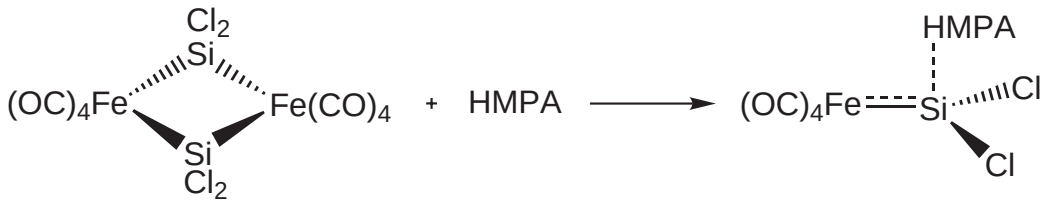

Figure 2.9: Cleavage of $[Fe_2(\mu_2\text{-}SiMe_2)_2(CO)_8]$ by HMPA to base-stabilised silylene.

2.2.1 Cleavage of an Iron-Silicon Bond

Addition of an excess of HMPA to a $[D_8]$toluene solution of *cis*-$Fe(CO)_4(SiCl_3)_2$ and sonication at room temperature led to a single new product within 10 min, as evidenced by ^{31}P NMR spectroscopy. A peak at 18.40 ppm indicated the formation of a single new phosphorus-containing species, differing from free HMPA (23.71 ppm).

The ^{29}Si NMR spectrum exhibited two signals at 68.11 and -205.84 ppm. The signal at 47.46 ppm in *cis*-$Fe(CO)_4(SiCl_3)_2$ was shifted to 68.11 ppm, attributed to the anionic complex $[Fe(CO)_4SiCl_3]^-$. The peak at -205.84 ppm was located in the range of hexacoordinated silicon compounds and indicated the formation of the cationic species $[SiCl_3(HMPA)_3]^+$.[137] The ^{13}C NMR data showed two signals for carbonyl carbons at 216.60 and 215.77 ppm, and a signal at 36.51 ppm attributed to the carbon atoms in HMPA. From the ^1H NMR experiment a conversion of 86% was calculated.

IR measurements in toluene solution showed four absorption bands in the carbonyl region of the spectrum at 2029 (w), 1951 (w), 1923 (s), 1910 (s) cm^{-1}. Scaled frequencies obtained from calculations carried out as part of the computational study (*vide infra*) on $[SiCl_3(HMPA)_3]^+[Fe(CO)_4SiCl_3]^-$ reproduced the experimental results remarkably well and showed that the doubly degenerate E vibration of a trigonal bipyramidal $Fe(CO)_4X$ compound with C_{3v} symmetry was split into two energetically different vibrations (1923 and 1910 cm^{-1}, see Table 2.2).

Table 2.2: Comparison of experimental and calculated ν_{CO} values (scale factor 0.98).[138]

ν_{CO} (experimental) (cm^{-1})	ν_{CO} (calculated) (cm^{-1})
2029	2029
1951	1970
1923	1955
1910	1912

Colorless crystals grown by slow diffusion of *n*-hexane into a saturated toluene solu-

tion were chosen for X-ray diffraction measurements, which revealed the ionic complex $[SiCl_3(HMPA)_3]^+[Fe(CO)_4SiCl_3]^-$. This compound was formed by cleavage of an Fe–Si bond and stabilisation of the cleaved $SiCl_3$-ligand by three HMPA molecules, resulting in a cationic hexacoordinated silicon compound (Figure 2.10, Table 2.3). The structural data thus confirmed the spectroscopic studies. The anionic iron complex has a trigonal-bipyramidal geometry (idealised point group C_{3v}) with the $SiCl_3$-ligand in an apical position. The chlorine substituents in the cationic, octahedral silicon compound have a meridional arrangement. Its structure was closely related to the known $[SiCl_3(HMPA)_3]^+[HCl_2]^-$.[137] In comparison with non-coordinated HMPA, a lengthening of the P–O bond and a concomitant shortening of the P–N bond was observed.[139]

Table 2.3: Selected bond lengths (Å) and angles (deg) of $[SiCl_3(HMPA)_3]^+$ $[Fe(CO)_4SiCl_3]^-$.

Fe(1)–Si(1)	2.229(1)	Si(2)–Cl(5)	2.202(2)
Fe(1)–C(1)	1.779(4)	Si(2)–Cl(6)	2.211(2)
Fe(1)–C(2)	1.757(4)	Si(2)–O(5)	1.763(2)
Fe(1)–C(3)	1.789(4)	Si(2)–O(6)	1.755(2)
Fe(1)–C(4)	1.786(4)	Si(2)–O(7)	1.769(2)
Si(1)–Cl(1)	2.088(2)	P(1)–O(5)	1.512(2)
Si(1)–Cl(2)	2.089(2)	P(1)–N(1)	1.623(3)
Si(1)–Cl(3)	2.095(2)	P(1)–N(2)	1.629(3)
Si(2)–Cl(4)	2.211(2)	P(1)–N(3)	1.622(3)
C(1)–Fe(1)–Si(1)	85.83(2)	Cl(1)–Si(1)–Cl(3)	101.43(5)
C(2)–Fe(1)–Si(1)	85.83(2)	Cl(2)–Si(1)–Cl(3)	100.99(5)
C(3)–Fe(1)–Si(1)	86.76(2)	Cl(1)–Si(1)–Fe(1)	116.12(5)
C(4)–Fe(1)–Si(1)	179.78(2)	Cl(2)–Si(1)–Fe(1)	117.25(5)
Cl(1)–Si(1)–Cl(2)	101.36(6)	Cl(3)–Si(1)–Fe(1)	117.00(5)

The cleavage reaction of an Fe–Si bond by hexamethylphosphoric triamide leading to the new ionic complex $[SiCl_3(HMPA)_3]^+[Fe(CO)_4SiCl_3]^-$ was additionally investigated by density functional calculations. Two possible pathways can be imagined (Figure 2.11), *viz.* a mechanism involving an intermediate silylene complex or direct Fe–Si bond cleavage.

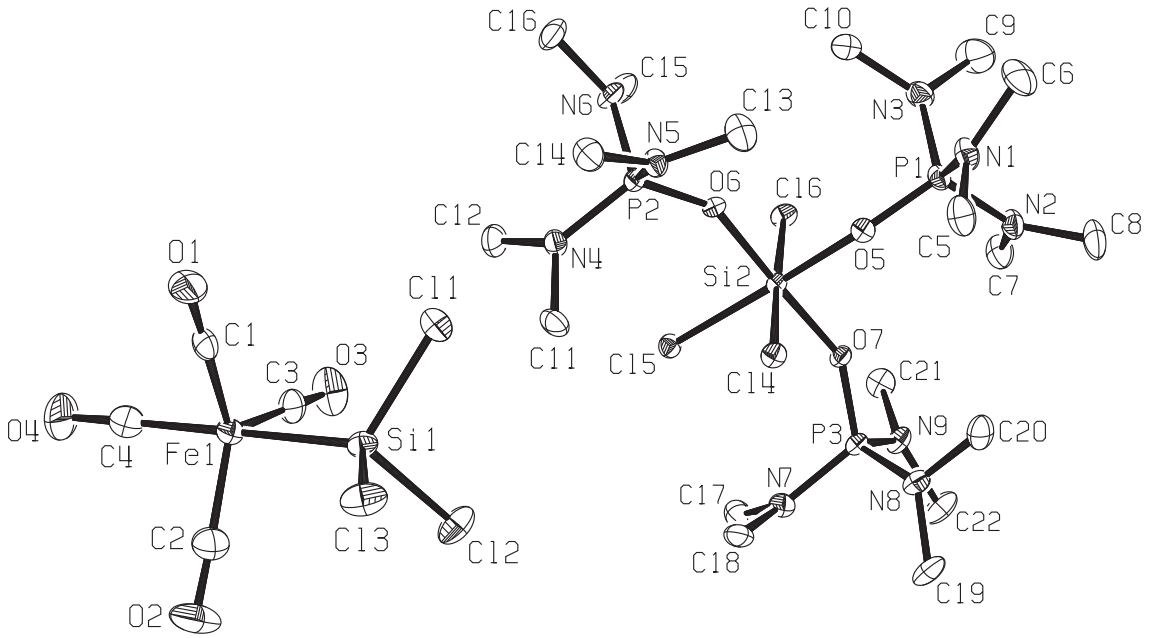

Figure 2.10: ORTEP plot and crystallographic numbering scheme of $[SiCl_3(HMPA)_3]^+[Fe(CO)_4SiCl_3]^-$.

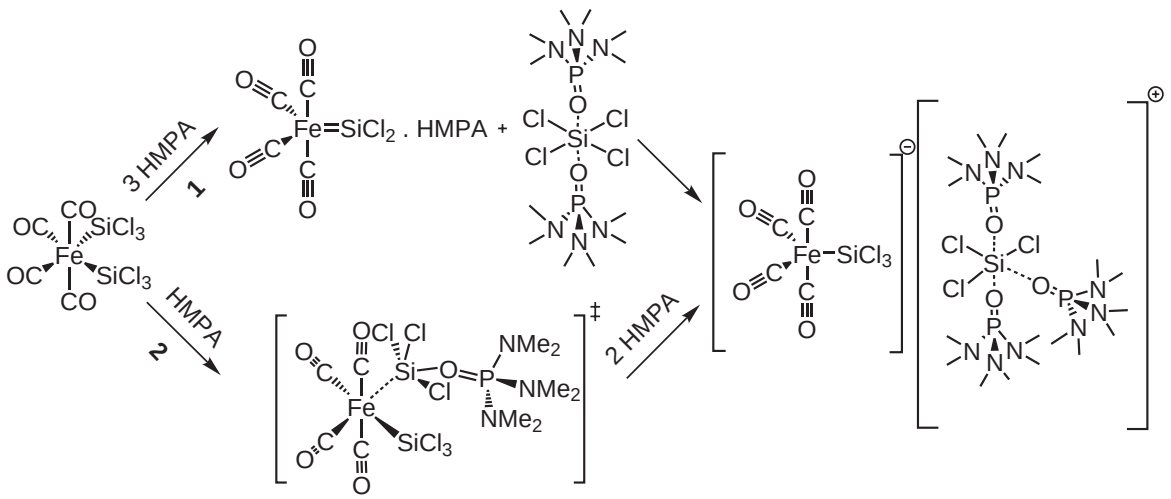

Figure 2.11: Possible reaction pathways of the formation of $[SiCl_3(HMPA)_3]^+$ $[Fe(CO)_4SiCl_3]^-$.

Due to steric constraints imposed by the size of HMPA and the octahedral geometry of *cis*-$Fe(CO)_4(SiCl_3)_2$, an approach to one of the equivalent iron-bonded $SiCl_3$ ligands was only possible opposite to the iron atom. Consequently, only one ground state was located for a *cis*-$Fe(CO)_4(SiCl_3)_2$–HMPA adduct (**B**, see Figure 2.12). The formation of **B** was slightly endergonic at 298.15 K by +5.9 kcal/mol after inclusion of thermal corrections, but it was exothermic in terms of enthalpy by -10.5 kcal/mol, and no barrier was found. Slight elongation of the Fe–Si bond by 0.08 Å occurred concomitant with the formation of a Si–O single bond (1.71 Å).

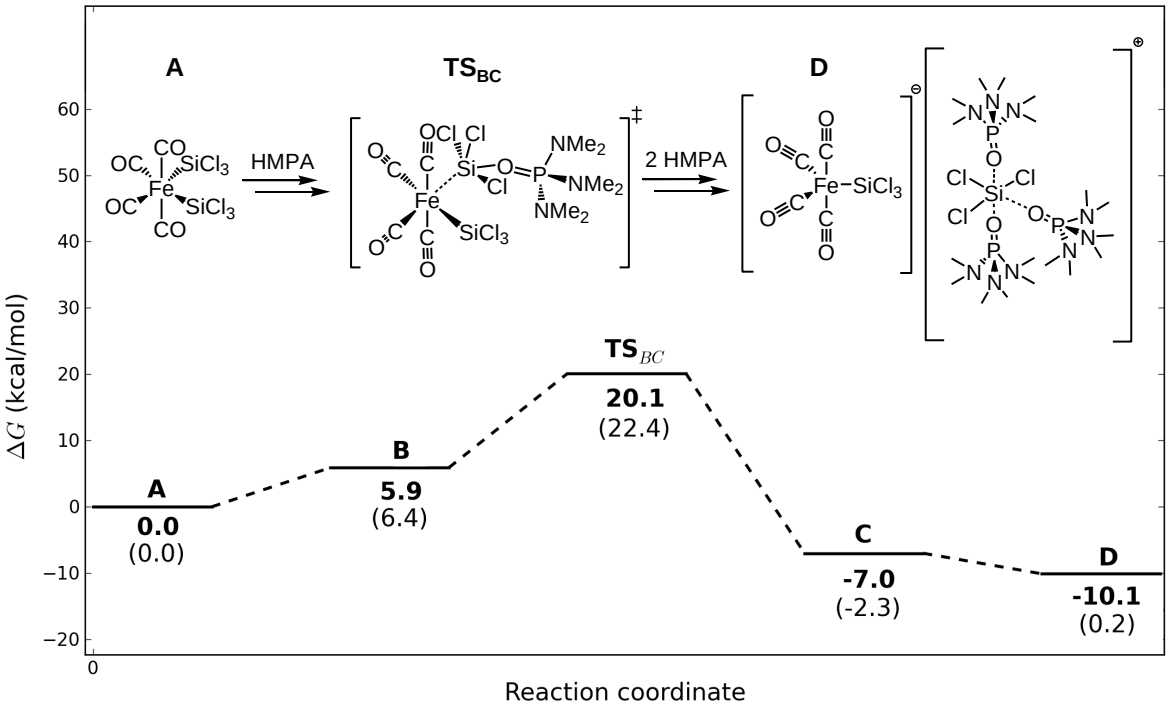

Figure 2.12: Reaction profile for direct Fe–Si bond cleavage.

All attempts to locate a transition state leading to the formation of an intermediate silylene complex by subsequent $SiCl_4$ elimination from **B** were unsuccessful: one Si–Cl bond in **B** was significantly elongated (2.50 Å vs. 2.12 Å in **A**) but could not participate in a chloride transfer because of its orientation away from the other $SiCl_3$ group.

Additionally, visual inspection of the Kohn-Sham orbitals revealed an anti-bonding relationship between a region of the LUMO with s character on the silicon atom of the trichlorosilyl group and an orbital of the HOMO with p_z character on the chloride atom in closest proximity. Furthermore, the overall difference in Gibbs Free Energy for the alternative reaction is +48.5 kcal/mol, rendering this pathway thermodynamically

unfavourable.

In contrast, the transition state for direct bond cleavage (**TS**) exhibited an energy barrier of 14.2 kcal/mol at 298.15 K. In the transition state, the Fe–Si bond length was already dramatically increased (3.89 Å). The adjacent ground state (**C**) showed two separate species which were further stabilised by two additional HMPA groups, leading to product **D**. The overall reaction was exergonic by -10.1 kcal/mol. Values in parentheses show Gibbs Free Energies for the gas phase. Relative energies of **A**, **B**, **TS** and **C** were similar but coordination of additional HMPA (**D**) would be unfavourable.

A direct Si–Si bond cleavage with the help of a strong donor has been investigated by Bellefon *et al.*[140] in detail for methylchlorodisilane. Kinetic studies of the disproportion of the disilane were carried out with different nucleophiles, among them also HMPA. It has been shown that poor π acceptor nucleophiles (phosphine oxides, -chlorides and trialkylphosphines) were more active disproportionation catalysts. All results supported the following mechanism for this cleavage involving a silylene intermediate (Figure 2.13).

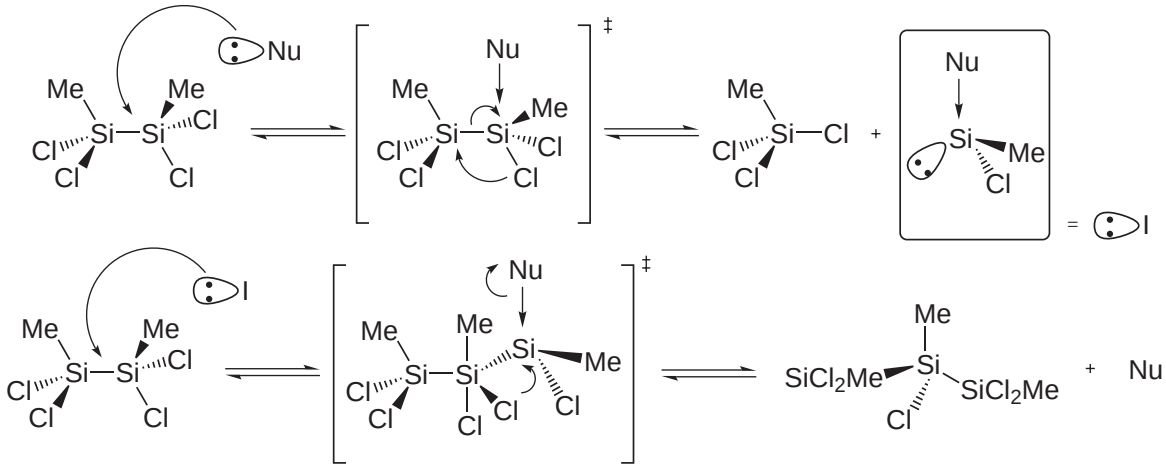

Figure 2.13: Proposed reaction mechanism for catalytic disproportionation of dislanes.

We were interested whether Fe–Si or Si–Si bond cleavage is favoured by the strong donor HMPA. We synthesised a suitable compound which contained both bond types, 1-[dicarbonyl(η^5-cyclopentadienyl)ferrio]-pentachlorodisilane (Figure 2.14). After addition of HMPA to a solution of the complex in C_6D_6 and sonication for several minutes at room temperature, the reaction was monitored by ^{31}P and ^{1}H NMR. In the ^{31}P NMR spectrum a new phosphorous peak at 22.1 ppm was observed, differing from free HMPA (23.17 ppm) and from $[SiCl_3(HMPA)_3]^+$ (18.40 ppm). After 1 h no further reaction

was observed. A maximum yield of 4.3% (quantified by ^{1}H NMR) of the new product was obtained (Figure 2.14).

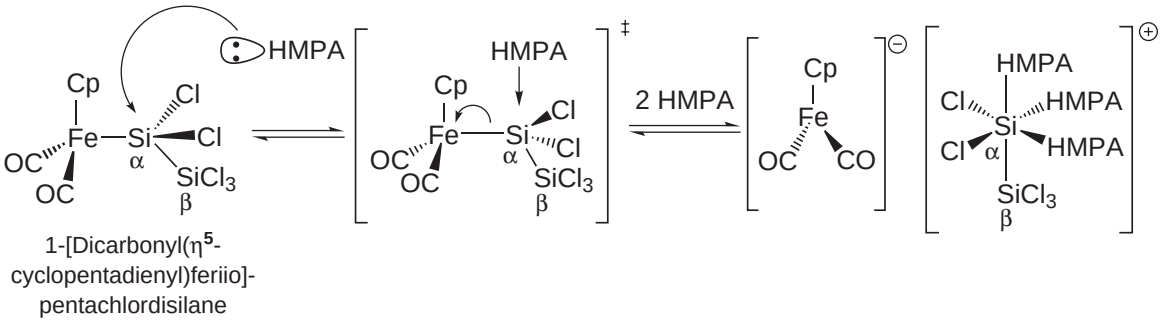

Figure 2.14: Proposed reaction mechanism for Fe–Si cleavage in 1-[dicarbonyl(η^5-cyclopentadienyl)ferrio]-pentachlorodisilane.

The ^{29}Si NMR spectrum exhibited a shift of the β-Si signal from -2.98 to -0.96 ppm and a new signal appeared at -199.2 ppm, which was assigned to α-Si (shifted from 77.21 ppm). The IR spectrum measured in C_6D_6 showed two strong bands at 1911 and 1865 cm^{-1} in the carbonyl region. The band at higher wavenumbers was assigned to the symmetrical stretching vibration of CO and the band at lower wavenumbers results from the asymmetrical stretching vibration of the CO ligands. Computational investigations provided scaled frequencies (1922 and 1884 cm^{-1}, scale factor 0.98[138]) which matched the experimental findings very well and showed the symmetrical and asymmetrical carbonyl vibration of $CpFe(CO)_2^-$ with the expected C_s symmetry.

In conclusion, results support the formation of $[Si_2Cl_5(HMPA)_3]^+[Fe(CO_2)Cp]^-$, resulting from the preferred Fe–Si cleavage and no indication of a Si–Si bond cleavage was detected. Judged by simple steric considerations, a nucleophilic attack by HMPA on the terminal -$SiCl_3$ moiety should be favoured (Figure 2.14). But overall, the Si–Si bond is more stable than the Fe–Si bond regarding bond cleavage.

2.2.2 Cleavage of a Cobalt-Silicon Bond

The complex $Co(CO)_4SiCl_3$ is known as an excellent single-source precursor for the growth of cobalt silicide nanowires by chemical vapour deposition experiments on a substrate.[141] Encouraged by the results obtained for $Fe(CO)_4(SiCl_3)_2$ (*vide supra*), we were interested in the behaviour of $Co(CO)_4SiCl_3$ in the presence of the strong base HMPA.

$Co(CO)_4SiCl_3$ was dissolved in C_6D_6 and HMPA was added by syringe. The colour of the solution immediately turned from yellow to pale blue. After 10 min of sonication at room temperature the reaction was analysed by ^{31}P NMR. A new peak at 18.22 ppm in the ^{31}P NMR appeared, indicating the formation of a new phosphorus containing compound. Compared to the product $[SiCl_3(HMPA)_3]^+[Fe(CO)_4SiCl_3]^-$ which exhibited a phosphorous peak at 18.40 ppm, the observed signal can be attributed to $[SiCl_3(HMPA)_3]^+$. The peak attributed to the trichlorosilyl group of $Co(CO)_4SiCl_3$ at 40.01 ppm in the ^{29}Si NMR measurement disappeared completely and a new signal appeared at -205.81 ppm, in the range of hexacoordinated silicon.

IR measurements in C_6D_6 solution showed four absorptions in the carbonyl region of the spectrum at 2160 (w), 2094 (w), 1961 (s), 1885 (s) cm^{-1}. These values were similar to the above mentioned vibrations in Table 2.2, which implied a trigonal bipyramidal $Co(CO)_4X$ compound with T_d symmetry. Those results supported the formation of $SiCl_3(HMPA)_3]^+[Co(CO)_4]^-$ by a similar reaction mechanism as the iron analogue, a direct Co–Si bond cleavage.

2.3 ^{29}Si NMR Shielding Calculations Employing Density Functional Theory

Results of a DFT study on the calculation of ^{29}Si NMR shieldings are presented, with a database consisting of 41 molecules, with a strong focus on penta- and hexacoordinated silicon compounds (with several silane derivatives for comparison). The need of this study arose out of our desire to use ^{29}Si NMR shielding calculations to assist the interpretation of NMR spectra of hypervalent silicon compounds, such as in Section 2.2, where initial calculations showed rather large deviations between experimental data and calculated chemical shifts.

The selection of molecules for this study consisted of 41 compounds with 44 distinct ^{29}Si NMR shifts (see Figure 2.15 for some examples; structural and molecular formula of all compounds can be found in the Appendix, Figures 5.1, 5.2, 5.3, 5.4, 5.5 and Table 5.3). Compounds **1–14** contained at least one tetracoordinated silicon atom (among them the smallest molecule considered in the present study, trimethoxysilane **1**), while compounds **15–25** exhibited one pentacoordinated silicon atom, respectively. The remainder of the selection (**26–41**) featured molecules containing a hexacoordinated

silicon atom, with compound 41 consisting of 91 atoms representing the largest molecule studied.

The majority of the experimental chemical shifts used for comparison were recorded with $CDCl_3$ as a solvent. Experimental shifts relative to TMS range from +22.9 to -188.7 ppm (see Appendix, Table 5.3). In case of the penta- and hexacoordinated molecules, the selection was guided by the availability of crystal structures as an unambiguous starting point for geometry optimisations and by the intent to investigate compounds with a high degree of structural diversity and different chemical shifts. Of the 41 considered molecules, all species except two (di-anionic **36**, cationic **41**) were neutral.

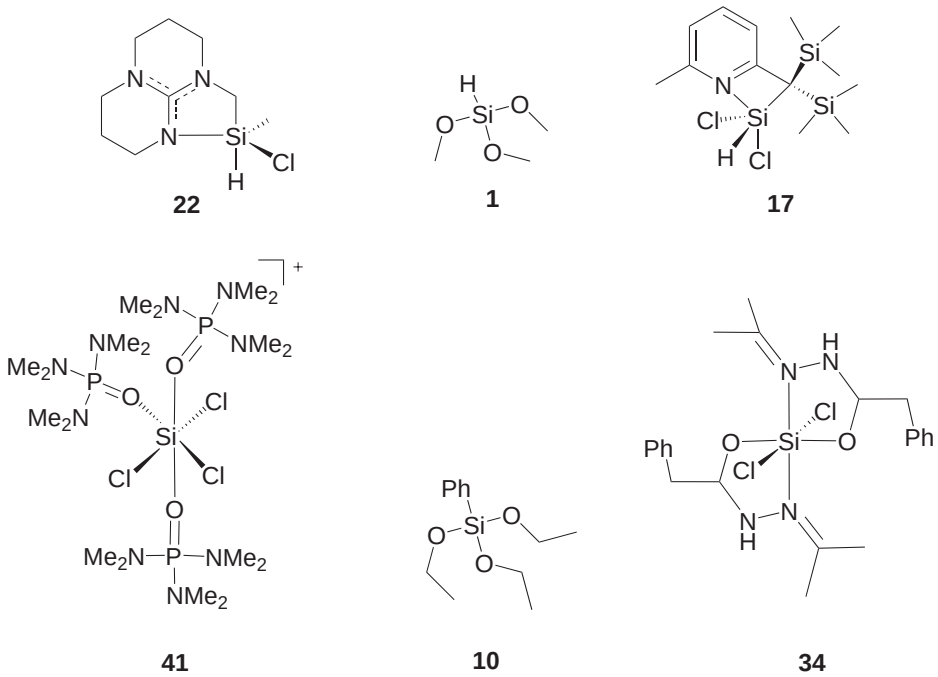

Figure 2.15: Structural formula of six largest outliers.

We are going to discuss deviations between calculated chemical shifts and experimental values in terms of mean absolute error (MAE). δcalc$_i$ = calculated NMR shift, δexpt$_i$ = experimental NMR shift

$$MAE = \frac{1}{n}\sum_{i=1}^{n} |\delta calc_i - \delta expt_i|$$

For economic reasons, we preferred a larger database of molecules with different structural motifs to a larger survey of different density functionals in conjunction with a smaller database, in order to facilitate the identification of possible pathological cases,

as our main concern was finding a suitable level of theory for ^{29}Si NMR shielding calculations with broad applicability to a range of different penta-/hexacoordinated compounds for differentiating between potential reaction products and intermediates. The majority of investigated molecules was medium- to large-sized, which is in contrast to the usual practice of selecting rather small molecules for benchmarking purposes.

For the entire database of 41 molecules (for a discussion on different subsets of the database, see below), the HCTH407/6-311+G(2d) level of theory yielded the best results. Data obtained with the hybrid B3LYP functional in conjunction with the 6-311G(d,p) and LDBS basis sets were more accurate than the ones obtained with the same basis sets alongside the HCTH407 functional. The pure BPW91 functional performs worst by a small margin (regardless of basis set, Figure 2.16). While the superiority of the HCTH407 functional was in agreement with the results obtained by Apeloig *et al.*[104] (on a small set of disilynes), the hybrid B3LYP functional performs better than the pure BPW91 functional in the present study.

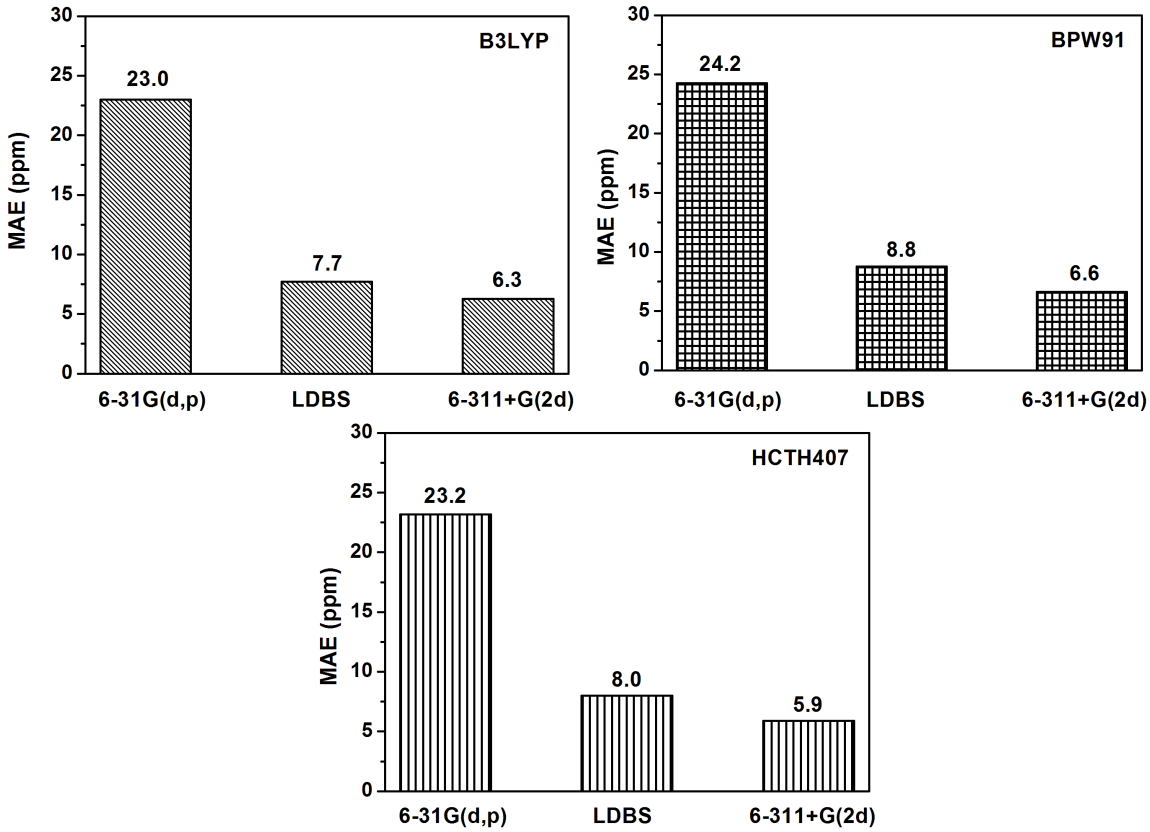

Figure 2.16: Mean absolute errors (MAE) between calculated and experimental chemical shifts for all 41 compounds at the given level of theory.

The results obtained with the locally dense basis set (see computational details in Section 4.3) were strikingly better than the results obtained with 6-31G(d,p) alone; this is of special significance for calculations on large molecules because of the potentially dramatic reduction in cost (*e.g.* the calculations for molecule 41 employ 853, 871 and 1217 basis functions with the 6-31G(d,p), the locally dense and the 6-311+G(2d) basis set, respectively).

Additionally, it is immediately obvious from Figure 2.17 and Table 2.5 that the differences between the results for the locally dense basis set and the 6-311G+(2d) basis are mainly systematic: they are easily corrected using the linear equation obtained from the linear regression (*e.g.* for HCTH407/LDBS, this leads to a reduction of the mean absolute error from 8.0 to 6.5 ppm). While the use of such relatively unbalanced basis sets might not be aesthetically pleasing from a theoretical perspective, it has also been used with success in a recent study by Morris and co-workers.[142]

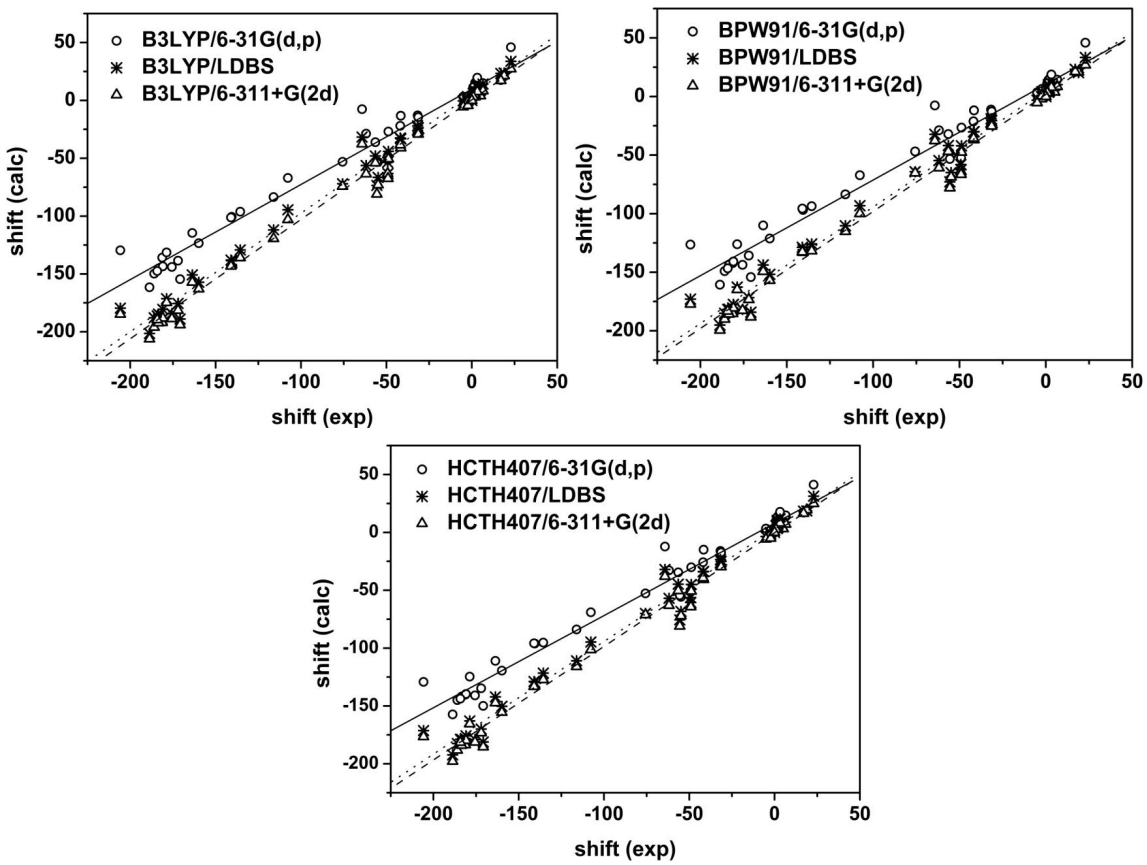

Figure 2.17: Plot of calculated *vs.* experimental chemical shift. Linear regressions are indicated.

Table 2.5: Parameters of the linear regression between experimental and calculated ^{29}Si chemical shift for all silicon containing compounds. A = y-intercept, B = slope, R = correlation coefficient.

Level of Theory	**A**	**B**	**R**
B3LYP/6-31G(d,p)	9.676 ± 2.209	0.823 ± 0.021	0.984
B3LYP/LDBS	5.339 ± 1.772	1.027 ± 0.017	0.993
B3LYP/6-311+G(2d)	0.478 ± 1.773	1.032 ± 0.017	0.994
BPW91/6-31G(d,p)	10.421 ± 2.280	0,817 ± 0.022	0,983
BPW91/LDBS	5.175 ± 1.888	0,994 ± 0.018	0,992
BPW91/6-311+G(2d)	1.731 ± 1.834	0,998 ± 0.018	0,993
HCTH407/6-31G(d,p)	7.868 ± 2.075	0.797 ± 0.020	0.985
HCTH407/LDBS	3.177 ± 1.820	0.974 ± 0.017	0.992
HCTH407/6-311+G(2d)	-0.304 ± 1.789	0.982 ± 0.017	0.993

If the three classes of silicon-containing molecules (*i.e.* silane derivatives, penta- and hexacoordinated compounds, respectively, see Table 2.6) are considered separately, the following trends are evident: for the small 6-31G(d,p) basis set, a very modest agreement with experimental values (regardless of the employed density functional) is only found for the tetracoordinated silane derivatives (compounds **1**–**14**), while the results obtained for penta- and especially hexacoordinated compounds are discouraging.

Table 2.6: MAE in ppm of calculated chemical shifts for silane derivatives (**1**–**14**), penta- (**14**–**25**) and hexa- (**26**–**41**) coordinated compounds, respectively.

	B3LYP			BPW91			HTCH407		
	6-31G (d,p)	LDBS	6-311 +G(2d)	6-31G (d,p)	LDBS	6-311 +G(2d)	6-31G (d,p)	LDBS	6-311 +G(2d)
(1–14)	9.3	6.9	4.5	10.1	6.8	4.9	8.4	5.6	4.4
(14–25)	24.0	9.6	5.8	25.0	11.6	7.7	21.9	9.3	5.7
(26–41)	39.4	7.3	9.0	41.3	9.0	8.0	42.7	10.0	7.9

It is worth noting that Rankin *et al.*[107] recently obtained surprisingly good results when calculating ^{29}Si-^{1}H spin-spin coupling constants at the B3LYP/6-31G level of theory. Regarding ^{29}Si NMR shielding calculations, the results of our study clearly show that this apparently favourable behaviour of the small 6-31G(d,p) basis set does not extend to the penta- and hexacoordinated compounds. The locally dense basis set (LDBS) already offers a dramatic improvement at a very small additional computational cost. Employing the larger, but still computationally tractable 6-311+G(2d) basis set on all atoms results in further improvements and furnishes satisfactory results for both tetracoordinated and hypervalent pentacoordinated compounds.

For six outliers (seven distinct chemical shifts, Figure 2.15), the geometries resulting from additional geometry optimisations at the most accurate level of theory identified above (*i.e.* HCTH407/6-311+G(2d), leading to a combined mean absolute error of 16.7 for the outliers) were used for the ^{29}Si NMR shielding calculations at the same level of theory in order to rule out the introduction of potentially large errors by using different levels of theory for geometry optimisation and subsequent ^{29}Si NMR shielding calculations. The influence of changes in structural parameters (including ro-vibrational effects) on the latter has been discussed in the literature.[100,143–145]

While relatively large changes can be observed in individual cases, they are not systematic, as the overall mean absolute error actually increases (Table 2.7).

Table 2.7: ^{29}Si NMR chemical shifts relative to TMS at higher levels of theory for six outliers and absolute isotropic shielding constants for TMS.

No	**Exp. Shift**	**HCTH407/ 6-311+ G(2d)// B3LYP/ 6-31G(d,p)**	**HCTH407/ 6-311+ G(2d)// HCTH407/ 6-311+G(2d)**	**HCTH407/ 6-311++ G(2df,2pd)// HCTH407/ 6-311+G(2d)**	**HCTH407/ 6-311+G(2d)// HCTH407/ 6-311+G(2d) with IEF-PCM**
1	-54.9 ($CDCl_3$)	-72.1	-74.5	-75.3	-72.7
10	-55.6 ($CDCl_3$)	-80.9	-83.8	-85.7	-79.6
17	-64.8 (C_6D_6)	-38.0	-50.2	-49.8	-55.1
	1.9 (C_6D_6)	5.4, 2.5	5.3, 3.6	6.1, 5.1	5.2, 3.9
22	-49.1 (C_6D_6)	-64.3	-59.2	-58.2	-55.5
34	-163.7 ($CDCl_3$)	-147.3	-142.4	-141.0	-142.9
41	-205.8 ([D_8]toluene)	-176.5	-168.8	-166.3	-170.9
	MAE (ppm)	**16.7**	**16.9**	**17.9**	**14.8**
TMS	0	337.7	337.7	339.0	338.2

Additionally, ^{29}Si NMR shielding calculations for the outliers were carried out with the even larger 6-311++G(2df,2pd) basis set on all atoms in order to measure the influence of basis set quality on the convergence of the obtained results. As shown in Table 2.7, the mean absolute observed change for all seven distinct chemical shifts is less than 1.3 ppm while the mean absolute error increases slightly to 17.9 ppm. We tentatively assume that the observed errors result from our neglect of modelling the influence of the solvent and possible differences between the structure in the solid state and in

solution (Table 2.7).

In a final attempt to reduce the large deviations from experiment for the six outliers, geometry optimisations and shielding calculations with HCTH407/6-311+G(2d) were carried out in conjunction with the integral equation formalism polarised continuum model (IEF-PCM)[146–148] in order to model the influence of the solvent: this approach results in an improved mean absolute error of 14.8 ppm (Table 2.7).

As a direct consequence, the large deviations from experiment observed for the outliers are neither a result of different levels of theory used for geometry optimisation and ^{29}Si NMR shielding calculations, nor insufficient quality of the employed basis sets, nor negligence of solvent effects.

Considering that three molecules with a Si–H bond can be found among the outliers, it is worth pointing out that Heine *et al.*[100] already noted less satisfactory results when calculating chemical shifts of silanes with increasing numbers of hydrogen atoms bound to the silicon atom. The other molecules displaying a large error between experiment and theory do not share any obvious commonalities.

2.4 Cobalt Nanocomposites

Several working groups used transition metal silyl complexes as single-source precursors for growth of transition metal silicide nanowires on given substrates, *e.g.* Si(100)/SiO_2.[67,68,141] This simple approach, which has been reported previously by Lieber and co-workers, uses chemical vapour deposition of these complexes without the use of any metal catalysts.[149] Based on those results we sought to introduce those precursors for nanoparticle formation in an amorphous matrix (*e.g.* silica).

2.4.1 Thermal Decomposition of $Co(CO)_4SiCl_3$ Adsorbed on Silica

In a recent communication, Liang *et al.* claimed to have synthesised CoSi particles on a silica support by thermal decomposition of adsorbed $Co(CO)_4SiCl_3$.[38] To this end, $Co(CO)_4SiCl_3$ was deposited on calcined silica (surface area = 668 m^2/g) in a fluidised bed reactor by chemical vapour infiltration.

When the adsorbed precursor was treated at 300°C in a H_2 atmosphere, particles in silica were obtained which showed neither an X-ray pattern of CoSi nor metallic Co because of the small size of the particles (1–2 nm). The observed lattice spacing in high-resolution TEM led the authors to conclude that CoSi particles (JCPDS PDF 65-3296) were formed. EDX investigations appeared to confirm this assignment. Analogous results were later reported for mesoporous silica.[150] We were able to reproduce all experimental findings for the silica-based composite. Additional experiments, however, did not confirm the conclusions that the particles were CoSi.

The composite sample was prepared in the way described in Section 4.5.1, using the same procedure as in the literature.[38] The silicon:cobalt ratio at the surface of the particles was 6.8:1 (see XPS data below). The transmission electron pattern of the sample treated at 300°C under H_2 showed distinct particles, well-distributed in an amorphous silica matrix (Figure 2.18, left).

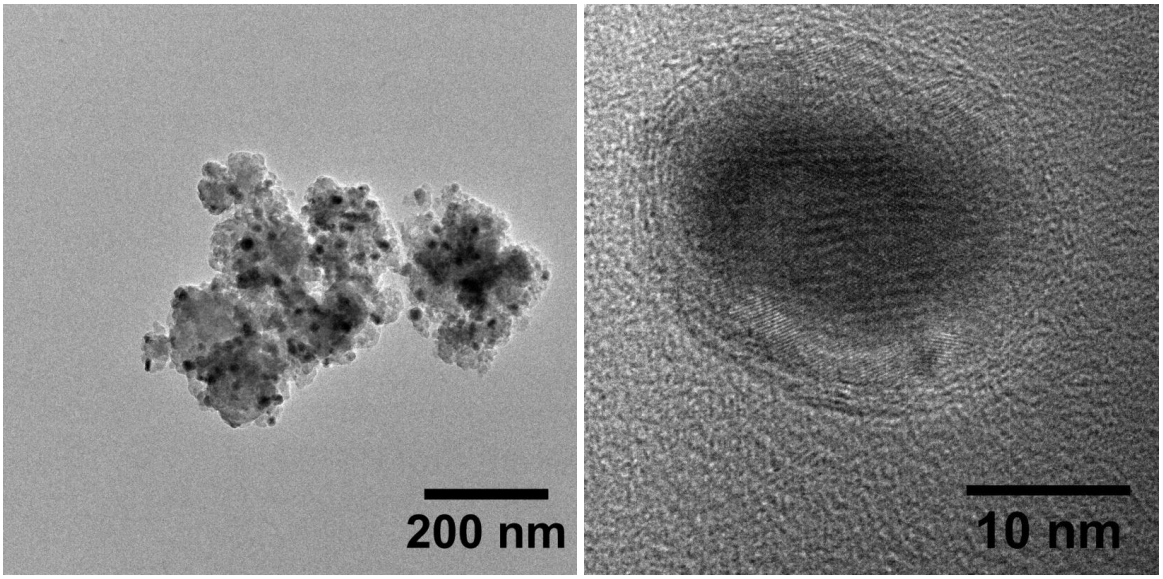

Figure 2.18: Left: TEM of the SiO_2-based composite treated at 300°C; right: HRTEM of a single particle.

The particles were somewhat larger (with an average diameter of 20 nm) than described in the literature,[38] but also gave no conclusive X-ray diffraction pattern (*vide infra*). EDX spectra of the particles were the same as reported in the literature[38] (Figure 2.19, left).

A line scan across the particle (Figure 2.19, right) showed a constant level of silicon and oxygen in the surroundings of and throughout the particles, because silica was the

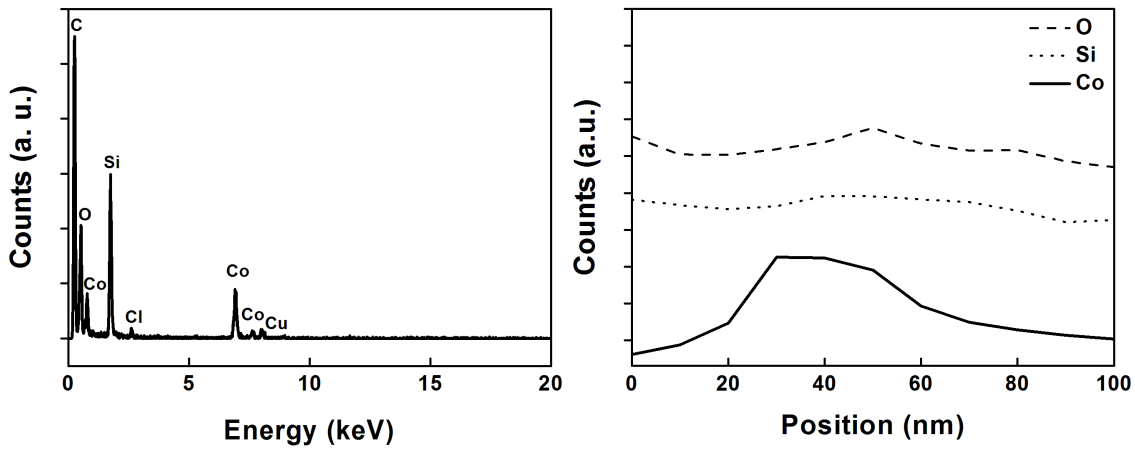

Figure 2.19: Left: EDX spectrum of a single nanoparticle in SiO_2; right: EDX line scan profile of a single nanoparticle in SiO_2.

support, while cobalt was only present in the particles. The carbon signal resulted from the used carbon grid (Figure 2.19, left).

The HRTEM pattern of a single particle confirmed its crystalline nature with a lattice spacing of ∼0.24 nm, which matched the spacing of the (100) plane of α-cobalt (0.22 nm). An amorphous shell surrounding the crystalline particle was visible, whose composition was not clear from the EDX line scans.

The oxidation state and chemical environment of the cobalt species were investigated by X-ray photoelectron spectroscopy (XPS). The survey spectrum of the material obtained after treating the precursor loaded silica sample at 300°C under H_2 is shown in Figure 2.20, in which all species of interest (Co, Si, C, O) are visible. Detailed spectra of the most important regions (O1s, C1s, Co2p, CoLMM, Co3p, Si2p, Si2s) for each element were also acquired and a quantitative analysis was performed. The thus obtained composition was O1s 68.3 at %, C1s 7.5%, Si2p 21.1%, and Co2p 3.1% (Si:Co ratio 6.8). The detected binding energies (BE) are reported in Table 2.8, together with the calculated Auger parameter for cobalt.[151]

Fitting of the Co2p region indicated the presence of several components assigned to cobalt species in different chemical environments (Figure 2.21).

The main components ascribed to the $Co2p_{3/2}$ region showed peaks at 780.2, 781.3, 786.2 and 788.4 eV. As expected, each of these components had the corresponding $Co2p_{1/2}$ component of the doublet shifted by about 15 eV with respect to $Co2p_{3/2}$.[152]

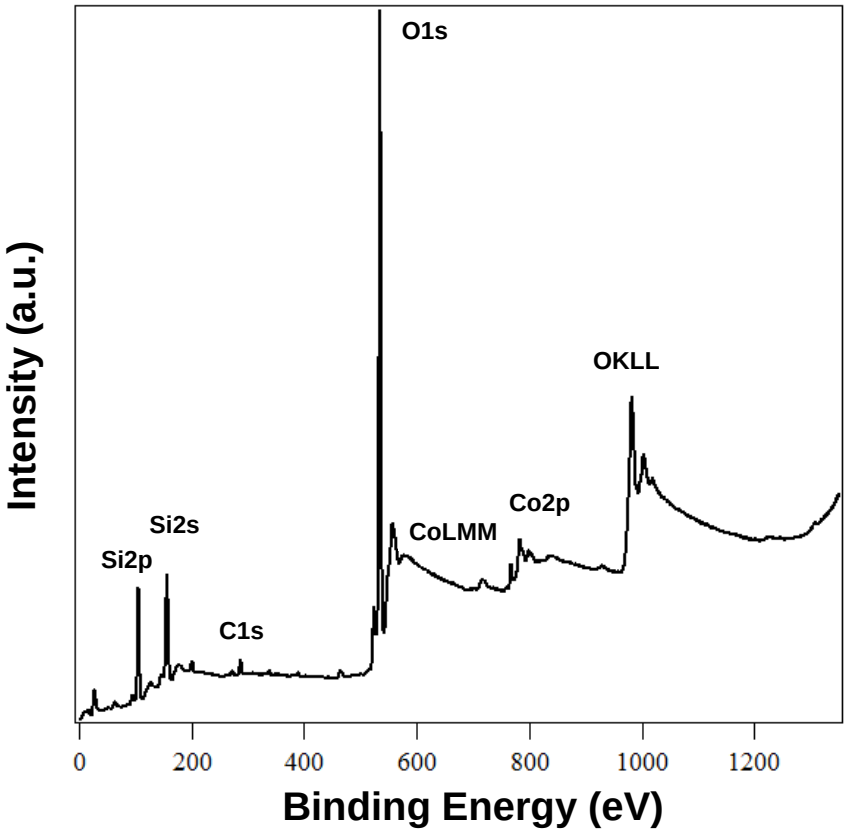

Figure 2.20: XPS survey spectrum of the material obtained after treating the precursor loaded silica sample at 300°C under H_2.

Table 2.8: Binding energies (BE) of the relevant species (values corrected for charging effects)

Region	BE (eV)
O1s	533.6
Si2p	103.3
Si2s	154.3
Co2p	See fitting below (Figure 2.21)
Co3p	60.8
CoLMM	715.2
CoLMM KE	771.4
Auger parameter	1552.7

Whereas the first two BE values can be ascribed to specific Co species, as discussed below, the latter two, shifted by about 6–7 eV with respect to the main component, were shake-up peaks.[153] The presence of shake-up peaks is typical of the presence of

Co(II); they were not observed for Co(III).

Furthermore, when comparing Co_3O_4 and CoO, the relative intensity of the satellite peak was stronger for CoO. These differences in the satellite peak were interpreted in terms of differences in the distribution of Co ions in tetrahedral and octahedral coordination sites in the subsurface region of Co_3O_4 and CoO.[154] The first component at 780.2 eV was assigned to the main spin-orbit component of Co2p in a Co(II) oxide, based on previous works on cobalt oxides.[153,155] The second component at 781.3 eV was assigned to $Co2p_{3/2}$ of Co(II) in Co_2SiO_4, with the $Co2p_{1/2}$ component at 797.0 eV. Accordingly, the corresponding shake-up peaks were detected at 788.4 ($Co2p_{3/2}$) and 804.0 eV ($Co2p_{1/2}$), respectively. The binding energy of $Co2p_{3/2}$ peak for Co silicate was reported to be 781.6 eV,[156] and that of $CoAl_2O_4$ 781.7 eV.[157,158]

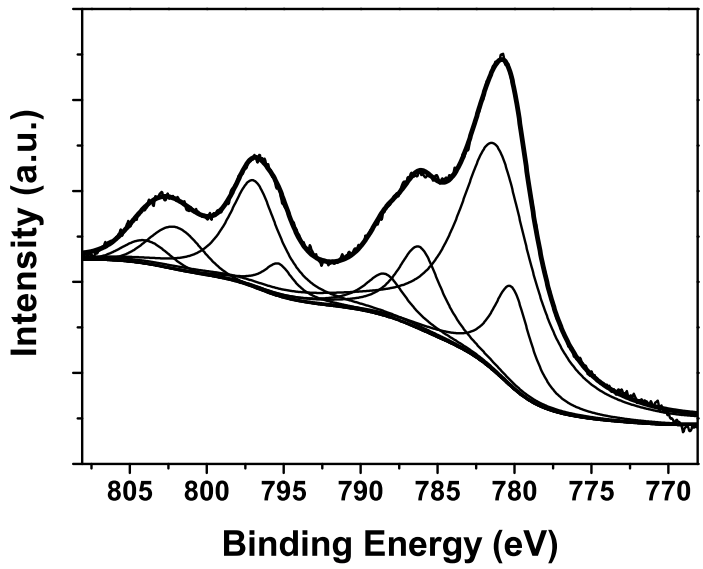

Figure 2.21: Deconvolution of the Co2p region in the XPS spectrum.

Nevertheless, this second component could also be ascribed to Co species involved in the interaction at the interface between silica and cobalt oxides, *i.e.* CoO/SiO_2. These results suggested that both Co_2SiO_4-like (or CoO/SiO_2) species and Co(II) oxide species were formed. The experimentally determined Auger parameter[151] of this main component was found at 1552.7 eV. The absence of cobalt silicides was supported by the BE of the Si2p, which is 103.3 eV, a value much higher than that expected for cobalt silicide (99.6 eV).[159] and similar to the values reported for silica (103.6 eV) and

silicate species (103.2–103.5 eV).[152] The BE value for O1s (533.6 eV) was much higher than that expected for Co(II) oxide species (529.6–530.0 eV), but this finding can be attributed to the prevalence of silica or silicates over cobalt-based species (Si:Co = 6.8:1).

To obtain crystalline phases more suitable for analyses by powder X-ray diffraction, the sample was heated at 600°C under N_2 flow. The notion was that the particles would become bigger by annealing, whatever their composition was; cobalt silicides, if present, would not decompose at this temperature.[160] After this heat treatment, the diffraction pattern for hexagonally close-packed α-cobalt (PDF 01-1278) was clearly observed (Figure 2.22, right). The observed pattern was assigned to the (100), (002) and (101) reflexions.

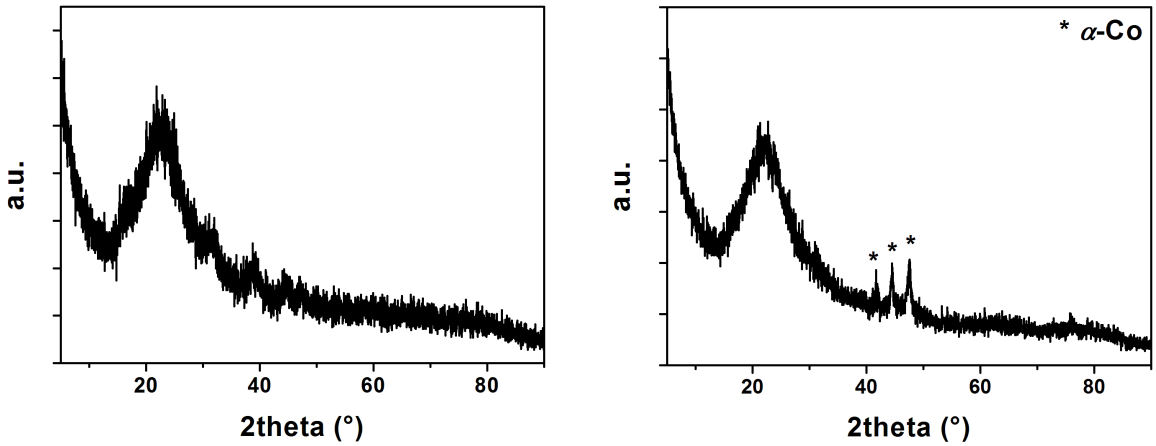

Figure 2.22: Diffraction pattern of the composite thermolysed at 300°C under H_2 (left), and after heating at 600°C under N_2 (right). The reflexions of α-cobalt are marked with an asterisk.

Further heating under N_2 to 1000°C resulted in the formation of the high temperature phase, face-centred cubic β-cobalt (Co, PDF 15-0806), a crystalline cobalt silicate phase (Co_2SiO_4, PDF 15-0865) and cubic cobalt oxide (CoO, PDF 78-0431) (Figure 2.23).

The nanoparticles formed upon thermolysis of $Co(CO)_4SiCl_3$ adsorbed on silica in a hydrogen atmosphere are metallic cobalt nanoparticles with a Co_2SiO_4/CoO shell. The reason why metallic cobalt was not detected by XPS is due to the fact that this method is surface-sensitive (because of the low average free path of the emitted photoelectrons) and therefore only the Co_2SiO_4/CoO shell was detected. Annealing of the composite at higher temperatures resulted in particles big enough to be characterised by powder XRD. Decomposition of initially formed Co silicide particles can be excluded, because

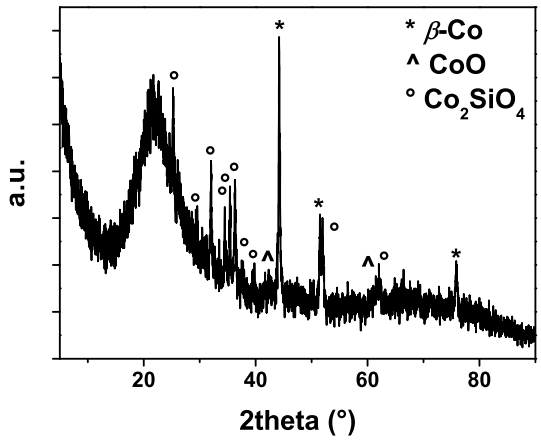

Figure 2.23: Diffraction pattern of Co, CoO and Co_2SiO_4 in SiO_2 after heat treatment at 1000°C under N_2.

Co silicides do not decompose, or react with silica, at the applied temperatures. XPS investigations showed that the oxide/silicate species were already present after H_2 treatment at 300°C, although in an amorphous state or in a thin layer, not detectable by XRD.

2.4.2 Thermal Decomposition of $Co(CO)_4SiCl_3$ Adsorbed on Charcoal

The formation of metallic Co nanoparticles was also observed, when $Co(CO)_4SiCl_3$ was deposited on charcoal and thermolysed under the same conditions (300°C, H_2 atmosphere). The powder X-ray diffraction pattern (Figure 2.24) clearly exhibited α-cobalt, as in the case of silica as the support. The single reflection at 26.71 was assigned to SiO_2 formed during the reaction from the $SiCl_3$ ligand.

TEM investigations indicated the presence of cobalt nanoparticles in the carbon matrix without an amorphous shell (Figure 2.25). An EDX line scan (Figure 2.26) showed again constant silicon and oxygen counts (but of lower relative intensity) in the surroundings of and throughout the particles, as in the case of the silica support. This result proved that the oxygen from the Co_2SiO_4/CoO shell in the case of the silica support was not an artefact from unintentional oxidation during sample preparation for TEM or EDX (then the particles on charcoal should also have an oxide shell), but

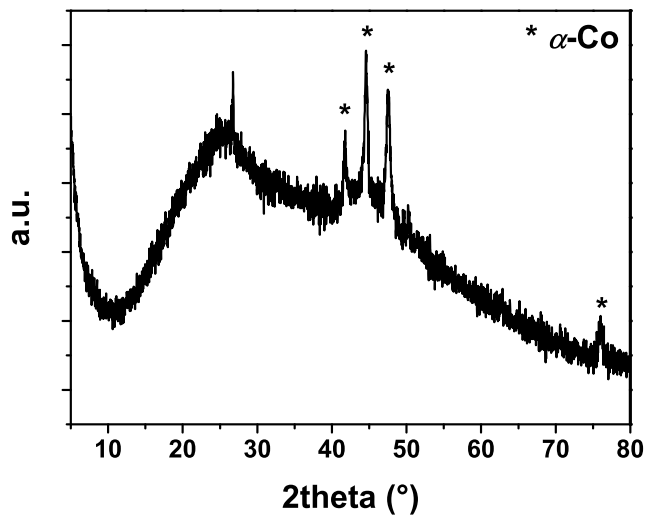

Figure 2.24: Diffraction pattern of Co nanoparticles on charcoal after thermolysis at 300°C under H_2.

must be due to the silica support. The particles were again about 20 nm large.

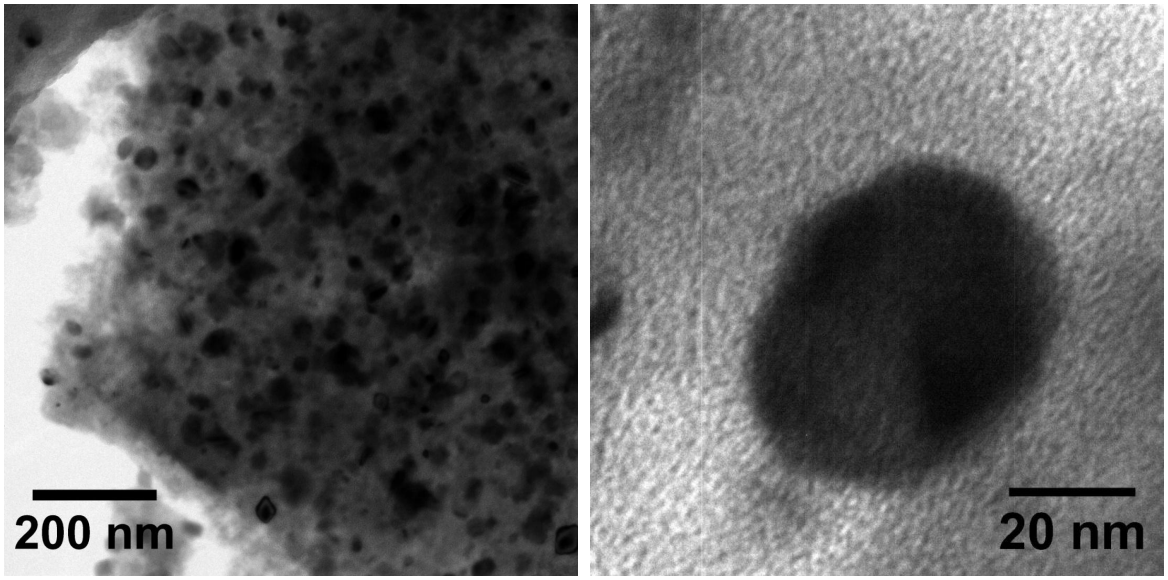

Figure 2.25: Left: TEM of the Co/charcoal nanocomposite after treated at 300°C; right: HRTEM of a single particle.

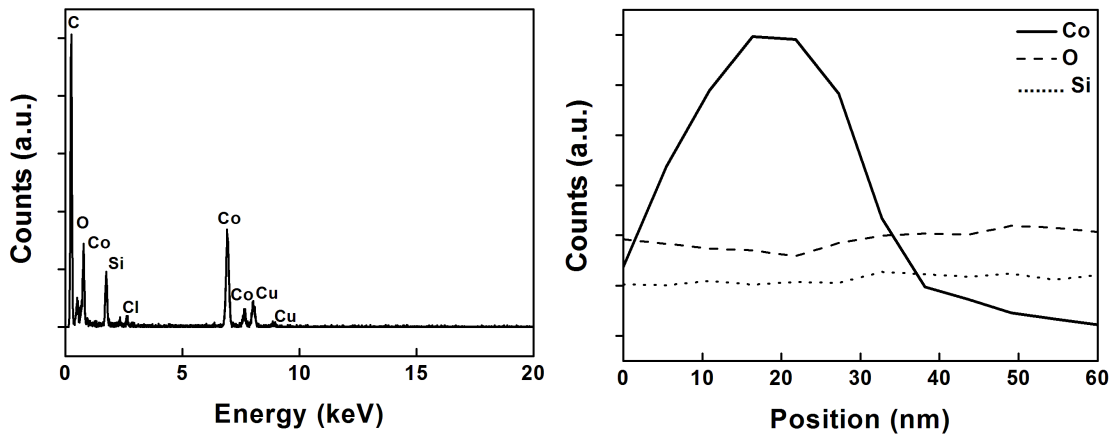

Figure 2.26: Left: EDX spectrum of a single nanoparticle in charcoal; right: EDX line scan profile of a single nanoparticle in charcoal.

2.4.3 Thermal Decomposition of $Co(CO)_4SiCl_3$ Adsorbed on Graphite

The ideal structure of graphite consists of layers composed of hexagonally arranged carbon atoms, bound together by weak van der Waals interactions. The carbon atoms are covalently bound to three neighbouring carbon atoms, through sp^2-sp^2 axial hybrid orbital overlap. Due to its unique structure we were interested whether the single-source precursor $Co(CO)_4SiCl_3$ also decomposed to cobalt nanoparticles with concomitant intercalation in the graphite layers. The complex was deposited on graphite by the same method as above. The material was also treated with the same temperature program under hydrogen atmosphere.

It was not possible to observe a significant crystalline phase by X-ray diffraction, apart from the crystalline phase of hexagonal graphite (JCPDS PDF 65-12-0212).

Patterns revealed by TEM measurements presented very small nanoparticles of about 5 nm distributed in the supporting graphite (Figure 2.27).

Further EDX line scans of a single particle indicated the presence of cobalt, silicon and oxygen. The cobalt content raised over the particle, which implied a pure cobalt phase and the silicon and oxygen content must stem from the matrix (Figure 2.28). In the light of previous results obtained for the complex $Co(CO)_4SiCl_3$, there is strong evidence that the formed particles are cobalt particles in graphite. The silicon and

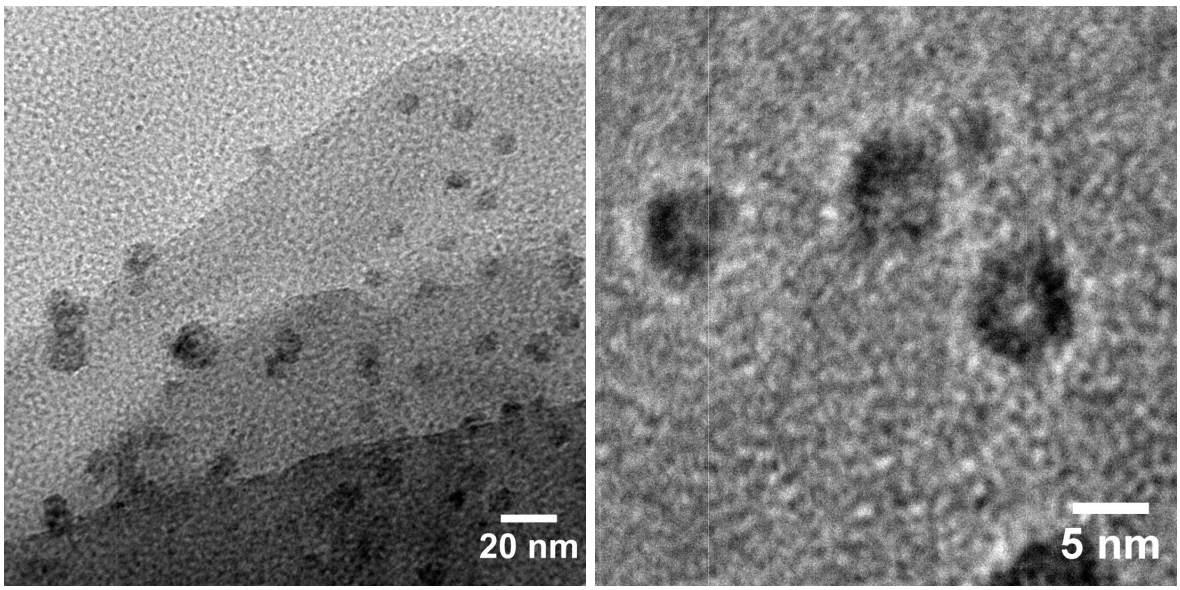

Figure 2.27: Left: TEM of the Co/graphite nanocomposite after treated at 300°C; right: HRTEM of particles.

oxygen content observed by EDX can be attributed to the decomposition of the $SiCl_3$ ligand, which results in the formation of a SiO_2 layer on the material.

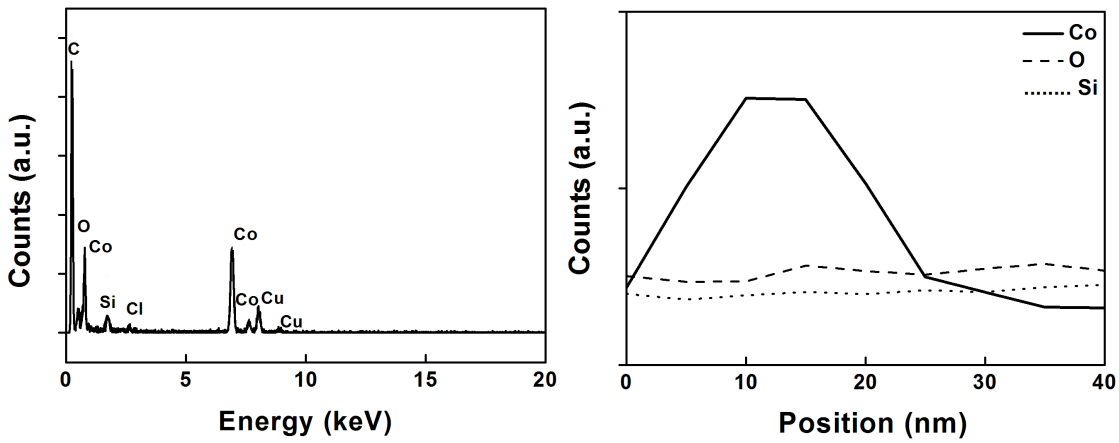

Figure 2.28: Left: EDX spectrum of a single nanoparticle in graphite; right: EDX line scan profile of single nanoparticles in charcoal.

These experiments support the conclusion, that while $Co(CO)_4SiCl_3$ might be an excellent single-source precursor for the growth of silicide nanowires under CVD conditions, it is not applicable for formation of silicide nanoparticles. A formation of cobalt nanoparticles was observed, independent of the used supporting material. If silica was used as a carrier, a Co_2SiO_4/CoO shell was generated, which was directly visible in the

HRTEM pattern.

2.4.4 Attempted Cobalt Particle Formation by a Sol-Gel Route

We tried to synthesise cobalt nanoparticles by a well known sol-gel route from Schubert and co-workers.[161,162] With this method, nanometer-sized metal particles with a narrow particle size distribution, homogeneously dispersed in a SiO_2 matrix were obtained. A series of metal salts were incorporated in a sol-gel matrix with aid of silanes $X(CH_2)_3Si(OR)_3$ (R = methyl, ethyl; X = NH_2, CN, $H_2NCH_2CH_2NH$). Depending on the choice of functional groups, a variety of stable complexes with most transition metals can be synthesised. Consequently, three distinct steps are necessary to yield metal/SiO_2 nanocomposites (Figure 2.29):

1. sol-gel processing of metal complexes.
2. oxidation of the resulting polycondensates at elevated temperatures.
3. reduction of the metal oxide particles at elevated temperatures.

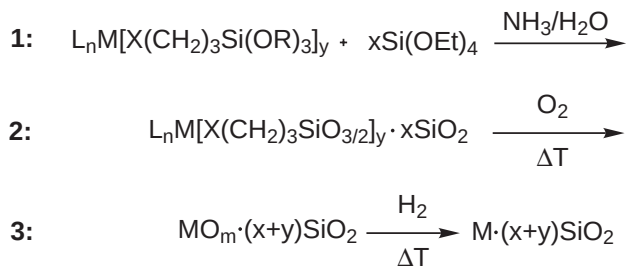

Figure 2.29: Three step route towards metal/SiO_2 nanocomposites.

The motivation to attempt the synthesis of cobalt nanoparticles stemmed from the need to obtain a reference material for the dibenzotiophene conversion tests described in Section 2.8. We proceeded as explained in the literature,[161,162] but after the last step (*i.e.* reduction of the metal oxide particles at elevated temperatures) no significant change of the blue colour of the nanocomposite after reduction treatment was recognised.

This indicates that no complete reduction could take place under these conditions. This can be explained by the existence of micropores in the sample before reduction

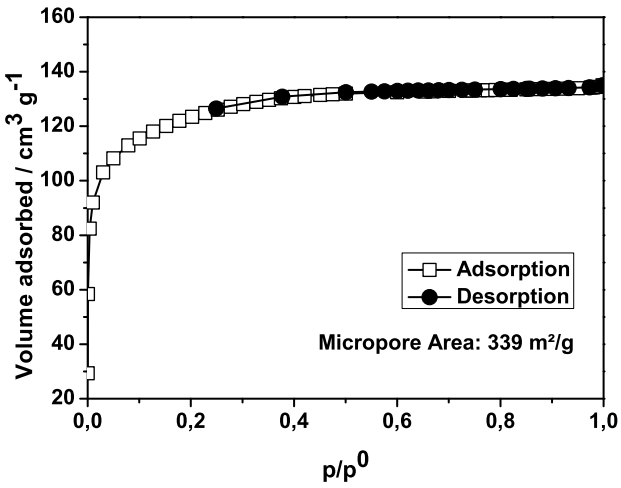

Figure 2.30: N_2 sorption measurements at 77 K of the sol-gel sample before reduction procedure.

treatment (Figure 2.30). The obtained isotherms are type I according to IUPAC classification and therefore characteristic of microporous materials.[163] The surface area was 339 m^2/g. Due to the small pores, the H_2O produced during reduction of CoO cannot be removed easily.[164] Higher temperatures might be necessary for complete CoO reduction.

Characterisation of the materials before and after reduction by XRD patterns gave no indication of crystalline phases, either due to the formation of too small cobalt particles or even clusters, or the whole composite being amorphous. The resolution of the used TEM was not high enough to locate any formed nanoparticles.

The oxidation state and chemical environment of the cobalt species in the two samples were investigated by X-ray photoelectron spectroscopy (XPS) in order to distinguish between the presence of different cobalt species in the materials.[153] In Figure 2.31, the survey spectrum of the sol-gel derived sample after H_2 treatment is reported, in which all species of interest (Co, Si, C, O) can be seen. From the detailed spectra of the most important regions (O1s, C1s, Co2p, Si2p), the atomic composition of the sample could be determined, as reported in Table 2.9.

Evidently, both samples exhibit very similar atomic compositions. Concerning the chemical state of the different species, the detected BE (including corrections for charging effects) are reported in Table 2.10.

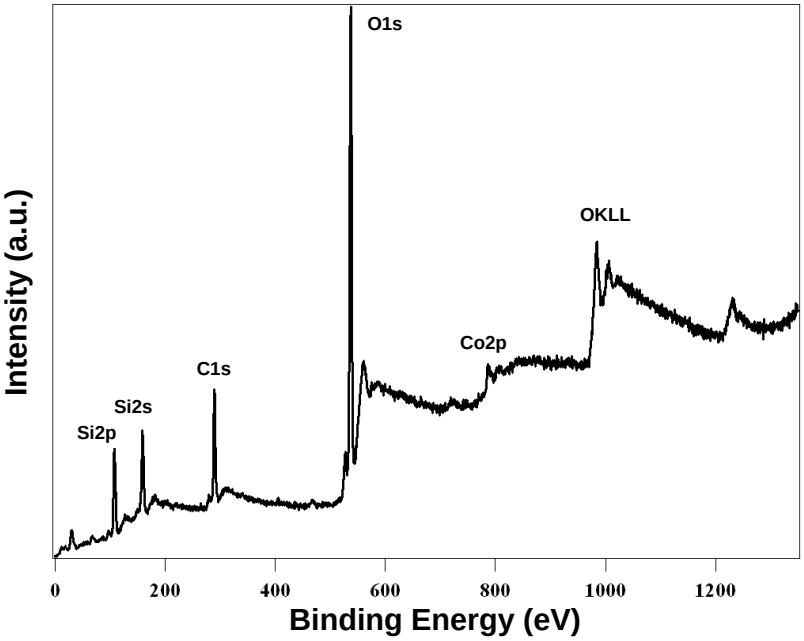

Figure 2.31: XPS survey spectrum of the material obtained by sol-gel process after H_2 treatment.

Table 2.9: Atomic percentages delivered by XPS analysis.

sol-gel sample before H_2 treatment	**atomic %**	**sol-gel sample after H_2 treatment**	**atomic %**
O1s	49.0	O1s	47.8
C1s	31.5	C1s	31.9
Si2p	18.2	Si2p	18.2
Co2p	1.6	Co2p	2.1
Si/Co	8.8	Si/Co	8.7

Concerning cobalt, the Co2p region displayed the main peaks for each of the $Co2p_{3/2}$ and $Co2p_{1/2}$ components, as reported in Table 2.10, separated as expected by about 15.8–16.0 eV, and the corresponding shake-up peaks, as evidenced by the fittings reported in Figure 2.32.

The BE value of the main peak for the H_2-treated sample (the values for untreated sample are enclosed in parentheses) at 781.8 eV (781.9 eV), and the observation of shake-up peaks, gave a hint for the presence of Co(II), although these high values could not be ascribed to Co(II) in CoO or either in Co_3O_4. The reported BE of Co2p for CoO and Co_3O_4 are 780.2–781.2 eV and 779.3–780.7 eV, respectively.[153,155,165] The additional presence of shake-up peaks were not significant for species identification.

Table 2.10: BE values of the relevant species (already corrected for charging effects).

sol-gel sample before H_2 treatment	**BE (eV)**	**sol-gel sample after H_2 treatment**	**BE (eV)**
O1s	532.3	O1s	532.5
Si2p	103.0	Si2p	103.2
Si2s	154.1	Si2s	154.1
$Co2p_{3/2}$	781.9	$Co2p_{3/2}$	781.8
$Co2p_{1/2}$	797.7	$Co2p_{1/2}$	797.9
$Co2p_{3/2}$ (shake-up)	787.1	$Co2p_{3/2}$ (shake-up)	786.5
$Co2p_{1/2}$ (shake-up)	803.3	$Co2p_{1/2}$ (shake-up)	803.5

The existence of shake-up peaks is symptomatic for Co(II) in CoO and Co_3O_4 (not for Co(III)). Okamoto's group[166] reported BE values of about 781.3–781.9 eV for Co(II) species in a CoO/SiO_2 system, which depend on the CoO concentration.

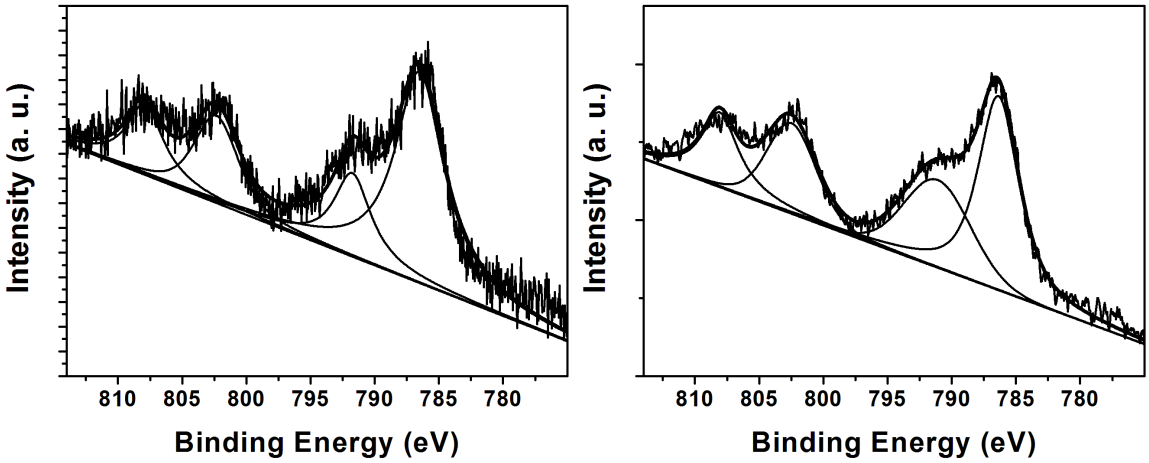

Figure 2.32: Deconvolution of the Co2p region of the samples before (left) and after (right) H_2 treatment.

Mekki *et al.*[167] investigated cobalt sodium silicate glasses with the chemical composition $(0.3)Na_2O$-$(0.70\text{-}x)SiO_2$-xCoO for $0.0 \leq x \leq 0.2$ and they assigned BE values for Co2p in the range of 780.1–780.5 eV. Considering the observed BE values, no metallic cobalt was present in the samples, which would be expected to be 778.1–778.5 eV.[152] In order to assign the Si species, the BE value of Si2p was found to be 103.2 eV (103.0 eV), which is similar to the reported numbers for silica (103.6 eV) and silicate species (103.2–103.5 eV).[152]

As a consequence, we assume the presence of Co(II) in an oxygen environment (either CoO or Co_2SiO_4) in a silica matrix. Furthermore, the chemical composition of both samples were very similar, leading to the conclusion that a hydrogen treatment at 500°C for 2 h did not affect the sol-gel derived cobalt-containing material. As mentioned above, the formed micropores during sol-gel procedure complicated the H_2O desorption during hydrogen treatment of the cobalt oxide or silicate in the sample. It appears to be reasonable to suggest application of higher temperatures and longer reduction times for metallic cobalt formation.

2.5 Transition Metal Silicide Nanocomposites

2.5.1 Iron Silicide

While it turned out that $M(CO)_n(SiCl_3)_m$ complexes are suitable for transition metal silicide nanowire formation under CVD conditions on a substrate, they are not applicable for nanoparticle formation in a matrix. Those circumstances led to the application of other single-source precursors: organometallic polymers containing both the desired metal and silicon.

Formation of Fe_3Si and Fe_5Si_3 nanoparticles derived from polymer **B** and **C** (Figure 2.33) has not been reported so far (see Introduction 1.3). We were able to tune the size and composition of the formed particles by the choice of polymer and the thermolysis conditions.

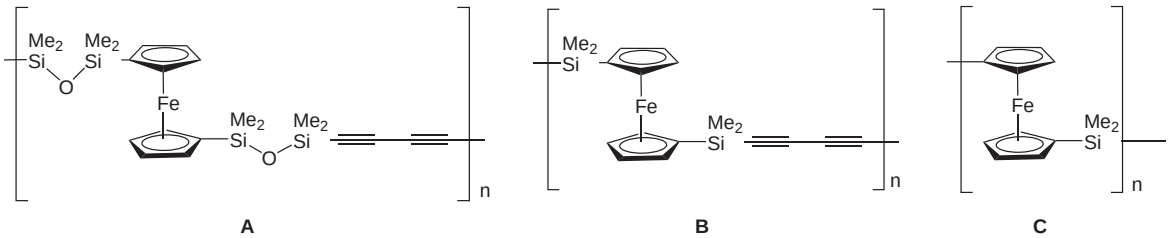

Figure 2.33: Structural formula of the polymers.

All thermolysis experiments were carried out in a split tube furnace equipped with a gas flow controller under nitrogen atmosphere (flow rate 200 mL/min) at maximum temperatures of either 850°C or 1000°C. Three different temperature programs were applied. In each case, the temperature was raised to the specified temperatures with

a heating rate of 10°C/min and then held at these temperatures for the specified time period.

Program **I**: (i) 250°C for 1 h, (ii) 400°C for 1 h, (iii) 850°C for 3 min.

Program **II**: (i) 250°C for 1 h, (ii) 400°C for 1 h, (iii) 1000°C for 3 min.

Program **III**: 1000°C for 4 h.

For further reference, the labels of the pyrolysed samples consist of the abbreviation used for the polymer followed by a roman numeral indicating the pyrolysis temperature program. For example, **BII** is the material resulting from pyrolysis of polymer **B** with temperature program **II**.

The original procedure for the synthesis of iron silicide nanoparticles in a matrix stems from Keller's group,[86] where they used polymer **A** and applied different heating programs. We started with the same heat treatment as reported in the literature, *i.e.* program **II** on polymer **A** and were able to obtain Fe_5Si_3 nanoparticles in a SiC/C matrix. It is noteworthy that polymer **A** did not result in iron silicide formation when a lower temperature was applied. If program **I** was used for thermolysis of polymer **A**, crystalline phases of Fe_3C (JCPDS PDF 34-0001), austenite (Fe, C) (JCPDS PDF 31-0619) and cubic Fe (JCPDS PDF 01-1262) were observed (Figure 2.34).

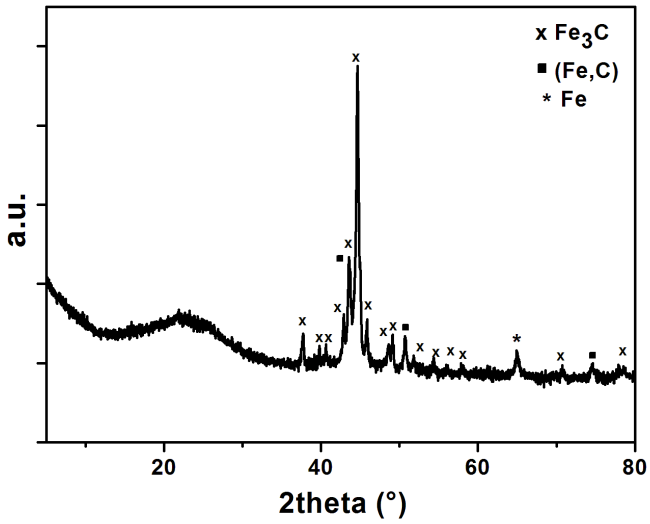

Figure 2.34: XRD pattern of **AI**.

To gain more insights into the structure of the obtained products, TEM patterns were recorded (Figure 2.35, left). Large particles were observed in a matrix. EDX line scans

on several particles showed an increased iron but no silicon content (Figure 2.35, right). We assume that no iron silicon nucleation was feasible thermodynamically at the lower temperature. The thermolysis at 850°C of polymer **A** led to material **AI**, which might be an intermediate product for the formation of iron silicides.

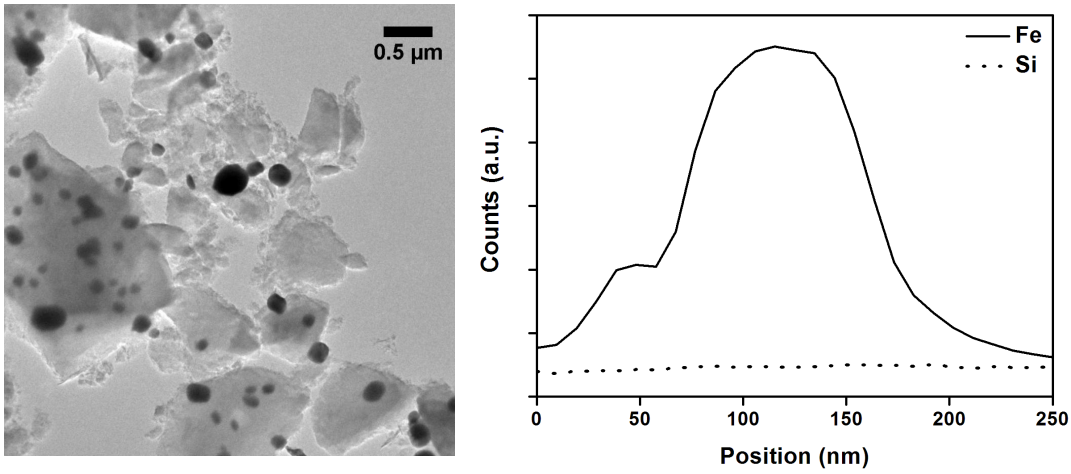

Figure 2.35: Left: TEM pattern of **AI**; right: EDX line scan profile of a single particle of **AI**.

Based on these results, the size of the spacer $[-SiMe_2 - O - SiMe_2- \equiv - \equiv -]$ in the polymer was reduced systematically. Initial removal of the $[-SiMe_2 - O - SiMe_2-]$ moiety, which led to polymer **B** and subsequent removal of the $[- \equiv - \equiv -]$ moiety yielded the easily accessible poly(ferrocenylsilane) (polymer **C**). Different heating protocols were applied to investigate the influence of the heating rate and the maximum temperature on the composition of the formed composites.

The analytically obtained iron content of polymer **B** was higher in both cases (**BI** 26.7 wt%, **BII** 26.2 wt%) as expected from stoichiometric calculations due to the loss of CH_4 and H_2 during heat treatment. Thermolysis of **B** at two different maximum temperatures led to two different iron silicide phases: whereas Fe_3Si was formed with program **I** (maximum temperature 850°C), metastable Fe_5Si_3 was formed with program **II** (maximum temperature 1000°C). The XRD pattern of **BI** clearly exhibited diffraction peaks of the cubic phase of Fe_3Si (JCPDS PDF 35-0519; space group Im-$3m$). The diffraction pattern of **BII** was assigned to hexagonal Fe_5Si_3 (JCPDS PDF 38-0438, space group $P63/mcm$, Figure 2.36). Both XRD patterns displayed broad reflexions at about 25.9° for graphite (JCPDS PDF 75-1621). For sample **BII**, an additional reflexion can be assigned at 35.7° for SiC (JCPDS PDF 22-1273, space group

*P*63*mc*). This supported the formation of a carbon and silicon carbide matrix during thermolysis (as carbon and silicon is released from the polymer).[83]

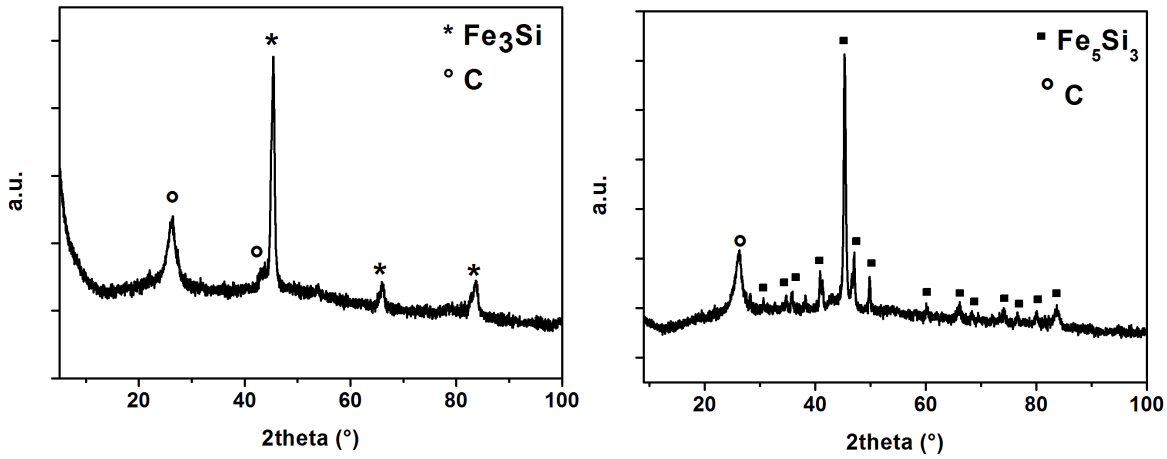

Figure 2.36: XRD pattern of **BI** (left) and of **BII** (right).

The kinetics of the thermolysis of polymer **A**, which also led to formation of either Fe_5Si_3 (at faster thermolysis rates of 10°C/min) or bcc-Fe (at lower thermolysis rates, 1°C/min), have been discussed in detail by Keller *et al.*[86] They also observed formation of metastable Fe_5Si_3 at higher temperatures. The Fe_3Si phase was generated subsequent to the formation of FeSi, which is the first silicide phase among the possible iron silicide products due to its favourable ΔG_V (*i.e.* change in free energy per unit volume or driving force for nucleation).[168] Metastable Fe_5Si_3 formed only when it was easier to nucleate than the thermodynamically more stable phase.[169] The metastable phase was stabilised due to the impact of carbon and the higher temperature on ΔG_V and γ (interfacial free energy), and consequently on the thermodynamic barriers associated with the diffusion and nucleation of Fe and Si reactants.

Average particle sizes were calculated from the width of the (110) reflexion (in **BI**) and the (211) reflexion (in **BII**) according to Scherrer's equation.[170] A value of about 20 nm was obtained for sample **BI** and about 40 nm for sample **BII**.

To gain more insights into the nanoscale structure of the powders, TEM measurements were performed. There was a significant difference between samples **BI** and **BII**, not only regarding their phase composition but also their morphology, though both originate from the same polymer precursor. The TEM pattern (Figure 2.37) of sample **BI** displayed well-distributed nanoparticles in a size range of 10–20 nm, which corresponds to the average particle size obtained from XRD (*vide supra*).

The particles were encapsulated in a matrix, which apparently consisted of SiC and C. The chemical composition of the particles and the matrix were analysed by EDX line scans. They confirmed the existence of Fe and Si in the particle and Si for the matrix. Figure 2.38 shows the line scan for sample **BI**, the line scans for all other samples reported in this section were similar and are not reproduced. A closer look at sample **BII** (Figure 2.37) revealed particles with a broad size distribution which are furthermore not as well-distributed as in sample **BI**. The EDX line scan (not shown) again confirmed the existence of Fe and Si in the particles and gave evidence to the formation of a SiC matrix.

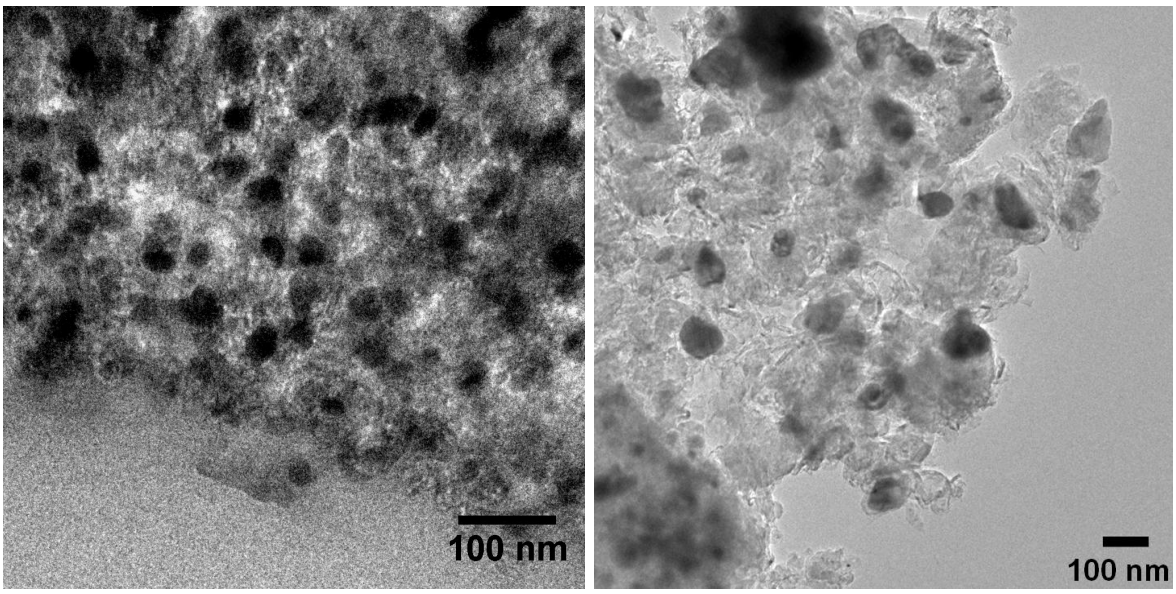

Figure 2.37: TEM pattern of **BI** (left) and of **BII** (right).

The molar Fe:Si ratio for polymer **C** was 1:1, *i.e.* the silicon content was lower compared to polymer **B** (1:2), which was in turn responsible for the higher observed iron content (39.8 wt% in **CII** and 50.9 wt% in **CIII**). A mass loss of 78% took place during the reaction, due to volatilisation of impurities (ferrocene) and formation of molecular depolymerisation products,[88] which were deposited as an orange sublimate on the cooler parts of the tube.

Compound **C** was thermolysed at 1000°C with different heating rates (program **II** and **III**, the latter reproducing the conditions used by Manners *et al.*[87,88]). Intriguingly, an Fe_3Si phase was obtained in both cases, together with graphite, as identified by the XRD patterns (Figure 2.39). As mentioned in the introduction, linear and hyperbranched poly(ferrocenylsilane) have been reported as organometallic polymeric precursors for iron particle formation.[87–89] In those cases, however, polymers of high

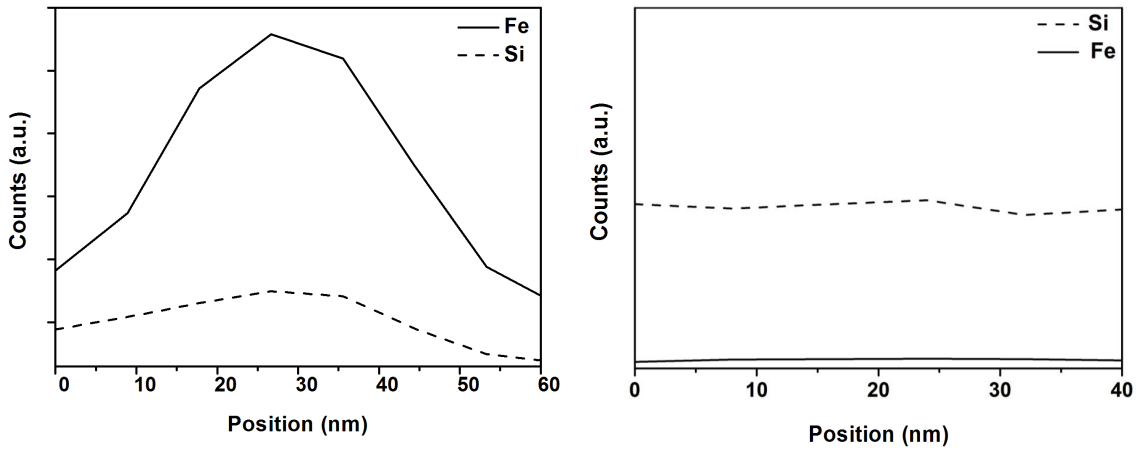

Figure 2.38: EDX line scans of particle (left) and matrix (right) of **BI**.

molecular mass were employed, typically in the range M_w = 15000–20000 and M_n = ∼10000. In our work, only oligomeric **C** was used as precursor (M_w = 1739, M_n = 1143 as analysed by GPC). We tentatively assume that silicon can be released more easily from silicon-containing end-groups than from silicon incorporated in a polymer chain, which may lead to the observed Fe_3Si formation.

The fact that Fe_3Si was obtained by thermolysis of **C** at 1000°C while Fe_5Si_3 was obtained from **B** under the same conditions also supports the assumption[86] that the carbon produced during the reaction is responsible for the formation of metastable Fe_5Si_3 (besides the higher temperature). Due to the shorter organic spacer in **C**, less carbon can be released.

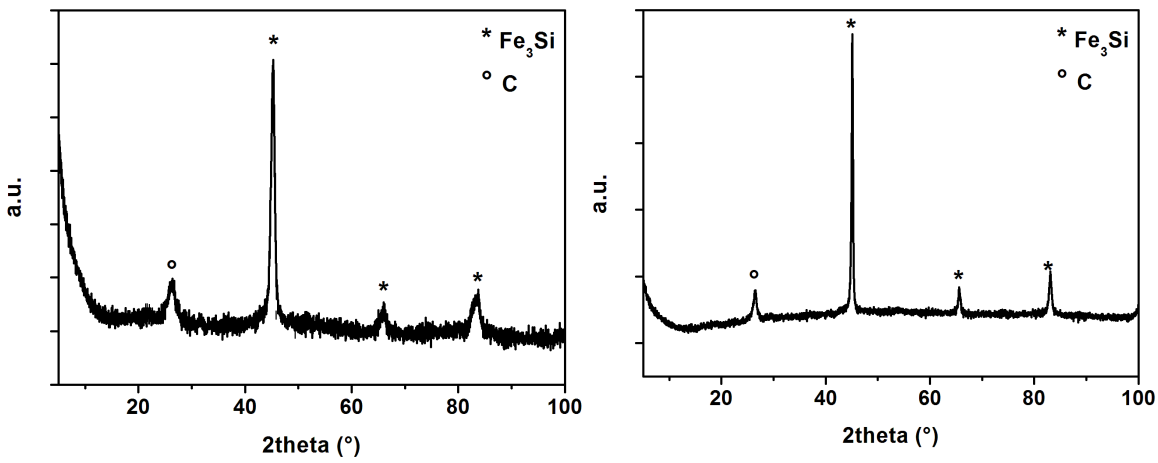

Figure 2.39: XRD pattern of **CII** (left) and **CIII** (right).

The (110) reflexion was employed to calculate average crystallite sizes for **CII** and **CIII**. Smaller values of about 12 nm were obtained for **CII** and larger crystallites for **CIII** (about 44 nm). Further evidence for the existence of smaller particles in **CII** and larger ones in **CIII** was obtained from TEM. Figure 2.40 (left) displays well-distributed particles encapsulated in a SiC/C matrix. The particles were not spherical and their size was in the range of 10–100 nm. The EDX line scans across the particle and the matrix again revealed Fe and Si in the particle (Figure 2.41, left) and only Si in the matrix.

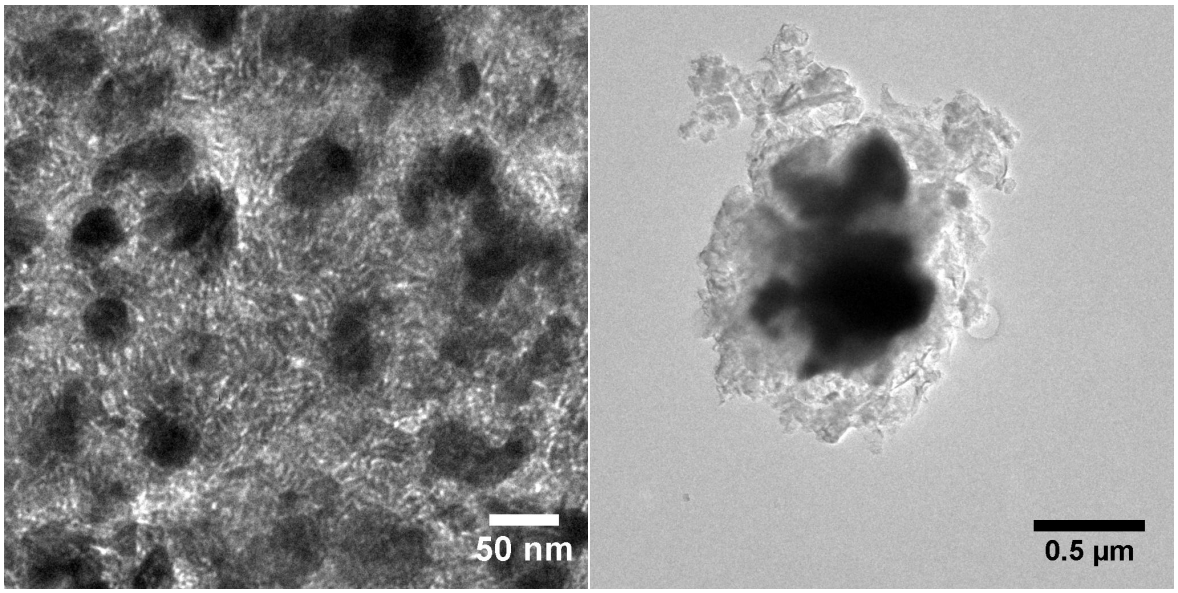

Figure 2.40: TEM patterns of **CII** (left) and **CIII** (right).

It is apparent that a longer heat treatment of polymer **C** resulted in larger crystallite sizes. The longer time period apparently favoured agglomeration/aggregation of the previously formed smaller particles as calculated from the XRD line width and apparent in Figure 2.40 (right). The TEM pattern exhibited large particles of about 0.6 μm still surrounded by a SiC/C matrix. Their chemical composition was again analysed by EDX line scans, which showed the presence of Fe and Si in the particle (Figure 2.41, right) and only Si in the matrix.

If the polymer **C** was thermolysed at lower temperatures (850°C) with program **I**, the formation of cubic Fe (JCPDS PDF 87-0722) resulted, as evidenced by XRD. Particle formation was also confirmed by TEM patterns and EDX line scan profiles. These results indicate that more than 850°C are necessary to achieve nucleation of Fe and Si of polymer **C**. In contrast to the thermolysis experiments with polymer **B**, the acetylene

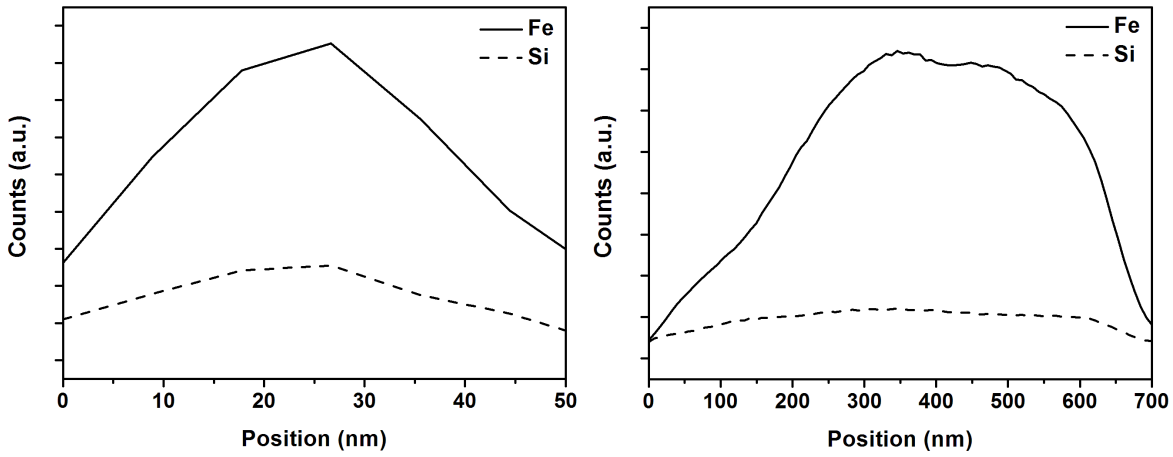

Figure 2.41: EDX line scan profile of a single particle of **CII** (left) and **CIII** (right).

group may positively influence the iron silicide formation.

We obtained Fe_3Si and Fe_5Si_3 nanoparticles in a SiC/C matrix of varying size, tunable by different temperatures and choice of organometallic precursors. We have shown that the carbon content of the polymer chains (polymer **B**) and higher temperature, supported the formation of thermodynamically metastable Fe_5Si_3. At lower temperatures, the same polymer **B** yielded the more stable Fe_3Si phase in the form of smaller and well-distributed nanoparticles encapsulated by SiC/C. Increasing the temperature alone did not lead to larger Fe_3Si particles but instead to the formation of a Fe_5Si_3 phase. Gratifyingly, lowering the carbon content of the polymer chains (polymer **C**), led to the possibility of obtaining larger Fe_3Si nanoparticles even at higher temperatures.

Raman spectroscopy measurements were performed for samples **BI**, **BII**, **CII**, **CIII** in order to additionally characterise the formed carbon species. Figure 2.42 shows Raman spectra for all samples, which were characteristic of an undisturbed graphitic lattice. For all measurements, a band at $\sim$1580 cm^{-1} was assigned to an ideal graphitic lattice vibration mode with E_{2g} symmetry. Such spectra are generally observed for highly oriented polycrystalline graphite and for single graphitic crystals, whose edge length parallel to the graphene layers is larger than 100 nm. An additional first-order band was visible at $\sim$1360 cm^{-1}, corresponding to a graphitic lattice vibration mode with A_{1g} symmetry. Another first order band could be observed at $\sim$1620 cm^{-1} which appeared as a small shoulder on the G band (ideal graphitic lattice, E_{2g}-symmetry) while the D2 band corresponded to a disordered graphitic lattice in surface graphene layers, again

with E_{2g}-symmetry.[171]

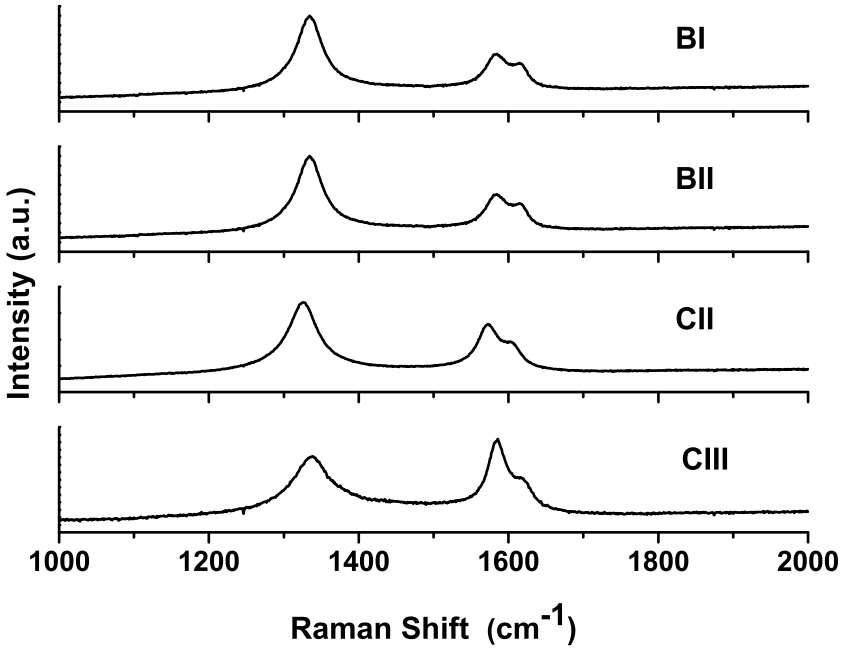

Figure 2.42: Raman spectra of thermolysed samples.

The application of poly[(silylene)diacetylene] as a precursor for formation of β-SiC-containing materials in high yields under argon at temperatures up to 1400°C has been demonstrated in detail by the group of Corriu.[82] Two main features of the thermolysis procedure have been discussed:

- cross-linking of the diacetylene groups at about 300°C led to a stabilised sp^2-ultrastructure network; SiC formation took place in the amorphous carbon matrix.
- silicon content before and after heat treatment was the same; the detected weight loss stemmed from CH_4, H_2 and C_2H_4 removal.

Successful complexation reactions of bis(trimethylsilylene)diacetylene with $Fe_2(CO)_9$ under UV irradiation have already been observed by Pannell *et al.*[172] Red crystalline $[Fe(CO)_3\{C_4CO(SiMe_3)_2\}]_2$ was obtained, whose IR spectrum exhibited acetylene and carbonyl bands of the polymer and the complexed iron carbonyl compound (2073 (C≡C) , 2047, 2018 (C≡O), 1652 (C=O) cm^{-1}) with the following structure (Figure 2.43).

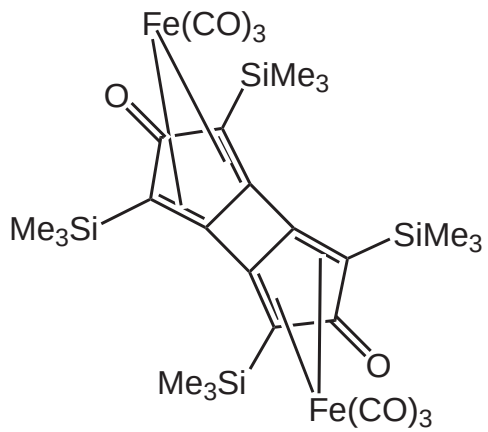

Figure 2.43: Structure of $[Fe(CO)_3\{C_4CO(SiMe_3)_2\}]_2$.

Comparing the infrared spectra of products obtained from the reaction between poly-[(silylene)diacetylene] and $Fe_2(CO)_9$, similar bands were observed and assigned. The bridged CO group of $Fe_2(CO)_9$ (1821 cm^{-1}) disappeared completely (see Section 4.4.13). This result led us to assume the following reaction product, in analogy with the structure shown in Figure 2.43, named polymer **D** (Figure 2.44) for further reference.

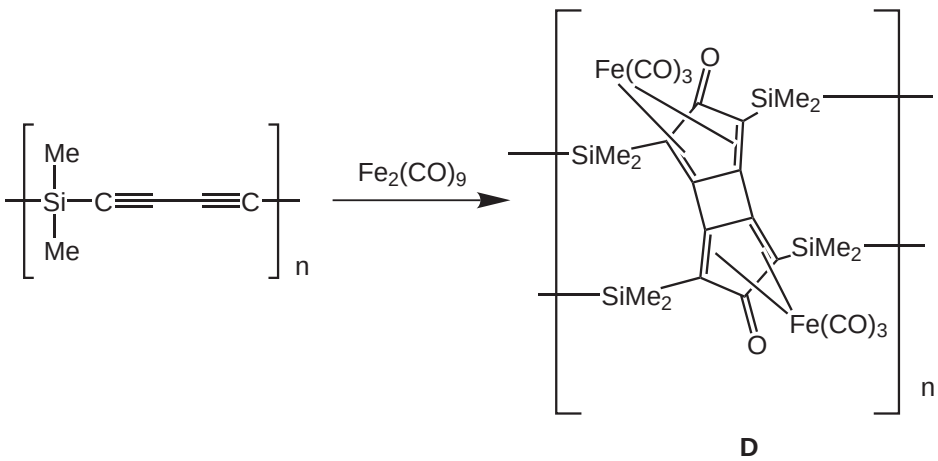

Figure 2.44: Proposed complexation reaction.

We have coordinated iron to the polymer, which is an excellent base for iron silicide nanocomposite formation. After subjecting compound **D** to the heat treatment of program **II**, the measured XRD pattern of the obtained material clearly showed a Fe_3Si (PDF 35-0519) phase besides a broad carbon reflexion at 25.9° (Figure 2.45). A maximum temperature of 1000°C was necessary to obtain iron silicides. Thermolysis at 850°C under H_2 led to iron-containing ceramics.

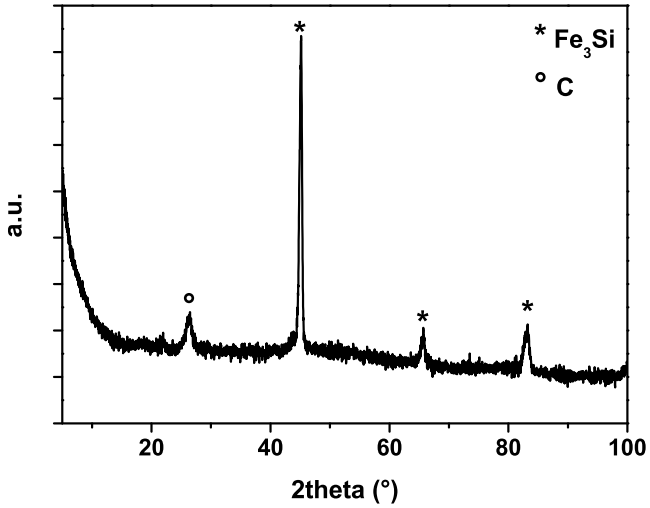

Figure 2.45: XRD pattern of Fe_3Si.

Concerning the iron silicide containing sample, particles were also observed by TEM measurements (Figure 2.46, left). In comparison to the iron silicide particles discussed above, they were more diluted in the matrix and also exhibited a large particle size distribution. EDX line scans across those particles displayed a high iron and silicon content. As expected, no metal content was observed in the matrix, leading to the conclusion of iron silicide particles surrounded by SiC/C (Figure 2.46, left).

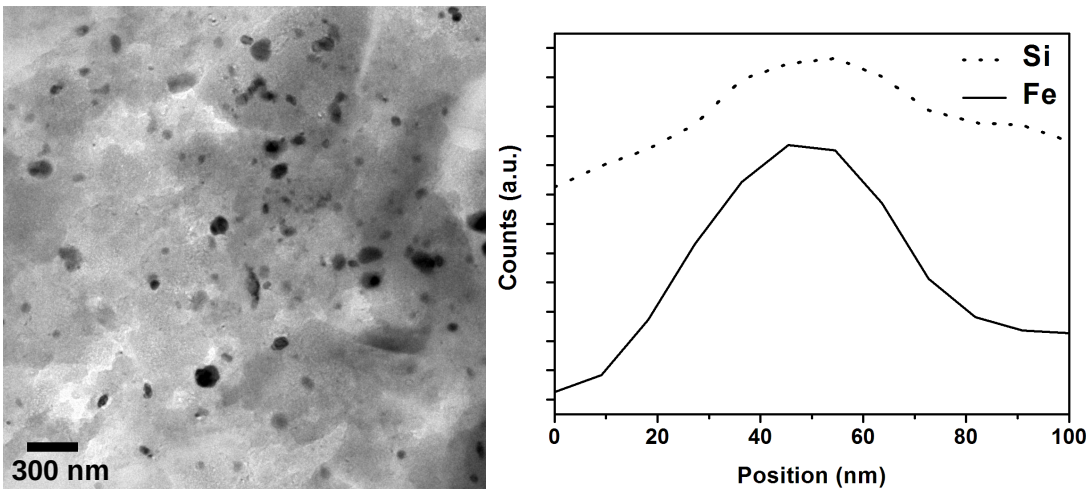

Figure 2.46: TEM pattern of Fe_3Si (left), EDX line scan profile of a single particle (right).

Obviously, this kind of precursor also led to Fe_3Si but resulted in a lower iron content (17.5 wt%). It seemed that the $Fe_2(CO)_9$ used as a starting material did not react with poly[(silylene)diacetylene] quantitatively, also evidenced by the deposition of orange $Fe_2(CO)_9$ at the cooler parts of the glass tube. Nevertheless, the resulting iron-containing polymer is an easily accessible precursor for iron silicide nanocomposite formation.

2.5.2 Cobalt and Manganese Silicides

Cobalt Silicide

Coordination of cobalt carbonyl to acetylene groups is well known in the literature and has been a topic of interest for several working groups.[81,83,172–175] For preparation of the cobalt precursor, the acetylene groups of poly[(silylene)diacetylene] reacted with $Co_2(CO)_8$ by dissociation of two carbonyl groups per dimeric unit (Figure 2.47), which led to polymer **E**.

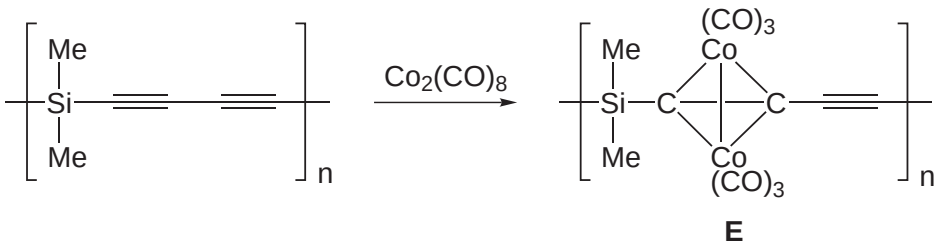

Figure 2.47: Reaction of poly[(dimethylsilylene)diacetylene with $Co_2(CO)_8$.

Work of Corriu *et al.*, who thermolysed polymer **E** under argon atmosphere at 1400°C, resulted in Co_2Si based ceramics.[84] In our work, a different temperature program (program **II**, *vide supra*) and nitrogen as an inert gas were used in conjunction with a maximum temperature of 1000°C. After thermolysis of compound **E**, the XRD pattern exhibited reflexions for Co_2Si (JCPDS PDF 04-0847) and the high temperature phase, face-centred cubic β-cobalt (JCPDS PDF 15-0806) with a ratio of 9:1 (Figure 2.48).

To gain insights into the nanostructure of the prepared materials, TEM measurements were performed. The obtained TEM patterns for the thermolysed cobalt carbonyl complexed polymer showed particles distributed in a matrix (Figure 2.49). It was obvious that the particle size distribution was broad (10–100 nm). The chemical composition

was additionally determined by EDX line scans across the particles and the matrix, which confirmed the existence of cobalt and silicon in the particles (Figure 2.49).

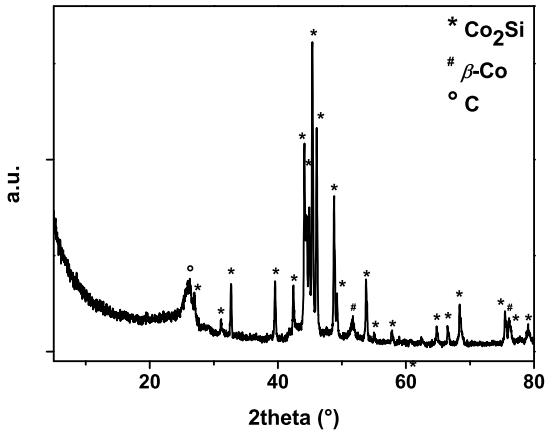

Figure 2.48: XRD pattern of Co_2Si/Co.

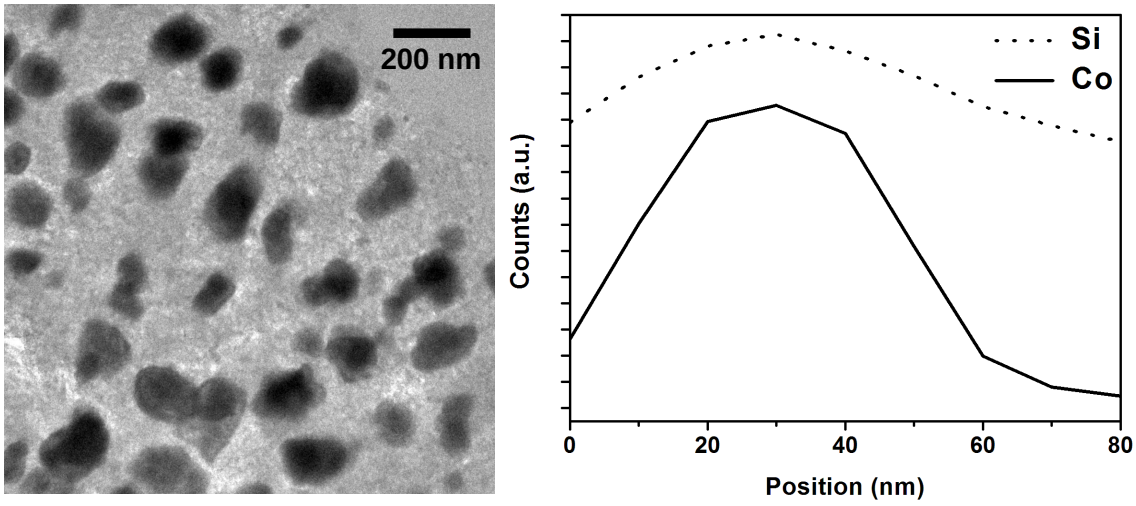

Figure 2.49: Left: TEM pattern of Co_2Si/Co; right: EDX scan profile of a single particle.

The formation of Co_2Si can be envisioned as involving the reaction of cobalt clusters with silicon released from the poly[(dimethylsilylene)diacetylene]. Thermolysis of organic materials under nitrogen not only led to the formation of carbon but also to evolution of volatile gases CH_4, H_2 and small amounts of C_2H_4.[82] That explains the weight loss of about ∼28 wt%, which took place during heat treatment. At lower temperatures (about 850°C) the formed cobalt clusters were not able to react with the Si

present in the matrix and it was only possible to generate β-cobalt instead of cobalt silicide.

Manganese Silicide

Coordination of transition metal carbonyl compounds to acetylene groups of a silicon-containing polymer is a convenient procedure to obtain suitable precursors for transition metal silicide nanocomposites. Its utility has been demonstrated for $Co_2(CO)_8$ and $Fe_2(CO)_9$ (*vide supra*). This strategy was applied to $Mn_2(CO)_{10}$. Unfortunately, neither long reaction times nor elevated temperatures led to a reaction between poly-[(dimethylsilylene)diacetylene] and $Mn_2(CO)_{10}$. Nevertheless, the mixture was used for further thermolysis experiments.

During heat treatment of the mixture with program **II**, leading to sample **FII**, small amounts of $Mn_2(CO)_{10}$ were deposited at the cooler end of the glass tube. Due to the volatile nature of the carbonyl compounds, we initially doubted whether this mixture might be suitable for metal silicide formation, in contrast to the chemically bonded metal carbonyls in compound **D** and **E**, where the metal source is an integral part of the polymer during heating. Nevertheless, enough manganese source remained in the mixture to form Mn_5Si_3 (JCPDS PDF 42-1285). The broad reflexions showed in the XRD pattern indicate the formation of smaller crystalline particles than in the samples before (Figure 2.50). A reflexion for graphite (JCPDS PDF 75-1621) was assigned in the XRD pattern at about 25.9°.

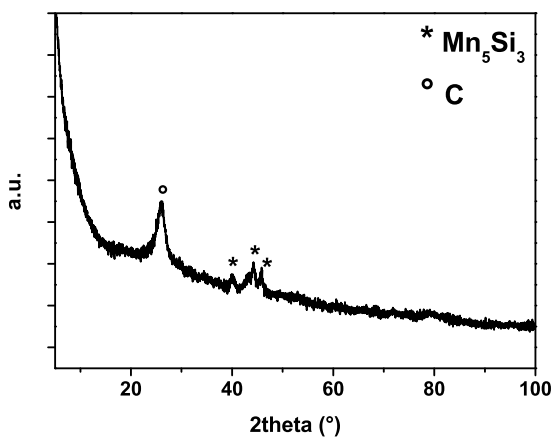

Figure 2.50: XRD pattern of Mn_5Si_3.

The nanostructured nature of the sample was also confirmed by TEM measurements and it was also possible to record meaningful EDX line scan profiles across single particles (Figure 2.51). The XRD pattern of Mn_5Si_3 in SiC/C sample showed broad reflexions, which indicated a small crystallite size. Reflexion (211) was employed for calculating the average crystallite size, which amounted to a mean size of 19 nm. The assumption of small particles was further confirmed by the recorded TEM images in Figure 2.51. Particles of about 10–30 nm were observed. For the non-reacted mixture, $Mn_2(CO)_{10}$ was partly evaporated during thermolysis. At higher temperatures CO dissociates, leading to a reaction of the now unsaturated manganese carbonyl fragments or even elementary manganese with the acetylenic groups of the polymer. Due to the thermal reaction, enough manganese can remain in the precursor mixture to form manganese silicide.

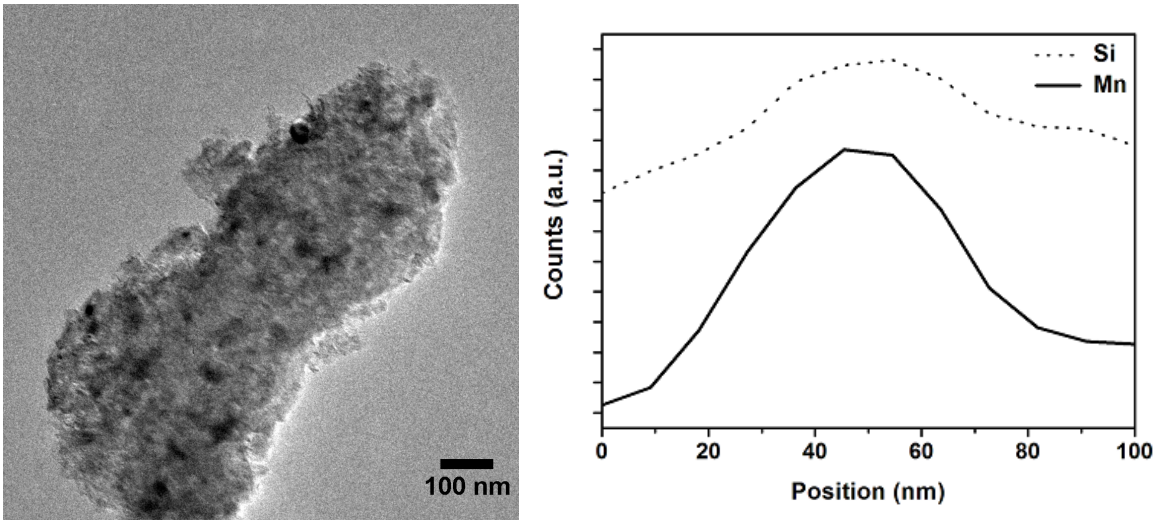

Figure 2.51: Left: TEM pattern of Mn_5Si_3; right: EDX line scan profile of a single particle.

The carbon part of the nanocomposites derived from the coordination compounds was also investigated by Raman spectroscopy. The spectra are all similar to the measurements shown in Figure 2.42. It can be concluded that the obtained graphite structures are the same as explained above.

2.5.3 Magnetisation of Iron and Cobalt Silicides

Iron Silicide

The magnetic behaviour of nanoparticles is strongly affected by inter-particle interactions, as well as shape and size effects.[4,8] When the size of magnetic particles is reduced to a few tens of nanometers, they become single domain particles, revealing dramatic changes in magnetic properties. For instance, small nanoparticles demonstrate a large coercivity, superparamagnetism, spin glass behaviour, *etc.*[8] Additionally, a small non-sphericity of single domain nanoparticles can result in a significant increase of the coercivity.[7,176]

The Fe_3Si particle size of the composites investigated here ranged from 10 to 100 nm and additionally agglomerates of about 0.6 μm were observed. Furthermore, the particles in sample **CII** and **CIII** were non-spherical (*vida supra*). Magnetic measurements were therefore performed to investigate the ferromagnetic properties of the Fe_3Si phase and their dependence on size and shape of the nanoparticles.

Table 2.11: The corresponding values of saturation magnetisation M_s, remanent magnetisation M_r, and coercive force H_c.

	M_s (emu/mol)	M_r (emu/mol)	H_c (Oe)
BI	6852	2360	120
CII	7428	1422	220
CIII	8207	242	65

Figure 2.52 shows the measured field dependence of the magnetisation of samples **BI**, **CII**, and **CIII** at room temperature. As can be seen, all samples exhibited a rather soft ferromagnetic behaviour with symmetric hysteresis loops. The coercive force H_c was at first observed to increase from ∼65 Oe (sample **CIII**) to ∼220 Oe (sample **CII**) with decreasing size of the nanoparticles (see inset of Figure 2.52). However, upon further reduction of size (sample **BI**) the coercive force decreased (∼120 Oe), presumably indicating the formation of single magnetic domain particles.[4] Moreover, the shape of the hysteresis loop of sample **BI** was more rectangular as expected for an array of single domain particles.[177]

In addition, samples **CII** and **CIII** revealed slower saturation than sample **BI**, which might be due to non-spherical shape of the nanoparticles in the former two samples that gives rise to an additional shape anisotropy. The saturation magnetisation M_s was

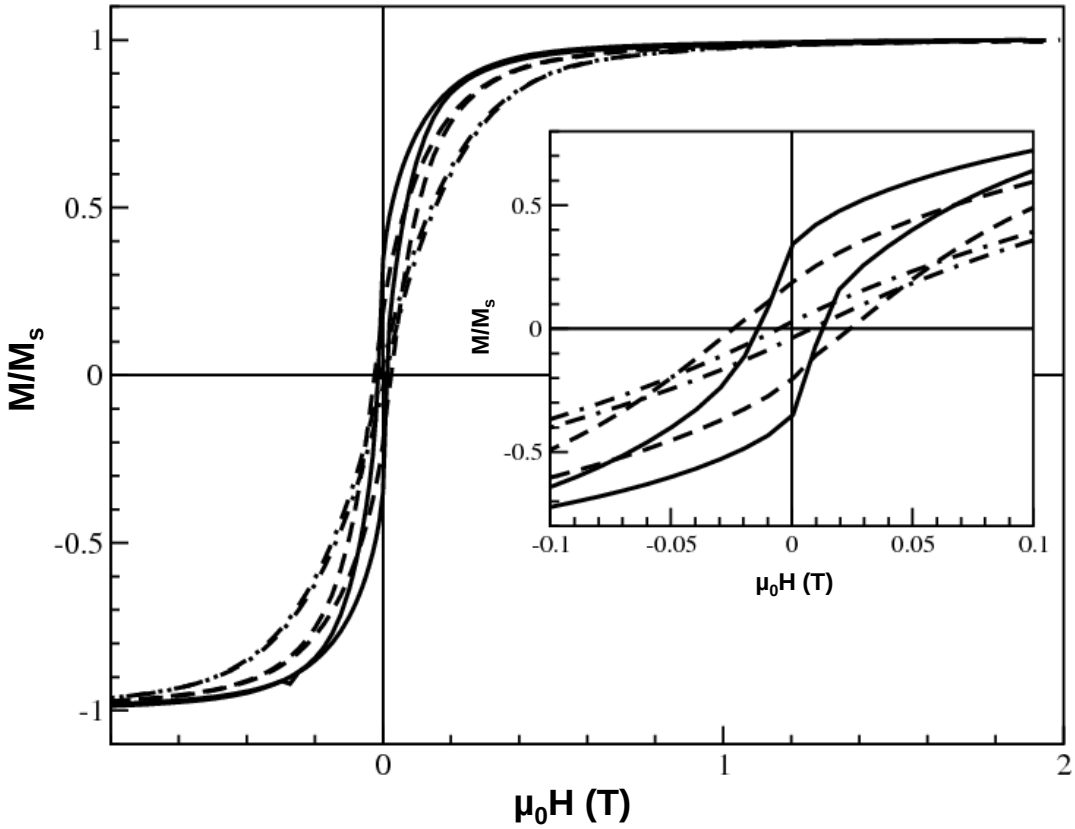

Figure 2.52: Reduced magnetisation M/M_s measured as a function of the applied magnetic field at room temperature in the samples **BI** (solid line), **CII** (dashed line), and **CIII** (dash-dotted line). Inset shows the low field region.

found to increase with the size of the nanoparticles (sample **BI** 6850 emu/mol, sample **CII** 7430 emu/mol, sample **CIII** 8210 emu/mol) whereas the remanent magnetisation M_r decreased from ∼2360 emu/mol in sample **BI** down to ∼242 emu/mol in sample **CIII** (see Table 2.11). Furthermore, the room temperature remanence ratio M_r/M_s also decreased with growing particle size, but remained much lower than M_r/M_s = 0.5 predicted by the Stoner-Wohlfarth model for randomly oriented non-interacting nanoparticles.[178] Such a low remanence ratio could indicate magnetostatic coupling of the well separated nanoparticles in the SiC/C matrix.[179]

It should be noted that measured M_s values were much lower than previously found (∼11700 emu/mol) in Fe_3Si nanoparticles.[78] This reduction of the saturation magnetisation may also be ascribed to the matrix effect.

Cobalt Silicide

The reduced magnetisation M/M_s has been plotted for the Fe_3Si samples (Figure 2.52) to show the anisotropy and the difference of the shape of M(H) curves. In the case of Co_2Si/Co nanocomposites, the M value is shown on the ordinate (Figure 2.53), because at low temperatures (3 K) no saturation of M and therefore no M_s value can be obtained.

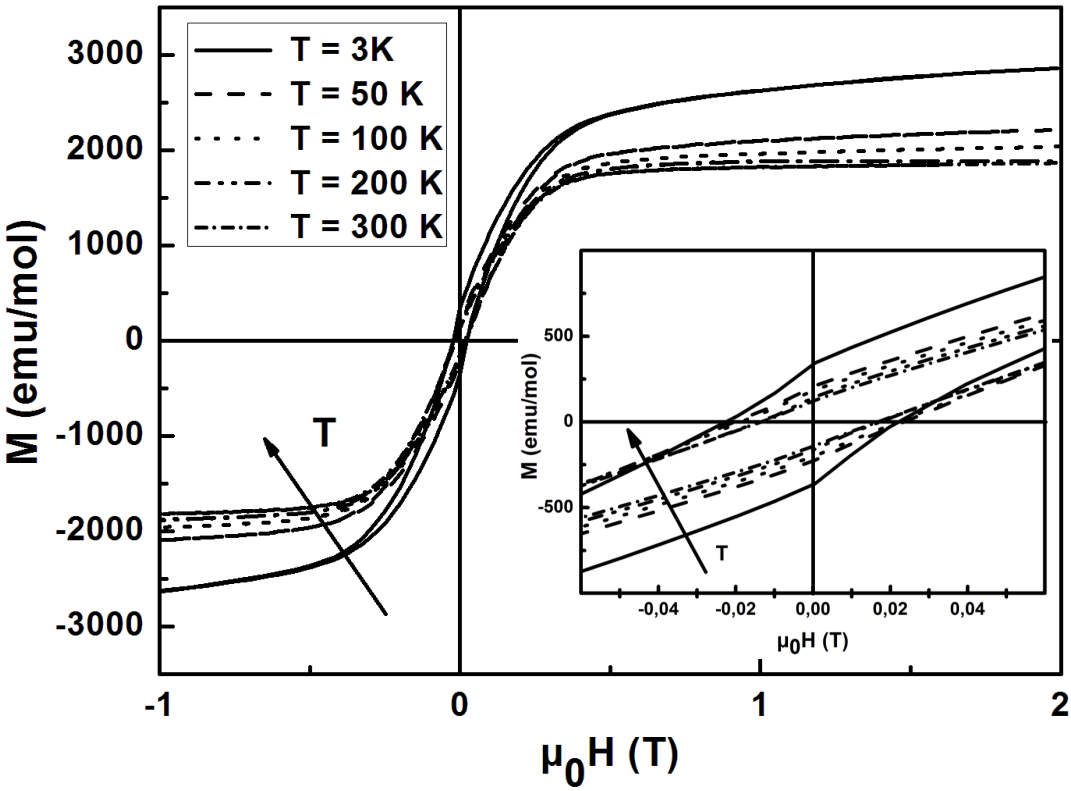

Figure 2.53: Field dependence of reduced magnetisation M measured at 3 K, 50 K, 100 K, 200 K and 300 K of Co_2Si/Co in SiC/C (**EII**). Inset shows the field region.

Additionally, the temperature dependence of the magnetic properties of the Co_2Si/Co nanoparticles dispersed in SiC/C was subject of our interest and was investigated by SQUID measurements. In Figure 2.53 the magnetisation as a function of magnetic field was measured in the temperature range T = 3–300 K. The hysteresis loop at 300 K and observed coercivity (196 Oe) indicated the presence of ferromagnetic nanoparticles.

Similar hysteresis loops as compared to room temperature measurements were observed at lower temperatures (decreasing to 3 K), with a gradual increase in the saturation

magnetisation. The magnetisation did not saturate at temperatures lower than 50 K, even when the applied field was increased to 10 kOe. A marginal change of the H_c values in the temperature range of 3–300 K is shown in Table 2.12.

Table 2.12: The corresponding H_c values of sample Co_2Si/Co in SiC/C (**EII**) at different temperatures.

T (K)	H_c (Oe)
3	195.3
50	195.2
100	195.5
200	195.3
300	195.7

Zero-field-cooled (ZFC) susceptibilities were measured by cooling the sample in zero field and then by increasing the temperature with an applied field (H = 1000 Oe), while field-cooled (FC) curves were recorded by cooling the sample in the measuring field. The ZFC and FC susceptibilities of the Co_2Si/Co sample are depicted in Figure 2.54. At high temperatures, the two curves coincide and the susceptibility follows in a first approximation a Curie-Weiss law.[7] At lower temperatures, they begin to separate and the ZFC magnetisation exhibited a narrow maximum, also called the blocking temperature (T_B = 4.6 K). This behaviour is characteristic of a superparamagnetic assembly of ferromagnetic particles[180] and it is due to the progressive deblocking of the particles of increasing size as the temperatures rises.

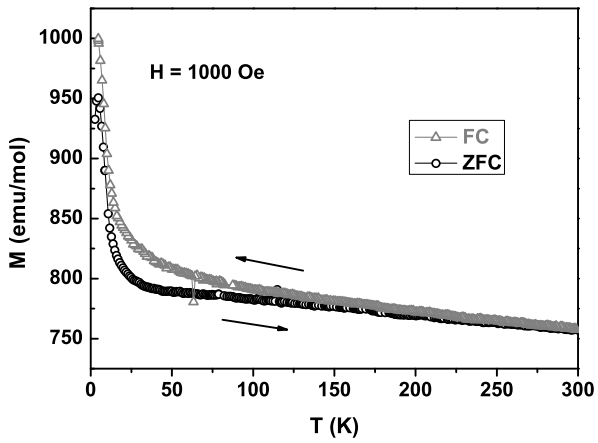

Figure 2.54: Temperature dependence of ZFC and FC susceptibilities of the Co_2Si/Co nanocomposite (**EII**).

The temperature at the maximum in the ZFC curve (T_B) is related, although in a complex way, to the blocking of particles with mean size, while the temperature at which the ZFC and FC curves begin to separate (T_{sep}) corresponds to the blocking of the largest particles. Complete convergence of FC and ZFC curves is not observed above the blocking temperature (T_B). Such behaviour is common with spin disorder systems (frustrated systems).[8] If spin disorder exists in the whole volume of a nanoparticle, reentrant spin-glass behaviour is expected.

It is known from the literature that diamagnetic compounds can be turned into ferromagnetic by size reduction. An appropriate case is the formation of CoSi nanowires on a Si substrate obtained by a vapour transport based method. Ferromagnetic properties of those nanowires in contrast to diamagnetic CoSi bulk were observed.[37]

Our Co_2Si/Co nanoparticles demonstrate ferromagnetic character and Co_2Si bulk is known to be paramagnetic at room temperature.[35] Due to the size reduction of Co_2Si nanoparticles, the contribution from their surface becomes larger, from which ferromagnetism can be expected. Defects or strain in the particles can also be responsible for that behaviour. It is difficult to assess whether the ferromagnetic behaviour stems from the reduced size of the Co_2Si nanoparticles or from the contribution of the Co nanoparticles (90% Co_2Si, 10% Co). Cobalt is known to be ferromagnetic in bulk (T_C = 1398 K).[181] It has also been shown in the literature that 4 nm large cobalt nanoparticles embedded in a paramagnetic matrix (C or Al_2O_3) still display ferromagnetism, due to the large effective additional anisotropy and a remarkable improvement in the thermal stability of the moments of the nanoparticles.[182]

In order to elucidate whether the cobalt proportion or reduced size effects are responsible for the observed ferromagnetism, systematic measurements and investigations are necessary.

2.6 Tetraethylsilane Treated Nanocomposites

Liang and co-workers[150] recently reported the synthesis of silicide modified nickel catalysts, which was achieved by simple SiH_4 treatment of nickel metal dispersed in carbon at elevated temperatures. Those catalysts showed improved activities towards phenylacetylene hydrogenation.

Those results encouraged us to verify the preparation procedure with different met-

als supported on γ-alumina. We were interested whether silane treatment of metal-containing materials always led to silicide formation. γ-Alumina was chosen as an appropriate supporting material, due to its widespread use in the catalytic community and facilitation of the analysis of possible silicon species after silane treatment. We used easily accessible $SiEt_4$, which is less hazardous than SiH_4.

The preparation of the alumina supported materials followed a straightforward impregnation route, which is a standard method to obtain metal-containing catalysts.[183] The impregnation route implied the preparation of metal salt solutions, which were subsequently used to impregnate γ-alumina. The used solvent was evaporated and the materials were calcined to obtain the corresponding metal oxides dispersed in the supporting material. Further reduction treatment under hydrogen at elevated temperatures led to the desired metal nanoparticles in γ-alumina.

The nanocomposites of Section 4.5.4 consist of five different metals: Co, Ni, Fe, Mn, and Mo, which are all dispersed in γ-alumina. The following reduction treatment required temperatures below 700°C to avoid agglomeration of the nanoparticles. It is known that MoO_3 requires temperatures of about 1200°C under a reducing atmosphere (H_2) to achieve the metallic state.[184]

Due to that behaviour, Mo precursors in low oxidation states were necessary, which were calcined under exclusion of air. It is indispensable to employ completely dissolved precursors for impregnation. A balance between solubility and loading of low oxidation state Mo precursors was necessary, which led to the choice of two different precursors: $Mo_2(OAc)_4$ on the one hand and $[MoCp(CO)_3]_2$ on the other hand.

Preparation (including drying) of the composites and filling the reactors for temperature-programmed reduction (TPR) were carried out in a glove-box in order to exclude air exposure. All materials were crushed and then sieved through a 30–80 mesh sieve, to avoid diffusion limitations during further treatments.

The following steps were performed in one unit, which consisted of six reactors in a heat block (maximum temperature 900°C) and it allowed to be the entire procedure under argon. The unit was equipped with a mass spectrometer (MS) in order to analyse the exhaust of one reactor (switching to different reactors was possible). The ethylene hydrogenation performance was a first test to monitor a possible change of the catalytic behaviour before and after tetraethylsilane treatment. Ethylene hydrogenation is a common model system to elucidate catalytic behaviour of suitable materials. Steps

performed:

- temperature programmed reduction.
- first ethylene hydrogenation.
- tetraethylsilane treatment.
- second ethylene hydrogenation.

The catalysts are named **Co**, **Ni**, **Fe**, **Mn**, **Mo1** and **Mo2** after reduction and **Co/SiEt$_4$**, **Ni/SiEt$_4$**, **Fe/SiEt$_4$**, **Mn/SiEt$_4$**, **Mo1/SiEt$_4$** and **Mo2/SiEt$_4$** after $SiEt_4$ treatment.

The ethylene hydrogenation results are discussed in Section 2.7. The application of tetraethylsilane at elevated temperatures was tested as a procedure for silicide formation. The reaction was monitored by mass spectrometry, with focus on the molybdenum-containing catalyst derived from **Mo1**. Total consumption of $SiEt_4$ accompanied by ethane production was observed. After about 2 h the detected $SiEt_4$ amount increased, while the amount of detected ethane decreased. After 3 h the end of the reaction was indicated by no further consumption of $SiEt_4$.

The two most promising catalysts (**Ni/SiEt$_4$** and **Mo1/SiEt$_4$**) were investigated in detail by TEM, EDX and XPS measurements.

TEM of both samples were recorded and are depicted in Figure 2.55. A rod-like structure was observed, this formation stemmed from the heat treatment of γ-Al_2O_3 at 600°C. In metal-free γ-Al_2O_3 samples, the observed rods were also present (Figure 2.56). Attempts to record diffraction patterns of the metal-containing materials only revealed reflexions of the carrier material (γ-Al_2O_3).

Identification of any significant metal-containing particles after $SiEt_4$ treatment in the samples by TEM was not successful. Nevertheless, EDX analyses of different spots of the samples were performed with the intention to assign a suitable composition for possibly formed metal silicides (see Table 2.13 and Table 2.14).

Even when regarding the stoichiometry of $MoSi_2$ with the highest silicon proportion of all molybdenum silicides (Mo:Si weight ratio is 2.5:1), the silicon content detected by EDX on several spots in one sample was too high. A similar phenomenon was observed for the **Ni/SiEt$_4$** sample: the calculated weight ratio of Ni:Si for $NiSi_2$ (which exhibits the highest silicon proportion of all nickel silicides) was 1.04:1, *i.e.* the silicon content

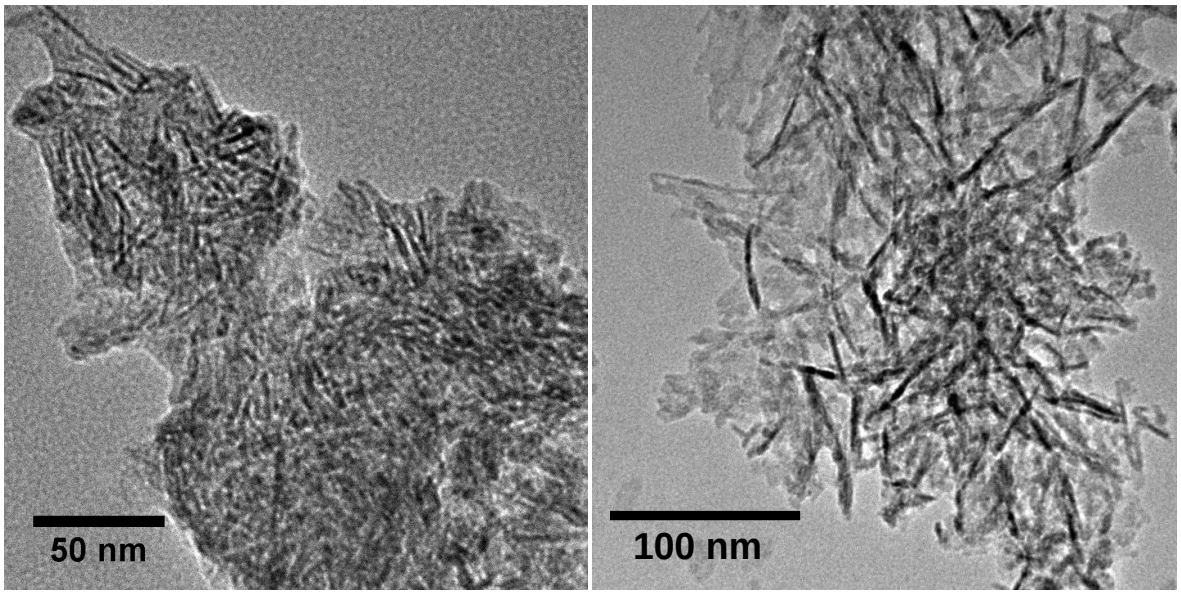

Figure 2.55: TEM pattern of **Mo1/SiEt$_4$** (left) and **Ni/SiEt$_4$** (right).

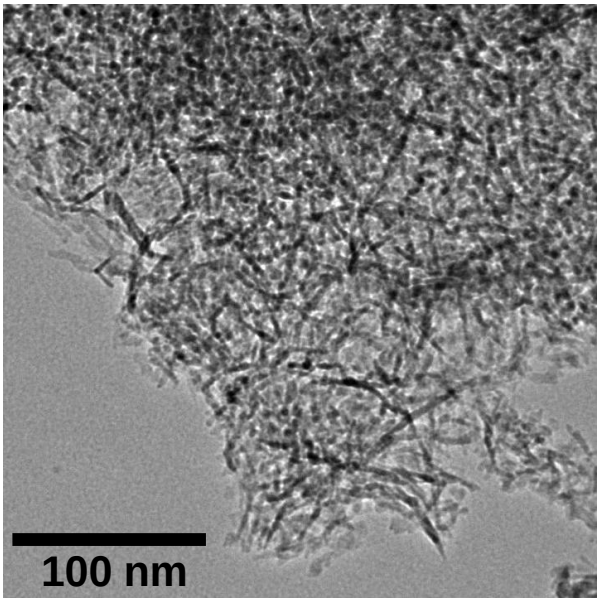

Figure 2.56: TEM pattern of pure γ-Al_2O_3 treated at 600°C.

measured by EDX also showed a too high silicon amount.

If the formation of metal silicides took place, the excess of detected silicon must stem from another silicon species such as SiO_2, SiC, silicate or even elemental silicon. The detection of the highly dispersed metal and silicon reached the limit of the TEM method. XPS analyses of both samples were carried out to distinguish the oxidation states of the species present in the material.

Table 2.13: Mo and Si content in sample **Mo/SiEt$_4$**.

Mo (wt%)	Si (wt%)
2.8	5.4
1.4	5.4
1.1	5.5
1.8	4.6
2.2	3.7
1.8	3.5
1.0	4.2

Table 2.14: Ni and Si content in sample **Ni/SiEt$_4$**.

Ni (wt%)	Si (wt%)
5.1	9.9
3.9	10.0
6.8	11.0
3.7	9.4
5.2	11.9
6.0	11.5
6.1	10.9

The survey spectra of **Mo/SiEt$_4$** and **Ni/SiEt$_4$** are shown in Figure 2.57 and 2.58. All species of interest are depicted (Mo, Ni, C, Si, Al, O) in the spectra. Additionally, the determined atomic composition of the samples is reported in Table 2.15.

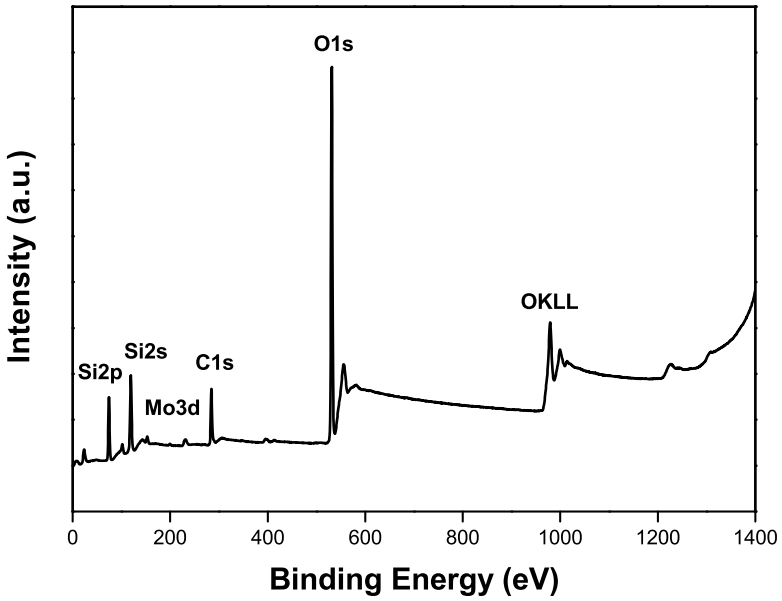

Figure 2.57: XPS survey spectrum of sample **Mo/SiEt$_4$**.

The exhibited atomic compositions showed a much lower Mo3d rate compared to Ni2p: this is ascribed to the lower initial amount of precursor $Mo(OAc)_4$, whereas the content of nickel in the compound has to be at least 10 wt%.

Regarding the molybdenum species, the relevant BE values are shown in Table 2.16

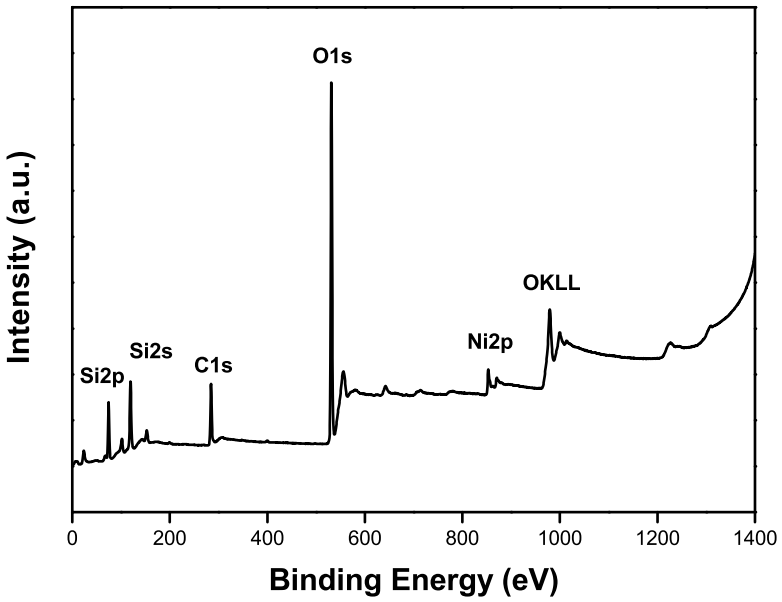

Figure 2.58: XPS survey spectra of sample **Ni/SiEt$_4$**.

Table 2.15: Atomic percentages delivered by XPS analysis.

Mo/SiEt$_4$	**atomic %**	**Ni/SiEt$_4$**	**atomic %**
O1s	53.4	O1s	49.7
C1s	15.0	C1s	19.0
Al2p	29.0	Al2p	24.8
Si2p	2.3	Si2p	4.8
Mo3d	0.4	Ni2p	1.8
Si/Mo	4.1	Si/Ni	1.2

and the Mo3d and Si2p components are depicted in the deconvolution spectra in Figure 2.59.

The BE value of the main peak in the deconvolution spectrum of Mo3d$_{3/2}$ at 232.5 eV was assigned to Mo(IV) species. The reported values of Mo3d$_{3/2}$ for MoO_2 were between 232.3 and 235.7 eV.[185,186] The second peak of Mo3d$_{5/2}$ at 229.4 eV could also be ascribed to Mo(IV) species, the corresponding values of Mo3d$_{5/2}$ were given in the literature in the range of 228.8 to 229.4 eV.[185–187] The spectrum exhibited a small shoulder for Mo3d$_{3/2}$ at 235.7 eV, which can be attributed to a Mo(VI) species, as reported in the literature.[185]

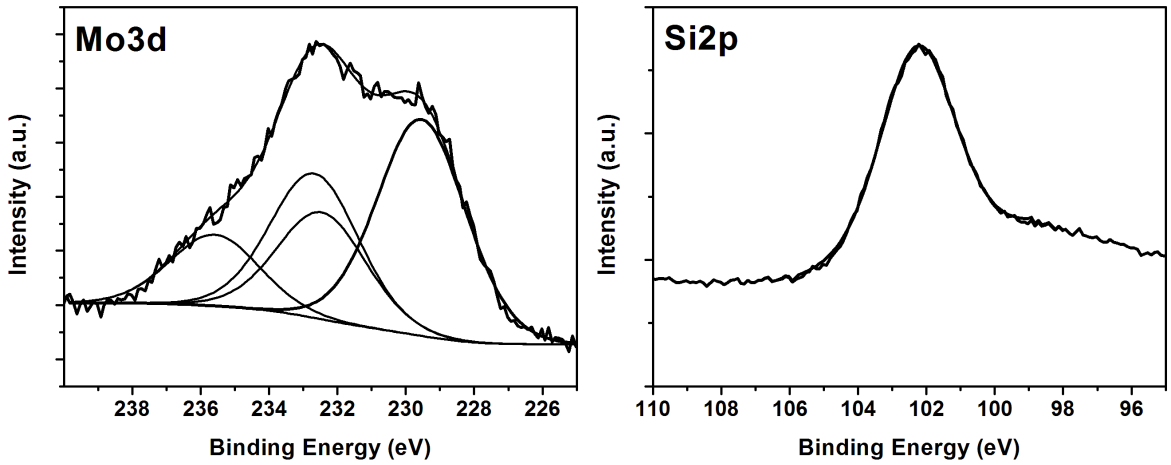

Figure 2.59: Deconvolution of the Mo3d (left) and Si2p (right) region of the sample **Mo/SiEt$_4$**.

Table 2.16: Binding energies of the relevant species for sample **Mo/SiEt$_4$** (values corrected for charging effects).

Region	BE (eV)
O1s	531.6
Si2p	102.3
Si2s	119.5
Mo3d$_{5/2}$	229.5
Mo3d$_{3/2}$	232.5
	235.7

No significant peaks supporting the existence of $MoSi_2$ could be observed in Figure 2.59, left. The known peaks of Mo3d$_{3/2}$ for $MoSi_2$ range between 227.4 and 227.6 eV[188,189] and the value of Mo3d$_{5/2}$ for $MoSi_2$ was reported to be 230.9 eV.[188]

A closer look at the Si2p spectrum of sample **Mo/SiEt$_4$** indicated a single peak at 102.3 eV corresponding to molybdenum in a silicate environment,[190] whereas no Si2p peak for $MoSi_2$ could be attributed, which should appear around 99.1–99.4 eV (Figure 2.59, right).[188,189]

These results supported the absence of $MoSi_2$ and the presence of MoO_2 and MoO_3. Additionally, the BE value for O1s (531.6 eV) was slightly higher than expected for MoO_x species, which was known to range from 529.6 to 531.1 eV.[185–187,189,191] This findings could be ascribed to the prevalence of silica or silicate with respect to molybdenum-based species.[152] Nevertheless, formation of $MoSi_2$ could not be excluded, due the very high oxidation sensitivity of $MoSi_2$ which was analysed in detail by Shaw and

co-workers.[192]

Table 2.17: Binding energies of the relevant species for sample **Ni/SiEt$_4$** (values corrected for charging effects).

Region	BE (eV)
O1s	531.6
Si2p	100.1
	102.3
Si2s	120.1
Ni2p$_{3/2}$	853.3
	856.3
	863.1
Ni2p$_{1/2}$	870.9
	873.9
	880.1

From the detailed spectrum of the most important regions of sample **Ni/SiEt$_4$** (O1s, C1s, Al2p, Si2p, Ni2p) the atomic composition was determined as reported in Table 2.15. Concerning the chemical state of the different species, the detected BEs (corrected for charging effects) are depicted in Table 2.17.

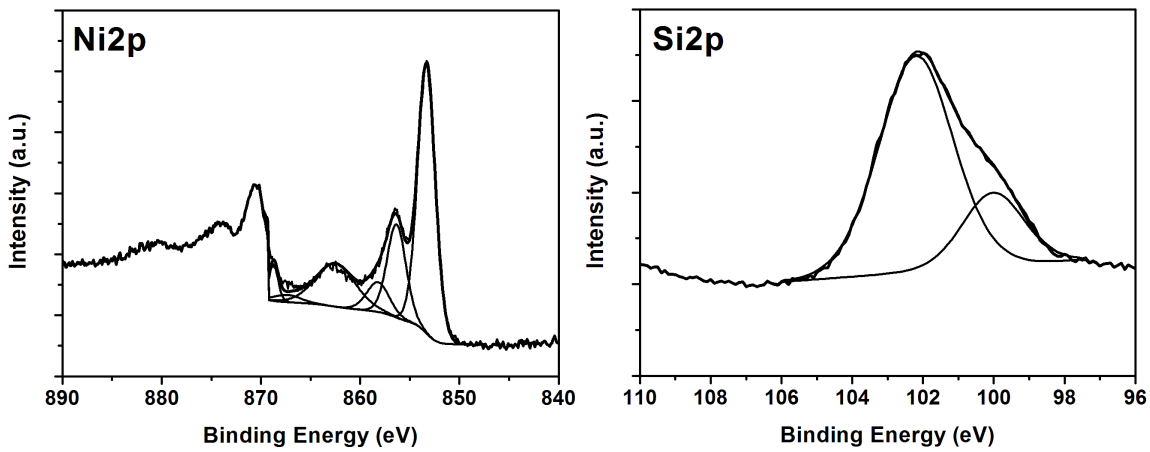

Figure 2.60: Deconvolution of the Ni2p (left) and Si2p (right) region of the sample **Ni/SiEt$_4$**.

The deconvolution spectrum of the Ni2p region presented two peaks for the nickel oxide species (Figure 2.60). The peaks obtained at binding energies of 856.3 eV (Ni2p$_{3/2}$) and 873.9 eV (Ni2p$_{1/2}$) suggested the presence of NiO (854.0–856.8 eV for (Ni2p$_{3/2}$) and 873.0–880.0 for (Ni2p$_{1/2}$)). Satellite peaks due to shake-up processes appeared between 861–862 eV and 879–881 eV.[152,193,194]

Two additional peaks were observed at 853.3 eV ($Ni2p_{3/2}$) and 870.9 eV ($Ni2p_{1/2}$) in Figure 2.60, which were much lower than suggested for nickel oxide. The obtained binding energies could be attributed to nickel silicide. Since the recorded values for the Ni2p region for different nickel silicides (Ni_3Si, $Ni_{31}Si_{12}$, Ni_2Si, NiSi and $NiSi_2$) were very similar, we assume the composition of $NiSi_2$ fits best, given the results of the measurement.[152,195] Not only the Ni2p binding energies, but also the found binding energy in the region of Si2p at 100.1 eV (Figure 2.60) supported the formation of $NiSi_2$.[195,196] An additional peak at 102.3 eV indicated the presence of nickel silicate, which was supported by a binding energy of 531.6 eV in the O1s region. This could be ascribed to the prevalence of silica or silicate with respect to nickel-based species.[152]

Strong evidence was given by XPS measurements that a mixture of different nickel phases was present after tetraethylsilane treatment of the nickel supported γ-alumina. Apart from nickel oxide and nickel silicate, the presence of nickel silicide was confirmed.

2.7 Ethylene Hydrogenation

Hydrogenation of ethylene (see Figure 2.61) catalysed by metals has been an intensively investigated topic for several years.[197–199] For instance, the catalytic conversion of ethylene to ethane on nickel has been discussed in great detail.[200,201] Ethylene hydrogenation is a suitable test model to distinguish catalytically active materials from catalytically inactive materials.

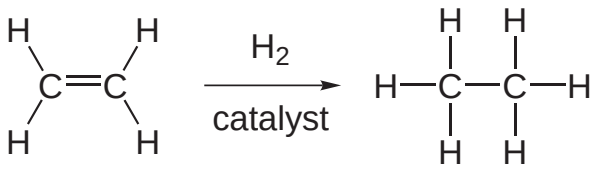

Figure 2.61: Ethylene hydrogenation using a catalyst.

The first ethylene hydrogenation test was performed after TPR experiments and the second test after $SiEt_4$ treatment. We used ethylene hydrogenation as a test to identify catalytic activity of the materials before and after $SiEt_4$ treatment. In Figure 2.62, the observed ethylene to ethane conversion is depicted. Catalyst **Co** and **Ni** exhibited 100% conversion to ethane, while the other catalysts showed nearly no conversion. This is not entirely surprising, especially since nickel-containing catalysts are used to perform ethylene hydrogenation.[200,201]

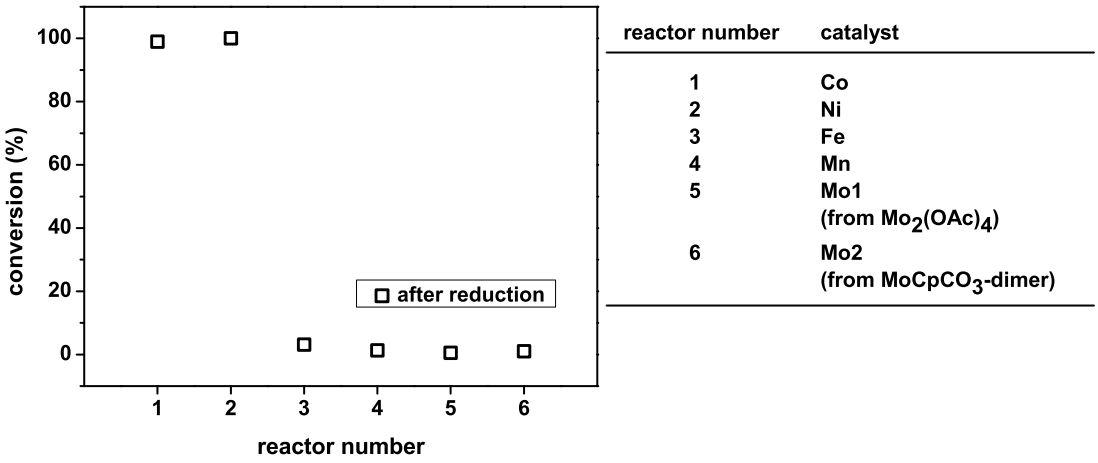

Figure 2.62: Ethylene hydrogenation after reduction.

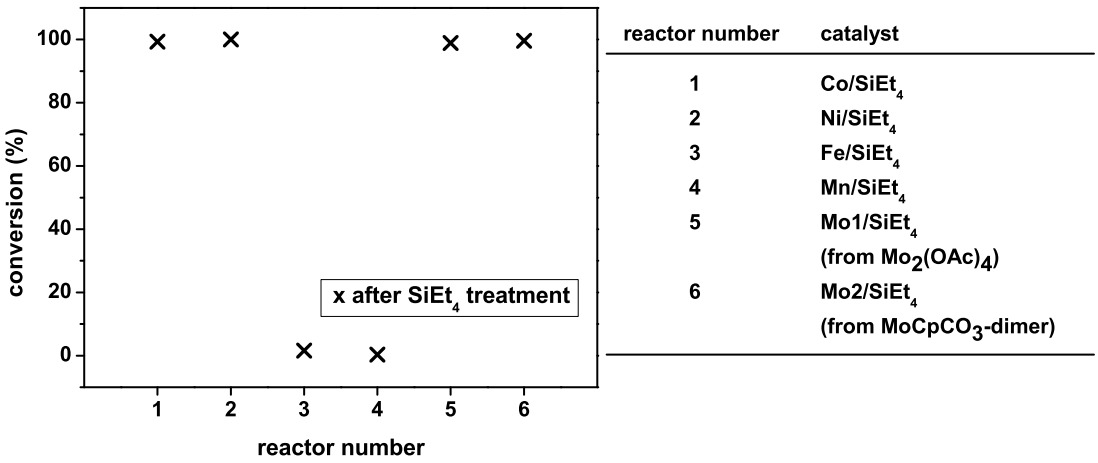

Figure 2.63: Ethylene hydrogenation after reduction and $SiEt_4$ treatment.

The second hydrogenation test at 40°C was carried out after $SiEt_4/H_2$ treatment of all catalysts at 400°C for 5 1/2 h. In Figure 2.63, the observed conversion of ethane is shown. It is obvious that the previously inactive **Mo1** and **Mo2** are active towards ethylene hydrogenation after $SiEt_4$ treatment, with 100% conversion to ethane taking place. The **Fe** and **Mn** catalyst did not show any change in the conversion rate, *i.e.* their behaviour towards ethylene hydrogenation before and after tetraethylsilane treatment is the same. For reactor number 1 and 2, no deterioration of performance occurred. Of course, no improvement can be interpreted from the data, given that

100% conversion already took place before $SiEt_4$ treatment. It turned out that the molybdenum-containing materials underwent the most interesting change in catalytic activity. Additionally, elemental molybdenum was not suitable as a catalyst for ethylene hydrogenation.

Although XPS spectra (Section 2.6) only showed formation of molybdenum oxide and silicate, molybdenum silicide formation could not be ruled out, given its oxidation sensitivity, which might have taken place during sample transfer to the XPS instrument. Based on the available experimental evidence (TEM, EDX and XPS), it is impossible to tell which phase was responsible for the observed catalytic activity.

2.8 Hydrodesulphurisation

Hydrodesulphurisation (HDS) is the reaction through which sulphur is removed from petroleum feedstock in refineries by reaction with hydrogen over solid catalysts under rather severe temperature and pressure conditions. Under these reaction conditions, sulphur-containing organic molecules present in the feed decompose to hydrocarbons and H_2S. We applied the materials synthesised in Section 2.4 and Section 2.5 for the following DBT HDS degradation tests. The dibenzothiophene conversion reaction paths are depicted in Figure 2.64.

There are two reaction pathways for HDS of DBT: either prehydrogenation of one of the arene rings followed by sulphur removal (HYD) of the heterocyclic moiety; or, alternatively, direct sulphur extrusion without any need for previous hydrogenation (DDS). In the direct desulphurisation reaction, which is the main route, dibenzothiophene and H_2 react to form biphenyl and H_2S. The hydrogenation reaction involves the hydrogenation of one benzene ring of dibenzothiophene, followed by desulphurisation of the resulting hexahydrodibenzothiophene to yield cyclohexylbenzene. More detailed accounts of the mechanisms are available in several recent reviews.[117–119]

2.8.1 Hydrodesulphurisation by Cobalt Nanocomposites

The first batch, which was tested by DBT HDS and subsequently analysed by GPC with regards to the conversion products, consisted of the cobalt nanomaterials from Section 2.4. All materials were investigated, with exception of the cobalt nanoparticles

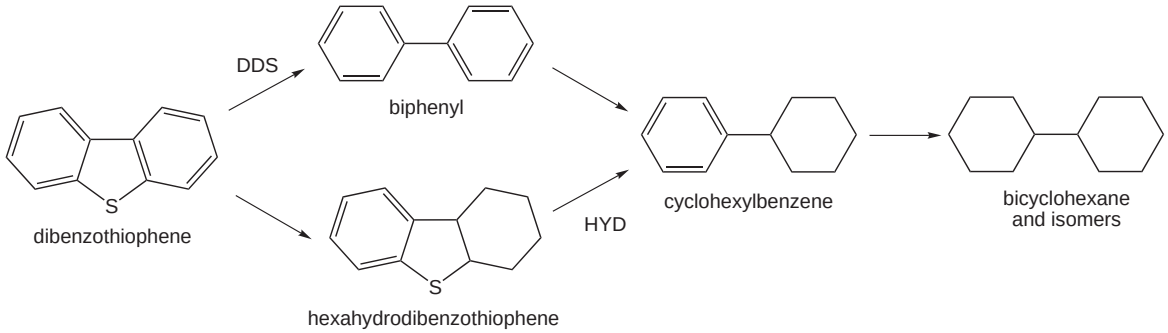

Figure 2.64: Dibenzothiophene degradation route.

on graphite due to their very low surface area of 10 m^2/g.

In Figure 2.65 dibenzothiophene hydrodesulphurisation results for cobalt-containing catalysts (Co_2SiO_4 and CoO in silica) prepared with impregnation methods and the material obtained by sol-gel route are plotted. The k-value was calculated for the DBT conversion measurements assuming pseudo 1st order kinetics.

The synthesis route for cobalt nanoparticles by impregnation of silica with $Co(CO)_4$ $SiCl_3$ presented in Section 2.4, resulted in cobalt nanoparticles with a Co_2SiO_4/CoO shell after treatment at 300°C under H_2. Furthermore, the cobalt nanoparticles formed after impregnation on charcoal were tested in the following batch. In order to compare these different nanocomposites, a sol-gel derived cobalt-containing silica material was produced by a procedure from the literature.[161,162] All the catalysts were pretreated with a presulphiding feed (hexadecane and 5.4 wt% of ditertiononylpentasulphide).

It is obvious from Figure 2.65, that the sol-gel sample exhibited the highest activity towards DBT conversion, which was not unexpected for the following reasons: the material offered a high surface area (about 399 cm^2/g, see Figure 2.30) and the catalytically active phase (Co_2SiO_4 or CoO units) was well dispersed in the silica, which presented excellent properties for catalytic degradation of dibenzothiophene. The higher conversion rate might also stem from the consumption of sulphur by formation of a phase resembling cobalt sulfides.[118]

The nanocomposite formed by impregnation of $Co(CO)_4SiCl_3$ on silica and subsequent reduction treatment showed much lower activity towards DBT HDS. The particles are quite large (20 nm). Considering the ln k-values of the nanomaterial cobalt on charcoal, the catalytic activity was not significantly lower when compared to the cobalt nanoparticles formed in silica. It appears that the supporting material had no signifi-

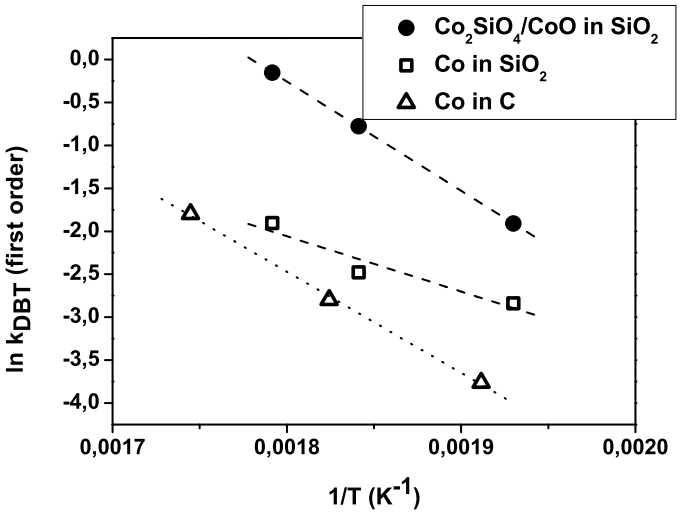

Figure 2.65: Arrhenius plot of DBT conversion at elevated temperatures; H_2-feed 250 mL/g.

cant impact on the catalytic activity.

Figure 2.66 shows the conversion products of Co_2SiO_4/CoO in silica and Co in silica (at 245°C, 270°C and 285°C, respectively). The data of cobalt in charcoal measurements were not considered, because the conversion reactions were carried out at different temperatures (250°C, 275°C and 300°C).

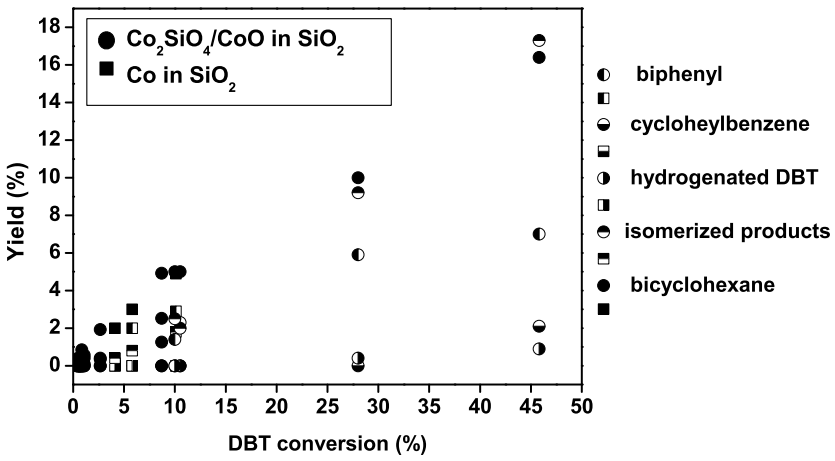

Figure 2.66: Selectivity of DBT conversion at 245°C, 270°C, 285°C; H_2-feed 250 mL/g.

The highest conversion of 45.8% was achieved for the sol-gel material at 285°C and the

main product was cyclohexylbenzene, while at lower temperatures biphenyl was the predominant product. These results led us to conclude that the direct desulphurisation reaction (DDS) route (see Figure 2.64) was favoured, followed by a hydrogenation of one phenyl group at higher temperatures. The cobalt in silica sample behaved similar, but with a much lower conversion of 10.1%.

The product fractions after DBT HDS using the cobalt in charcoal catalyst are shown in Table 2.18. It exhibited the highest conversion rate at 300°C of 11.2%. Biphenyl was again the main product at all temperatures, which supported the DDS route for degradation of DBT. In terms of selectivity, the catalysts (cobalt in silica or in charcoal) behaved similarly, consequentially no dependence on the supporting material could be demonstrated by the HDS tests.

Table 2.18: Conversion yields after DBT HDS over cobalt in charcoal.

Temperature (°C)	250	275	300
DBT conversion (%)	**1.6**	**4.3**	**11.2**
biphenyl (%)	0.6	1.9	5.4
cyclohexylbenzene (%)	0.0	0.2	1.8
hydrogenated DBT (%)	0.0	0.6	3.4
isomerized roducts (%)	0.0	0.0	0.0
bicyclohexane (%)	0.0	0.0	0.0

2.8.2 Hydrodesulphurisation by Transition Metal Silicide Nanocomposites

Further experiments were performed with the synthesised transition metal silicide nanocomposites of Section 2.5. We were again interested in their activity towards dibenzothiophene conversion to sulphur free organic compounds and also their selectivity during the degradation process.

The silicides chosen for the test were Co_2Si/Co (**EII**, particle size = 50–150 nm), Fe_5Si_3 (**BII**, particle size = 10–100 nm) and Mn_5Si_3 (particle size = ∼20 nm). It is worth mentioning that the materials were pretreated with hydrogen before the normal HDS test and no presulphiding feed was applied. The most active catalyst in this series was the cobalt containing one: since two phases were present, *i.e.* Co_2Si (90%) and Co (10%), we were not able to identify the catalytically active phase (see Figure 2.67). Compared to the pure cobalt phase of cobalt in charcoal materials, the perfor-

mance was still 0.5 units lower and for the sol-gel material even 2 units lower. This supports the assumption that Co_2Si phase was less active than cobalt or cobalt oxide catalysts. Considering the other two silicides, both HDS performances observed were lower compared to the cobalt nanocomposites (see Section 2.8.1).

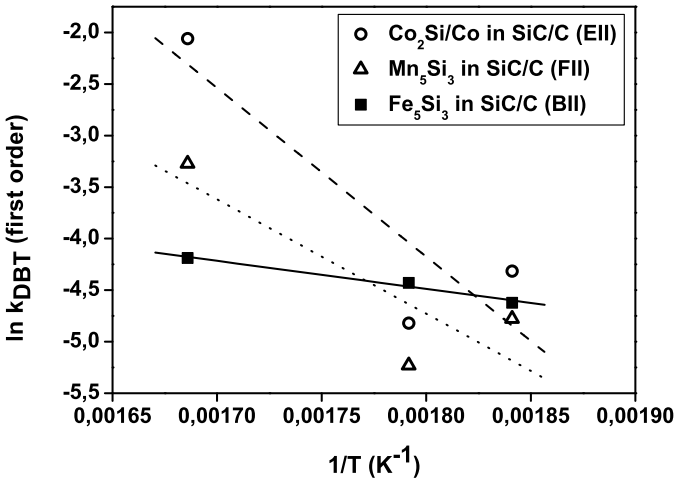

Figure 2.67: Arrhenius plot of DBT conversion at 270°C, 285°C and 320°C; H_2-feed 250 mL/g.

The plot in Figure 2.68 exhibits the selectivity of the employed materials. The manganese and cobalt-containing catalysts behaved similarly. The main product was biphenyl followed by hydrogenated DBT: it seems that both routes (DDS and HYD) were active, with a preference for DDS. Considering the iron containing compound, the production of hydrogenated DBT was promoted and less biphenyl (0.1%) at 320°C could be found. The Fe_5Si_3 in SiC/C catalyst facilitated the hydrogenation reaction, which involved the hydrogenation of one benzene ring of dibenzothiophene (HYD).

It is interesting to study the influence of the pretreatment on the catalytic behaviour. For pretreatment of the cobalt nanocomposites, a presulphiding feed was used while for the silicide nanocomposites, a hydrogen flow was used to that end. The following test set included Fe_3Si in SiC/C from different organometallic polymers. One sample consisted of particles with sizes between 10–30 nm (**BI**) and the other of about 10–100 nm (**CII**). The catalysts were tested at 250°C, 275°C, 300°C, 325°C and 350°C (Figure 2.69).

The materials which were pretreated using the presulphiding feed exhibited a higher

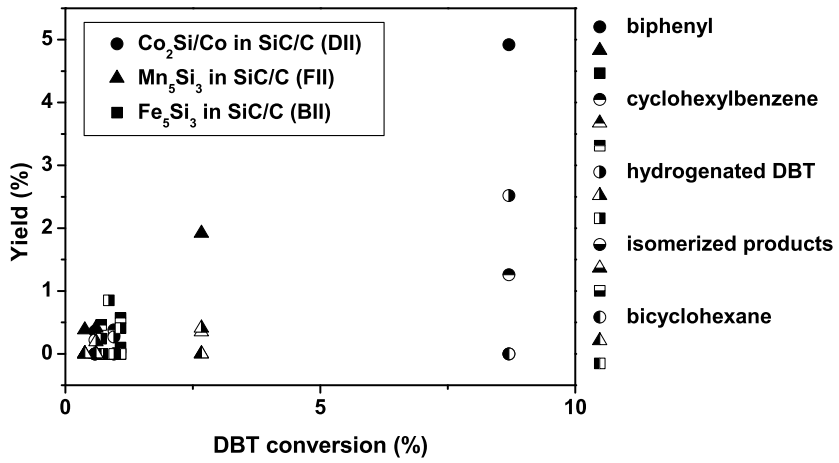

Figure 2.68: Selectivity of DBT conversion at 270°C, 285°C, 320°C; H_2-feed 250 mL/g.

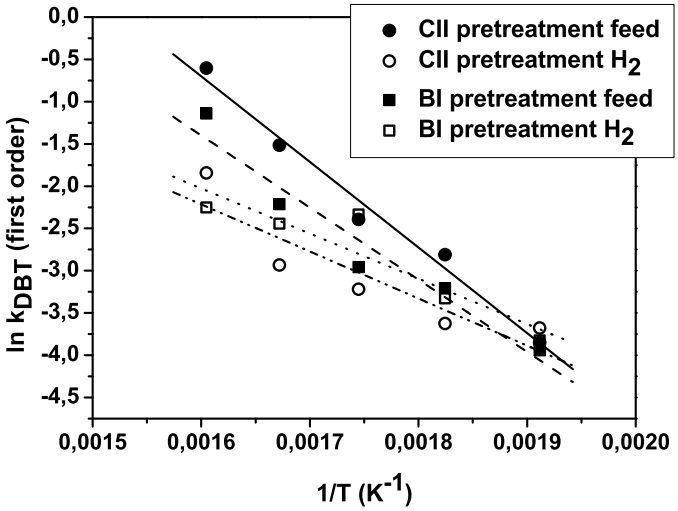

Figure 2.69: Arrhenius plot of DBT conversion at 250°C, 275°C, 300°C, 325°C and 350°C; H_2-feed 250 mL/g.

activity than the hydrogen pretreated materials. It seems that the feed flow activated the surface of the particles more than hydrogen. It is intriguing to note that the sample containing the larger particles (10–100 nm) resulted in a better conversion of dibenzothiophene than Fe_3Si, which contained particles sized around 10–30 nm.

The selectivity plots of both catalysts depicted in Figure 2.70 display similar conversion

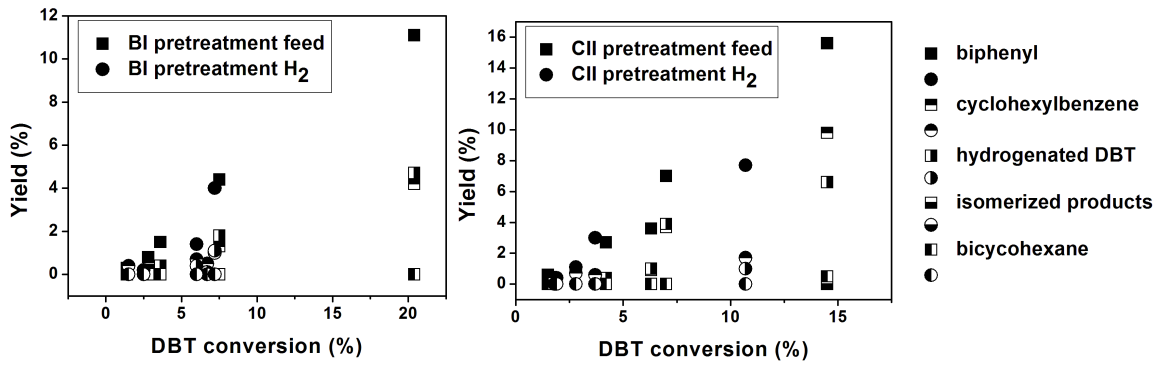

Figure 2.70: Selectivity of DBT conversion at 250°C, 275°C, 300°C, 325°C and 350°C; H_2-feed 250 mL/g.

rates for sample **BI** and **CII**. Biphenyl was the main product at 350°C in both cases, followed by cyclohexylbenzene and hydrogenated DBT. The direct sulphur extrusion (DDS) seemed to be the favoured route followed by hydrogenation of one phenyl group to cyclohexylbenzene. The conversion yield of the hydrogen pretreated material was lower but exhibited similar selectivity plots. Therefore, the hydrogen pretreatment had an influence on the conversion yield but not on the observed selectivity.

2.8.3 Hydrodesulphurisation by Nanocomposites before and after Tetraethylsilane Treatment

Since the materials showed a higher activity towards ethylene hydrogenation after $SiEt_4$ treatment (see Section 2.7), we were interested in their behaviour towards the commercially more relevant dibenzothiophene conversion at elevated temperatures (300°C, 325°C and 350°C). We did not consider the results of **Mo2** and **Mo2/SiEt$_4$** catalysts, due to a technical issue during the dibenzothiophene degradation measurements.

The Arrhenius plots of the catalysts before $SiEt_4$ treatment are depicted in Figure 2.71: **Co**, **Ni** and **Mo1** ln k-values of those nanocomposites are in the same range as compared to the observed ln k-values of **Fe** and **Mn**, which are much lower. It has to be mentioned that all compounds consisted of 10 wt% metal, with exception of the molybdenum-containing material, which has a loading of 1.6 wt% molybdenum (**Mo1**). Nevertheless, the catalyst **Mo1** exhibited an activity as high as the cobalt-containing compound.

The graph shown in Figure 2.72 exhibits the ln k-values of the catalysts after $SiEt_4$

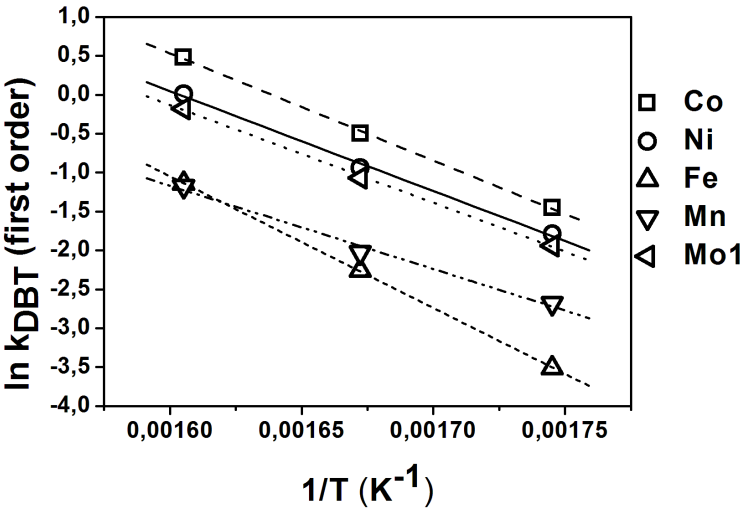

Figure 2.71: Arrhenius plot of DBT conversion at 300°C, 325°C and 350°C of catalysts after reduction.

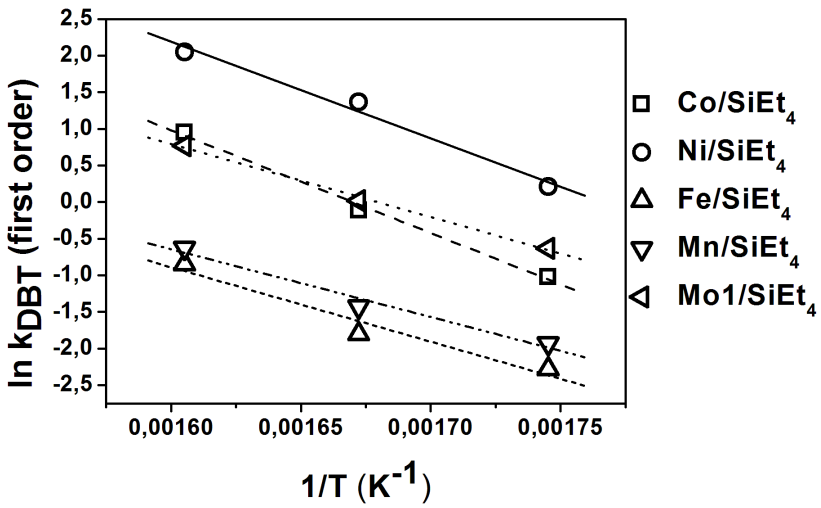

Figure 2.72: Arrhenius plot of DBT conversion at 300°C, 325°C and 350°C of catatlysts after $SiEt_4$ treatment.

treatment. Intriguingly, the **Ni/SiEt$_4$** catalyst demonstrated the highest ln k-values, with an increase of nearly two units. In general, activities for single metal catalysts, which are not promoted by a second metal are lower than the conversion seen for the Ni-containing catalyst. Although the loading of **Mo1/SiEt$_4$** is low compared to the other composites, the test displayed a high activity. Compared to the used MoS_2 standard on alumina with the same loading (1.6 wt%), the newly prepared catalyst showed a higher activity (by a factor of 1.2).[202]

Additionally, the nearly inactive materials (**Fe** and **Mn**) demonstrated a higher ln k-value after $SiEt_4$ treatment than before. It is well known that promoters are used for increasing the activity of metals dispersed in a supporting material (*e.g.* phosphorus) and even the matrix of the catalysts has an influence on their activity (*e.g.* alumina vs. alumina-zeolite).[203] The change of the electronic conditions before and after adding a promoter could also be the case with the silicon deposited from tetrathysilane on the material after the $SiEt_4$ treatment.

Figure 2.73 provides a better understanding of the dibenzothiophene conversion rates. The conversion yield delivered by the catalyst **Ni/SiEt$_4$** was nearly 100% at 350°C: it doubled after treatment of the **Ni** catalyst with $SiEt_4$. Taking a closer look at lower temperatures (300°C), the conversion yield even increased by a factor of 5.

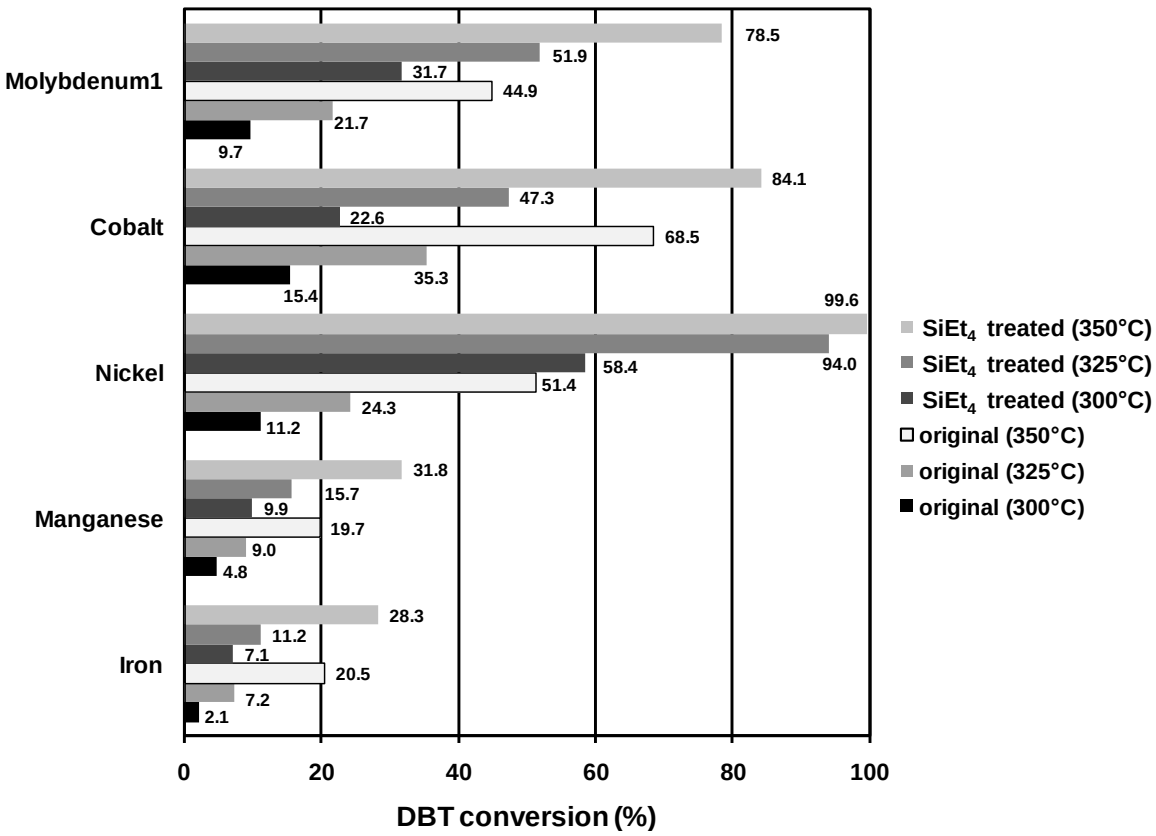

Figure 2.73: Conversion yield comparison of original ($SiEt_4$ untreated) and $SiEt_4$ treated material at 300°C, 325°C and 350°C.

The improvement observed for the **Mo1** catalyst was similar: at 350°C the conversion yield was also nearly twice as high as without $SiEt_4$ treatment, and at 300°C the yield increased by a factor of 3, when compared to using the original **Mo1** material. Also for the **Co** catalyst, an increase by a factor of about 1.5 at every temperature was observed

after $SiEt_4$ treatment. Even the nearly inactive composites **Fe** and **Mn** displayed a rise in the conversion yield by a factor of 1.5–2 from the untreated catalyst.

Based on the available investigations of the sample **Ni/SiEt$_4$** by XPS, the presence of nickel silicide in conjunction with oxide and silicate formation can be confirmed, which is a direct result of the generation of silicide phases during $SiEt_4$ treatment. This new phase supported on γ-alumina may be responsible for the observed promotion of the hydrodesulphurisation of dibenzothiophene, which is not entirely unusual, considering the enhancement of the activity of silicide modified nickel catalysts (leading to nickel silicides) towards phenylacetylene hydrogenation reported in the literature.[62]

3 Summary

The immense interest in nanostructured materials increased steadily over the last decade. These structures, which have a length scale of 1–100 nm, exhibit drastic changes in their physical properties compared to bulk materials. Chemistry, physics, biology and medicine are going hand in hand to synthesise and investigate new materials with novel properties and applications.

There are several routes to nanoparticles in a matrix, so-called nanocomposites. These materials are also well known as catalysts for various kinds of reactions.

In the first part of the work, the focus was on the synthesis of transition metal silicide nanoparticles, well-dispersed in an amorphous matrix (*e.g.* silica, alumina or charcoal) derived from suitable single-source precursors. Additionally, detailed characterisations of precursors and materials were carried out with a large array of methods (EDX, GPC, IR, NMR, N_2-sorption, Raman, SQUID, XRD, XPS, XRF) and DFT calculations were performed to gain insights into possible reaction mechanisms.

In the second part, the catalytic activity of newly prepared catalysts towards hydrodesulphurisation of dibenzothiophene was analysed. Additionally, a new catalyst preparation route by $SiEt_4$ treatment of metals on alumina was tested and the behaviour of the resulting materials towards ethylene hydrogenation and dibenzothiophene degradation was investigated.

The single-source precursor *cis*-$Fe(CO)_4(SiCl_3)_2$ is already known in the literature to be suitable for iron silicide layer or nanowire formation on a silica substrate.[67–69] Contrary to what has been postulated for the gas-phase decomposition of *cis*-$Fe(CO)_4(SiCl_3)_2$, its reaction with HMPA does not result in $SiCl_4$ elimination and formation of a (base-stabilised) metal silylene complex. Although one Fe–Si bond is broken, no transfer of Cl from the second $SiCl_3$ ligand is possible. This was confirmed by DFT calculations. Thus, the final product of this reaction is the new ionic complex $[SiCl_3(HMPA)_3]^+$ $[Fe(CO)_4SiCl_3]^-$.

Not only the iron carbonyl silyl complex reacts with HMPA to form an ionic compound, also the cobalt analogue $Co(CO)_4SiCl_3$ undergoes a Co–Si cleavage. $CpFe(CO)_2(SiCl_2SiCl_3)$ is a suitable complex to elucidate whether Fe–Si or Si–Si bond cleavage is favoured. The reaction was analysed by ^1H, ^{31}P and ^{29}Si NMR, which indicated the formation of $[Si_2Cl_2(HMPA)_3]^+[Fe(CO_2)Cp]^-$. These results support a direct Fe–Si bond cleavage.

Further investigations on the thermolysis behaviour of *cis*-$Fe(CO)_4(SiCl_3)_2$ revealed the formation of the new compound $Fe_2(CO)_6(\mu_2{-}SiCl_2)_3$, a dimeric iron complex with three bridging silylene ligands which was unequivocally characterised by single crystal X-ray diffraction. An alternative mechanistic rationale for $SiCl_4$ formation during thermolysis of *cis*-$Fe(CO)_4(SiCl_3)_2$ was proposed based on DFT calculations. The proposed mechanism involves chlorine abstraction by a $SiCl_3$ radical generated from homolytic Fe-Si bond cleavage, involving a singlet-triplet intersystem crossing.

DFT/GIAO ^{29}Si NMR shielding calculations provided satisfactory results for a set of 41 different molecules when compared to the experimental data. The need of this study arose out of the desire to use ^{29}Si NMR shielding calculations to assist the interpretation of NMR spectra of hypervalent silicon compounds, such as ($[SiCl_3(HMPA)_3]^+[Fe(CO)_4SiCl_3]^-$), where initial calculations showed rather large deviations between experimental data and calculated chemical shifts.

HCTH407/6-311+G(2d) consistently performed best among the different levels of theory employed in this work. The study focused on medium-sized compounds with at least one hypervalent silicon atom and investigated a structurally diverse selection of 27 different penta- and hexacoordinated compounds. It is evident that in order to obtain useful results for this class of molecules, employing a larger basis set than 6-31G(d,p) is absolutely necessary. Fortunately, employing a locally dense basis set (LDBS) already offered a dramatic improvement at very small additional computational costs.

In the present study, the choice of basis set exerted a much larger influence on the accuracy of the results than the choice of the functional. Employing the larger 6-311+G(2d) basis set on all atoms resulted in further improvements and furnished acceptable results for both tetravalent and hypervalent compounds. Nevertheless, a final note of caution is still warranted, as large differences between calculated and experimental shifts were observed for a few select cases, such as compounds exhibiting Si-H bonds.

The complex $Co(CO)_4SiCl_3$, which led to cobalt silicide nanowires under CVD condi-

tions[141] cannot necessarily be used for the preparation of silicide nanoparticles. Evidence is put forward that the nanoparticles formed upon thermolysis of $Co(CO)_4SiCl_3$ adsorbed on silica in a hydrogen atmosphere are not cobalt silicides as claimed in the literature,[38] but instead metallic cobalt nanoparticles with a Co_2SiO_4/CoO shell. Treatment at higher temperatures resulted in particles big enough to be characterised by powder XRD. Further XPS investigations showed that the oxide/silicate species are already present after H_2 treatment at 300°C, although in an amorphous state or in a thin layer, not detectable by XRD. Analogous experiments carried out on activated charcoal or graphite consequently resulted in the formation of pure cobalt nanoparticles, and formation of cobalt silicides was not observed either.

XPS measurements confirmed that a temperature of 500°C under hydrogen atmosphere for 2 h is not sufficient to reduce Co_2SiO_4/CoO in silica prepared by a sol-gel process to metallic cobalt.

The behaviour of three synthesised ferrocenyl-containing polymers upon thermolysis was studied (see Figure 3.1):

- poly[{(dimethylsiloxyl)ferrocenyl}diacetylene] (polymer **A**).
- poly[{(dimethylsilyl)ferrocenyl}diacetylene] (polymer **B**).
- poly(ferrocenylsilane) (polymer **C**).

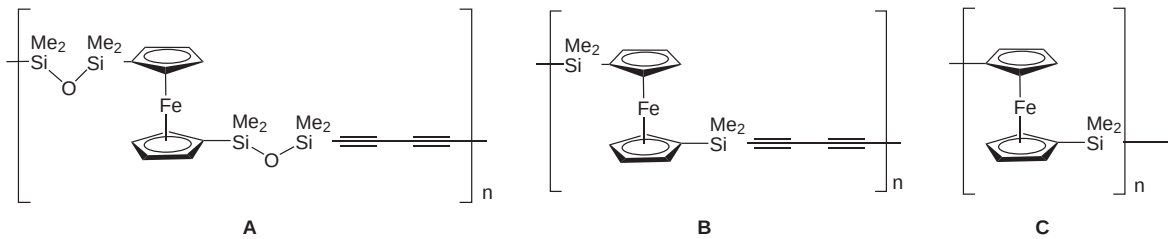

Figure 3.1: Structural formula of the ferrocenyl-containing polymers.

The synthesis of Fe_5Si_3 nanoparticles from poly[{(dimethylsiloxyl)ferrocenyl}diacetylene] (polymer **A**) was reproduced as reported in the literature.[86] It was confirmed that slow heating of the polymer to 1000°C led to α-Fe nanoparticles in a SiC/C matrix, while fast heating to 1000°C supports the formation of Fe_5Si_3. We were also able to demonstrate that fast heating of polymer **A** to 850°C yields α-Fe nanoparticles in a SiC/C matrix.

The synthesis of Fe_3Si and Fe_5Si_3 nanoparticles in a SiC/C matrix of varying size was

accomplished, tunable by different temperatures and organometallic precursors, which influence both the shape and the obtained iron silicide phases, and play an important role in the formation of different species. It was demonstrated that the carbon content of the polymer chains (polymer **B**) and higher temperatures support the formation of the thermodynamically metastable Fe_5Si_3 phase. At lower temperatures, the same polymer **B** yields the more stable Fe_3Si phase in the form of smaller and well-distributed nanoparticles encapsulated by SiC/C. Increasing the temperature does not lead to larger Fe_3Si particles but instead to the formation of a Fe_5Si_3 phase.

Gratifyingly, lowering the carbon content of the polymer chains as in poly(ferrocenylsilane) (polymer **C**) compared to poly[{(dimethylsilyl)ferrocenyl}diacetylene] (polymer **B**), led to the possibility of obtaining larger Fe_3Si nanoparticles even at higher temperatures. The recorded XRD patterns of all powders support the existence of a single crystalline iron silicide phase and the presence of carbon, which was also investigated by Raman spectroscopy, indicating the formation of a graphitic lattice during thermolysis of the organometallic polymers.

A further indication of particle formation is provided by the TEM and EDX analyses, which show a wide range of small and larger particles in each material. SQUID measurements confirmed soft ferromagnetic properties for all Fe_3Si containing samples. It was shown that the coercive force H_c of the nanoparticles changes with their size: for the smallest Fe_3Si nanoparticles (**BI**), the coercive force starts to decrease, presumably indicating the formation of single magnetic domain particles.

Further experiments on the applicability of suitable organometallic polymers for transition metal silicide formation arose from the synthesis of the following precursors:

- iron-containing poly[(dimethylsilylene)diacetylene].
- cobalt-containing poly[(dimethylsilylene)diacetylene].

They were synthesised by reaction of poly[(dimethylsilylene)diacetylene] with the corresponding metal carbonyls. After heat treatment at 1000°C under N_2, Fe_3Si and Co_2Si/Co nanoparticles in a SiC/C matrix were formed. Additionally, a mixture of $Mn_2(CO)_{10}$ and poly[(dimethylsilylene)diacetylene] yielded Mn_5Si_3 nanoparticles in a SiC/C matrix.

The magnetic behaviour of Co_2Si/Co nanoparticles was investigated by SQUID measurements. Field dependence of reduced magnetisation measured from 3–300 K exhib-

ited hysteresis loops in every case, which indicated ferromagnetic properties. Additionally, zero-field-cooled (ZFC) and field-cooled (FC) measurements were performed, which displayed a spin disorder system behaviour. Based on these results, a reentrant spin-glass behaviour is expected. Co_2Si is known to be paramagnetic in bulk form: due to the size reduction, the contribution of the surface increases and ferromagnetism can be expected. It is difficult to asses whether the ferromagnetism stems from the reduced size of the Co_2Si particles or from the contribution of the Co nanoparticles.

The synthesised nanocomposites were tested regarding their catalytic activity and selectivity towards hydrodesulphurisation of dibenzothiophene. Considering the cobalt-containing batch (sol-gel material, Co in SiO_2 and Co in charcoal), the sol-gel process derived material exhibited the best performance and favoured the direct desulphurisation route.

It turned out that all applied transition metal silicides show a low dibenzothiophene conversion rate. Among those, Co_2Si/Co nanoparticles had the best performance. Interestingly, the pretreatment of the catalysts had a significant influence on their behaviour. The application of H_2 before dibenzothiophene degradation tests on the catalysts had a negative impact on the conversion rate, compared to a presulphiding treatment. There is no significantly preferred hydrodesulphurisation route, direct desulphurisation and prehydrogenation both occur.

A new preparation route for transition metal silicide nanocomposites was carried out and tests of the resulting materials regarding their catalytic activity toward ethylene hydrogenation and hydrodesulphurisation of dibenzothiophene were performed. Different metals supported on γ-alumina (cobalt, nickel, manganese and molybdenum) were treated with tetraethylsilane at 400°C. This procedure turned the inactive molybdenum-containing material into an active catalyst towards ethylene hydrogenation.

The TEM pattern of the molybdenum-containing material (after tetraethylsilane treatment) revealed no significant particle formation, therefore a distribution of very small molybdenum nanoparticles or even clusters over the entire supporting material is assumed. EDX analyses confirmed the existence of molybdenum and silicon with a percentage corresponding to a Mo:Si stoichiometry of 2:5. The molybdenum content is too high for pure $MoSi_2$. Although XPS spectra only show formation of molybdenum oxide and silicate, molybdenum silicide formation cannot be ruled out: molybdenum silicide is sensitive to oxidation, which might have taken place during sample transfer

to the XPS instrument. Based on the available experimental evidence, it is impossible to identify the catalytically active phase.

Further hydrodesulphurisation tests with dibenzothiophene exhibited a significant improvement of the conversion by factors of 1.2–2 as compared to the untreated materials. The γ-alumina supported nickel material (containing nickel oxides, -silicates and -silicides), which was treated with tetraethylsilane at 400°C, shows the best improvement towards dibenzothiophene conversion. This catalyst was subsequently investigated by TEM imaging, which revealed no particle formation. Further XPS measurements confirmed the presence of nickel silicide besides nickel oxide and silicate. It is likely that the incorporation of silicon by treatment with tetraethylsilane leading to a silicide phase promotes the catalytic activity towards dibenzothiophene conversion.

4 Experimental Section

4.1 General Techniques

4.1.1 Synthesis of Organometallic Compounds

All reactions involving air- and moisture sensitive organometallic compounds were performed under an inert atmosphere of dry argon using standard Schlenk or glove box techniques. Anhydrous solvents were dried and purified according to standard procedures[204] and stored under an argon atmosphere over molecular sieves (3 or 4 Å, respectively). All reagents and solvents were purchased from Aldrich, Fluka, Merck, ABCR or Strem chemicals and used as received and if necessary stored under argon after opening them for the first time.

Deuterated solvents used for NMR experiments were purchased from Eurisotop (see Table 4.1), degassed using the freeze-pump-thaw technique and stored over 4 Å molecular sieves.

Table 4.1: Deuterated solvents used.

Name	Abbreviation	Supplier	Purity
[D_6]benzene	C_6D_6	euriso-top	99.5% D
[D_8]toluene		euriso-top	99.5% D
[D_3]chloroform	$CDCl_3$	euriso-top	99.5% D
[D_8]tetrahydrofurane	[D_8]THF	euriso-top	99.5% D

4.1.2 Thermolysis Experiments

All thermolysis experiments under air were performed with a muffle furnace (Ehret L3/11) equipped with a temperature controller.

Thermolysis experiments under nitrogen were carried out in a split tube furnace (Carbolite HST 12/300). For reduction reactions with hydrogen, a gas control system was used. The temperature program was set up with a temperature controller (Carbolite, type 3216).

4.2 Analytical Techniques

Energy-Dispersive X-ray Spectroscopy

Energy-dispersive X-ray spectroscopy (EDX) was performed with the TECNAI F20 or G20, line scan analyses were carried out in scanning transmission electron microscope (STEM) mode, using a real-time interactive imaging system using a high angle annular dark field (HAADF) detector.

Gel Permeation Chromatography

Gel permeation (GP) data were measured in THF relative to polystyrene standard and are therefore only estimates. Relative size exclusion chromatography (SEC) experiments were performed with a Waters system, which included a 515 HPLC pump, a W717 (R) autosampler, a W2410 (R) differential refractive index detector and Styragel columns (HR 0.5, 3, 4, linear), at 40°C at a rate of 1 ml/min. The system was calibrated using linear polystyrene standards. The molecular mass analysis was calculated with OmniSEC software.

Infrared Spectroscopy

Infrared spectroscopy (IR) measurements were performed on a Bruker Tensor 27 spectrometer (32 scans at a resolution of 4 cm^{-1}) using a liquid cell or a Zn crystal. IR bands are classified as either very strong (vs), strong (s), medium (m), weak (w), sh (shoulder) or br (broad).

Nuclear Magnetic Resonance Spectroscopy

^{1}H, ^{13}C and ^{31}P NMR spectra were recorded on a Bruker Avance 250 (250.13 MHz {^{1}H}, 62.86 MHz {^{13}C}, 100.13 MHz {^{31}P}) spectrometer. ^{29}Si NMR spectra were recorded on a Bruker Avance 300 (59.63 MHz {^{29}Si}) spectrometer. Chemical shifts are reported as δ values with TMS (^{1}H, ^{13}C, ^{29}Si) as standard. For ^{31}P NMR measurements H_3PO_4 was used as an internal standard.

Table 4.2: NMR Abbreviations

Abbreviation	Denotation
δ	chemical shift
s	singlet
d	doublet
t	triplet
q	quartet
m	multiplet
br	broad
J	coupling constant

Nitrogen Absorption

Nitrogen absorption measurements were performed at 77 K on Micromeritics ASAP 2010 and ASAP 2020 instruments. The surface area was calculated according to Brunauer, Emmett and Teller (BET) and t-plot method, and the pore size distribution according to Barrett, Joyner and Halenda (BJH) applied on adsorption and desorption branches of the isotherm. The samples were degassed under vacuum at 50 or 100°C for at least 5 h prior to the measurements.

Raman Spectroscopy

Raman spectra were recorded on a confocal Raman microscope (LabRAM system, Jobin-Yvon/Dilor, Lille, France). In this system, the Raman spectrometer was coupled to a microscope (model BX40, Olympus). Raman scattering was excited by a He-Ne laser at 632.8 nm and a laser power of 8 mW. The dispersive spectrometer was equipped with a grating of 600 lines/mm, giving a spectral resolution of 10 cm^{-1}. The detector was a Peltier-cooled CCD detector (ISA, Edison, NJ). The laser beam was focused

manually on the sample by means of a 20x microscope objective. Accumulation time for one spectrum was 2 times 600 s.

Single Crystal X-Ray Diffraction

Single crystal X-ray diffraction experiments were performed on a Siemens SMART and a Bruker-AXS APEX diffractometer with CCD area detectors and a crystal-to-detector distance of 5.0 cm using graphite-monochromated Mo-K_α radiation (λ = 71.073 pm). Data collection covered a hemisphere of the reciprocal space by recording three sets of exposures, each of them exhibiting a different ϕ angle. The time period of each exposure was 5 to 30 s each of them covering 0.3° in ω. The data were corrected for polarisation and Lorentz effects, and an empirical absorption correction (SADABS) was applied.[205] The structures were solved with direct methods (SHELXS97) and refinement to convergence was carried out with the full-matrix least squares method based on F^2 (SHELXL97) with anisotropic structure parameters for all non-hydrogen atoms.[206,207] The hydrogen atoms were placed on calculated positions and refined riding on their parent atoms.

Superconducting Quantum Interference Device Magnetometer

Magnetisation of powders was measured by a Cryogenics S700X SQUID magnetometer at T = 3 K, 50 K, 100 K, 200 K and 300 K in the wide field range. Spurious contributions to the measured signal, other than from the nanoparticles, were avoided by using diamagnetic sample holders with uniform mass and magnetic moment distribution along the whole SQUID scanning length.

Transmission Electron Microscopy

The obtained powders were deposited on a carbon grid for transmission electron microscopy (TEM) analysis. TEM images were obtained using a TECNAI F20 analytical microscope equipped with an S-Twin objective lens and a field emission source operating at 200 kV and were recorded with a Gatan Orius SC600 CCD camera. The TECNAI G20 microscope with a LaB_6-cathode and a CCD camera was also used.

X-ray Photoelectron Spectroscopy

XPS spectra were recorded on a Perkin-Elmer ϕ 5600ci spectrometer using standard Al radiation (1486.6 eV) working at 350 W. The spectrometer was calibrated by assuming the binding energy (BE) of the Au4f$_{7/2}$ line at 83.9 eV with respect to the Fermi level. The standard deviation for the BE values was 0.15 eV. The reported BE were corrected for the charging effects, assigning, in the outer layers where contamination carbon is still present, to the C1s line of carbon the BE value of 284.6 eV.[152,153] Survey scans (187.85 pass energy, 1 eV/step, 25 ms per step) were obtained in the 0–1300 eV range. Detailed scans (58.7 eV pass energy, 0.1 eV/step, 100–150 ms per step) were recorded for the O1s, C1s, Co2p, CoLMM, Ni2p, Mo3d, Si2p, Si2s regions. The atomic composition, after a Shirley type background subtraction, was evaluated using sensitivity factors supplied by Perkin-Elmer.[152] Samples were introduced directly, by a fast entry lock system, into the XPS analytical chamber. Peak assignments were carried out using values reported in the XPS Handbook, the NIST XPS Database and references therein given in the text.[152–156,159,165]

Powder X-ray Diffraction

X-Ray diffraction (XRD) analyses of powders were carried out on a Philips XPert Pro diffractometer system [Cu K$\alpha_{1,2}$ radiation (λ = 1.54060, 1.54439 Å)] equipped with an XCelerator multi-channel detector, Bragg Brentano geometry, silicon single crystal sample holder. The diffraction pattern was recorded between 5 and 100° (2θ) with 1s/step and a step size of 0.02°.

X-ray Fluorescence

Cobalt, iron and manganese were quantified by a Panalytical Axios Advanced wavelength-dispersive X-ray fluorescence spectrometer. The used system was equipped with a rhodium X-ray tube, operated at 50 kV and 50 mA. Background corrected intensities were measured at wavelengths of 17.89 Å (Co), 1.93 Å (Fe) and 2.10 Å (Mn).

4.3 Computational Details

Due to practical constraints, two different software suites were employed for the density functional theory calculations carried out in the present work: in the studies in Section 2.1 and Section 2.3 the Gaussian 03 suite of programs (revision D.01)[208] were used, while calculations on the HMPA-induced Fe–Si bond cleavage (see Section 2.2) were performed with the GAMESS (US) QC package.[209] This posed no problems, since the theoretical studies were carried out independently.

The computations of Section 2.1 were carried out at the BLYP/6-311G(3df)// BLYP/ m6-31G(d) level of theory with the pure BLYP density functional,[210,211] employing the triple zeta basis set 6-311+G(2df) for single point calculations and the double zeta basis set m6-31G(d) in unconstrained geometry optimisations,[212] transition state searches, and frequency calculations on all localised stationary points on the potential energy surface. Electronic energies obtained from single point calculations were corrected with unscaled harmonic zero point energies and thermal corrections at T = 298.15 K obtained at the lower level of theory, and are therefore reported as Gibbs free energies. All calculations were carried out with the Gaussian 03 program package,[208] and basis sets were retrieved from the EMSL Basis Set Exchange Library.[213]

Computations in Section 2.2 were performed with the hybrid B3LYP density functional[214] in conjunction with double zeta basis sets 6-31G* (for N, O, P, and Si atoms), 6-31G (for C and H atoms) and the relativistic Stuttgart effective core potentials (large core for Cl atoms and small core for the Fe atom). Basis sets were retrieved from the EMSL Basis Set Exchange Library.[213] Geometry optimisations and transition state searches were carried out with the PC GAMESS version[209] of the GAMESS (US) QC package[215] without any symmetry constraints. Obtained geometries were additionally characterised by frequency calculations, exhibiting no imaginary frequencies for ground states and only one imaginary frequency for transition states. Energies include unscaled harmonic zero point energies and thermal corrections at T = 298.15 K and are therefore reported as Gibbs Free Energies. Solvent effects were computed using the Polarisable Continuum Model[216] with toluene as a solvent.

For ^{29}Si NMR shielding calculations in Section 2.3, density functional theory calculations were carried out using the gauge including atomic orbital (GIAO) method in conjunction with the hybrid B3LYP[214] functional, the generalised gradient approximation functional (GGA) BPW91[217,218] and the meta-GGA functional HCTH407. The

choice of functionals was motivated by the findings of Apeloig *et al.*[104] and allows for a convenient comparison with their published results. Three different basis sets were used for ^{29}Si NMR shielding calculations: Pople's double-zeta, split-valence basis set 6-31G(d,p) with additional polarisation functions on all atoms; the triple-zeta, split-valence basis set 6-311+G(2d) with additional diffuse and polarisation functions only on heavy atoms; a combination thereof, with 6-31G(d,p) on all atoms except Si, where 6-311+G(2d) was used, which for the purpose of this study is referred to as locally dense basis set (LDBS).[219–221] The basis sets and references for all Pople-type basis sets used in this study are provided at `https://bse.pnl.gov/bse/portal`. To facilitate the comparison of calculated and experimental chemical shifts, the calculated isotropic shielding constants were converted into chemical shifts using tetramethylsilane (TMS) as a reference: for this purpose, the shielding constants for TMS were calculated at every level of theory used in the study and are shown in Table 2.7 and 5.3, respectively. All geometries were optimised at the B3LYP/6-31G(d,p) level of theory, which is known to produce reliable results with regard to convergence of structural parameters.[222,223] Where available (compounds **11**–**41**), geometry optimisations were started from structures obtained from the Cambridge Crystallographic Data Center *via* `www.ccdc.cam.ac.uk` or the Inorganic Crystal Structure Database FIZ Karlsruhe. Where appropriate, symmetry constraints were applied (*i.e.* when the experimentally available NMR shifts indicated the presence of molecular symmetry). All calculations were carried out with the Gaussian 03 suite of programs (revision D.01[208]). For the six outliers, geometry optimisations and shielding calculations with HCTH407/6-311+G(2d) were carried out in conjunction with the integral equation formalism polarised continuum model (IEF-PCM)[146–148] in order to model the influence of the solvent.

4.4 Synthesis of Precursors

4.4.1 Synthesis of $Fe(CO)_4(SiCl_3)_2$

A suspension of 0.5 g of triirondodecacarbonyl $Fe_3(CO)_{12}$ (0.99 mmol) and 5 mL of trichlorosilane $HSiCl_3$ (50 mmol) was loaded in a thick-walled glass tube.[68] The sealed vial was then heated in an autoclave at 120°C for 24 h. After cooling to room temperature, the mixture was transferred to a sublimation apparatus. Excess $HSiCl_3$ was removed under dynamic vacuum and the resulting yellow solid was sublimed at 90°C

under vacuum for several hours. The resulting white crystals were collected from the cold finger for further analysis.

Yield: 0.9 g (68%); **^{13}C NMR** (δ [ppm], C_6D_6, 20°C): 200.71 (CO); **^{29}Si NMR** (δ [ppm], C_6D_6, 20°C): 47.46 (Fe-$SiCl_3$); **IR** (λ [cm^{-1}], C_6D_6): 2082 (s), 2073 (s) (C≡O).

4.4.2 Synthesis of $Fe_2(CO)_6(\mu_2{-}SiCl_2)_3$

A 20-cm^3 glass vial was charged with 0.20 g of *cis*-$Fe(CO)_4(SiCl_3)_2$ (0.46 mmol) and sealed under argon atmosphere. The vial was heated in a furnace to 350°C for 30 min with a heating rate of 2°C/min. After cooling to room temperature, $FeCl_2$ and yellow, needle-like crystals were obtained.

Yield: 0.03 g (12%); **IR** (λ [cm^{-1}], toluene): 2022 (vs), 2001(s) (C≡O).

4.4.3 Synthesis of $[SiCl_3(HMPA)_3]^+[Fe(CO)_4SiCl_3]^-$

HMPA (0.10 mL, 5.6 mmol) was added by a syringe to a solution of $Fe(CO)_4(SiCl_3)_2$ (0.1 g, 0.2 mmol) in 2 mL of [D_8]toluene. The reaction was continued for 10 min in an ultrasonic bath. Monitoring the reaction by ^{1}H NMR showed the reaction to be almost complete, also evidenced by almost quantitative disappearance of the starting materials in the ^{29}Si NMR spectrum. Slow addition of 1.5 mL *n*-hexane gave colourless crystals.

Yield: 86% (quantified by ^{1}H NMR); **^{1}H NMR** (δ [ppm], [D_8]toluene, 20°C): 2.65 (s, 54 H, CH_3); **^{13}C NMR** (δ [ppm], [D_8]toluene, 20°C): 216.60 (CO), 215.70 (CO), 36.51 (CH_3); **^{31}P NMR** (δ [ppm], [D_8]toluene, 20°C): 18.40 (s, 3 P, O=PN$(Me_2)_3$); **^{29}Si NMR** (δ [ppm], [D_8]toluene, 20°C): 68.11 (Fe-$SiCl_3$), -205.84 ($SiCl_3(HMPA)_3$); **IR** (λ [cm^{-1}], [D_8]toluene): 2029 (w), 1951 (w), 1923 (s), 1910 (s) (C≡O).

4.4.4 Synthesis of 1-[Dicarbonyl(η^5-cyclopentadienyl)ferrio]-pentachlorodisilane

The compound was synthesised according to the literature.[140] A suspension of 2 g (10.8 mmol) of Na[$Fe(CO)_2Cp$] in 100 mL cyclohexane was treated with 2 mL (12 mmol) of

hexachlorodilsilane. Subsequently, the mixture was stirred for 4 d at room temperature in the absence of light. The formed insoluble NaCl and unreacted $Na[Fe(CO)_2Cp]$ were filtered and excess of hexachlorodisilane and solvent were removed under vacuum. The residue was extracted four times with 30 mL *n*-pentane. The extracts were reduced to about 15 mL and cooled to -78°C. A pale yellow solid precipitated, which was filtered and washed with about 10 mL *n*-pentane. The product was dried *in vacuo* for further analyses.

Yield: 1.28 g (34%); **^{1}H NMR** (δ [ppm], C_6D_6, 20°C): 4.11 (s, 5 H, Cp); **^{29}Si NMR** (δ [ppm], C_6D_6, 20°C): 77.21 (α-Si), -2.98 (β-Si); **IR** (λ [cm^{-1}], C_6D_6): 1912 (vs), 1865 (vs) (C≡O).

4.4.5 Synthesis of $[Si_2Cl_2(HMPA)_3]^+[Fe(CO_2)Cp]^-$

0.05 g (0.1 mmol) of 1-[dicarbonyl(η^5-cyclopentadienyl)ferrio]-pentachlorodisilane were dissolved in 0.7 ml C_6D_6. After addition of 0.07 mL (0.4 mmol) of HMPA, the reaction was treated in an ultrasonic bath for 20 min at room temperature. The reaction was monitored by ^{1}H NMR. After 1 h no further reaction was observed.

Yield: 4.3% (quantified by ^{1}H NMR); **^{1}H NMR** (δ [ppm], C_6D_6, 20°C): 4.69 (s, 5 H, Cp), 2.34 (s, 54 H, CH_3); **^{31}P NMR** (δ [ppm], C_6D_6, 20°C): 22.12 (s, 3 P, $O{=}PN(Me_2)_3$) **^{29}Si NMR** (δ [ppm], C_6D_6, 20°C): -199.23 (α-Si), -0.96 (β-Si); **IR** (λ [cm^{-1}], C_6D_6): 1951 (vs), 1903 (vs) (C≡O).

4.4.6 Synthesis of $Co(CO)_4SiCl_3$

In a typical experiment, 3 mL of trichlorosilane $HSiCl_3$ (0.03 mol) and 0.5 g of dicobaltoctacarbonyl $Co_2(CO)_8$ (1.46 mmol) were loaded into a thick-walled glass tube. The sealed vessel was then heated at 120°C for 2 d. After cooling, the reaction mixture was transferred to a sublimation apparatus in a glove box. Excess $HSiCl_3$ was removed under dynamic vacuum and the resulting solid was sublimed at 40°C and for 2 h before the product was collected from the cold finger of the sublimation apparatus inside the glove box. Yellow crystals were obtained.

Yield: 0.5 g (61%); **^{13}C NMR** (δ [ppm], C_6D_6, 20°C): 200.3 (CO); **^{29}Si NMR** (δ [ppm], C_6D_6, 20°C): 40.01 (Co-$SiCl_3$); **IR** (λ [cm^{-1}], C_6D_6): 2120 (w), 2066 (w), 2039

(s) (C≡O).

4.4.7 Synthesis of $[SiCl_3(HMPA)_3]^+[Co(CO)_4]^-$

HMPA (0.08 mL, 0.5 mmol) was added by a syringe to a solution of $Co(CO)_4SiCl_3$ (0.05 g, 0.16 mmol) in 1 mL of C_6D_6. The reaction was continued for several minutes in an ultrasonic bath, while the yellow solution turned pale blue. Monitoring the reaction by ^{31}P NMR showed the reaction to be complete, also evidenced by almost quantitative disappearance of the starting materials in the ^{29}Si NMR spectrum.

Yield: 100% (quantified by ^1H NMR); **^{1}H NMR** (δ [ppm], C_6D_6, 20°C): 2.33 (s, 54 H, CH_3); **^{13}C NMR** (δ [ppm], C_6D_6, 20°C): 214.61 (CO); **^{31}P NMR** (δ [ppm], C_6D_6, 20°C): 18.22 (s, 3 P, O=PN$(Me_2)_3$); **^{29}Si NMR** (δ [ppm], C_6D_6, 20°C): -205.81 ($SiCl_3(HMPA)_3$); **IR** (λ [cm^{-1}], C_6D_6): 2160 (w), 2094 (w), 1961 (s), 1885 (s) (C≡O).

4.4.8 Synthesis of Poly(ferrocenylsilane)

2.5 M *n*-butyllithium (30 mL, 79 mmol) was added dropwise to a solution of 7.0 g of ferrocene (Fc, 38 mmol) in 100 mL of *n*-hexane and 14 mL of tetramethylethylenediamine (TMEDA, 86 mmol). The solution turned orange, was stirred at room temperature for 10 h and was then cooled to 0°C. A solution of 7 mL of dichlorodimethylsilane (58 mmol) in 30 mL of n-hexane was added slowly. The mixture was warmed to room temperature and stirred over night. After removal of LiCl by filtration, the solution was evaporated under vacuum and 60 mL of toluene was added to the solution. A few milligrams of $PtCl_2$ were added to the solution which was then heated to 80–90°C for 3 h. The mixture was then cooled to room temperature, filtered, and the solvent evaporated under vacuum. A dark red viscous liquid was obtained.[224] Traces of ferrocene were still present; the product was not further purified prior to subsequent thermolysis.

Yield: 8.1 g (91%); **^{1}H NMR** (δ [ppm], $CDCl_3$, 20°C): 4.17 (t, J = 1.7 Hz, 4 H, Cp), 4.11 (t, J = 1.7 Hz, 4 H, Cp), 0.53 (s, 6 H, CH_3); **GPC** (THF *vs.* polystyrene): M_w 1739, M_n 1143, polydispersity 2.

4.4.9 Synthesis of 1,1'-Bis(chlorodimethylsilyl)ferrocene

To a solution of 5.0 g of ferrocene (Fc, 27 mmol) in 40 mL of *n*-hexane and 9 mL of tetramethylethylenediamine (TMEDA, 55 mmol), 21 mL of 2.5 M *n*-butyllithium (55 mmol) were added dropwise. Subsequently, the mixture was stirred for 3 h at RT. The solution turned orange and was cooled down to 0°C. A solution of 10 mL chlorodimethylsilane (90 mmol) in 20 mL was added slowly and the mixture was warmed to RT and stirred over night. After hydrolysis (HCl) under ice cooling, the solution was extracted several times with *n*-pentane. The organic phases were collected and dried over $MgSO_4$. The solution was filtered, the volatiles were evaporated under vacuum and a red liquid was obtained. Ferrocene was still present, further purification wasn't attempted during the synthesis.

Yield: 6.2 g (75%). **^{1}H NMR** (δ [ppm], C_6D_6): 4.11 (s, 4 H, Cp), 4.05 (s, 4 H, Cp), 0.55 (s, 12 H, Si-CH_3); **IR** (λ [cm^{-1}], C_6H_6): 2959 (w, C-H), 2278 (vs, Fc).

4.4.10 Synthesis of Poly[{(dimethylsilyl)ferrocenyl}diacetylene]

The polymer was obtained by modification of the procedure given in the literature.[83] A solution of 10 mL 2.5 M of *n*-butyllithium (26 mmol) and 19 mL of THF was cooled to -78°C. 1 mL of hexachlorobutadiene (6 mmol) was added, and the mixture was stirred for 3 h at room temperature. The solution of the lithiated diacetylene was added at -78°C to a suspension of $MgBr_2$ (2 g, 6 mmol) in 20 mL of THF. The mixture was warmed to RT and stirred for 1 h. Subsequently, 1 g (2 mmol) of 1,1'-bis(chlorodimethylsilylene)ferrocene was dissolved in 15 mL THF and added to the mixture. The reaction was stirred at room temperature over night. A 0.5 mL portion of methanol was added to substitute residual Si–Cl bonds, and the reaction was stirred again for 2 h at room temperature. After hydrolysis at 0°C, the mixture was extracted several times with *n*-pentane and dried over $MgSO_4$. The organic phase was filtered and the solvent was removed under vacuum resulting in a brown viscous liquid. Impurities of residual ferrocene and hydrolysed silicon species of the product were not further separated.

Yield: 1.7 g (94%); **^{1}H NMR** (δ [ppm], $CDCl_3$, 20°C): 4.22 (s, 4 H, Cp), 4.20 (s, 4 H, Cp), 0.42 (s, 12 H, Si-CH_3); **^{13}C NMR** (δ [ppm], $CDCl_3$, 20°C): 88.47 (Si-C≡C),

85.30 (Si-C≡C), 72.34 (Cp), 71.54 (Cp), 68.84 (C≡CH), -0.51 (Si-CH_3); **^{29}Si NMR** (δ [ppm], $CDCl_3$, 20°C): -19.61 (Si-C≡C); **IR** (λ [cm^{-1}], $CHCl_3$): 3306 (s, ≡C-H), 2962 (s, Si-CH_3), 2066 (s, C≡C); **GPC** (THF *vs.* polystyrene): M_w 22136, M_n 2667, polydispersity 8.

4.4.11 Synthesis of Poly[{(dimethylsiloxyl)ferrocenyl}diacetylene]

A solution of 10 mL THF and 10.2 mL of 2.5 M *n*-butyllitihium (26 mmol) was cooled to -78°C. Subsequently, 1 mL of hexachlorobutadiene (6 mmol) was added and the mixture was stirred for 3 h at RT. The resulting dark slurry was transferred to a solution of 1.3 mL dichlorotetramethyldisiloxane (6 mmol) in 5 mL THF at 0°C and was stirred for 30 min at RT. After cooling again to 0°C, a solution of 1.3 g ferrocene (Fc, 6 mmol) in 10 mL THF and 2.3 mL tetramethylethylenediamine (TMEDA, 34 mmol) 5.7 mL of 2.5 M *n*-butyllithium (34 mmol) was added dropwise. The mixture was warmed to RT and stirred for 1 h and the reaction was subsequently quenched with an aqueous NH_4Cl solution and extracted with diethyl ether. The combined extracts were dried over $MgSO_4$, filtered and the solvent removed, leaving a viscous brown oil. Impurities of residual ferrocene and hydrolysed silicon species of the product were not further purified.

Yield: 1.6 g (74%); **^{1}H NMR** (δ [ppm], $CDCl_3$, 20°C): 4.35 (s, 4 H, Cp), 4.14 (s, 4 H, Cp), 0.27 (s, 12 H, Si-CH_3); **^{13}C NMR** (δ [ppm], $CDCl_3$, 20°C): 88.01 (Si-C≡C), 86.30 (Si-C≡C), 72.84 (Cp), 70.96 (Cp), 68.61 (C≡CH), -0.94 (Si-CH_3); **IR** (λ [cm^{-1}], $CHCl_3$): 3302 (s, ≡C-H), 2961 (s, Si-CH_3), 2064 (s, C≡C); **GPC** (THF *vs.* polystyrene): M_w 1553, M_n 621, polydispersity 2.

4.4.12 Synthesis of Poly[(dimethylsilylene)diacetylene]

In a modified procedure of Corriu *et al.*[225] a mixture of 50 mL 2.5 M *n*-butyllithium (132 mmol) and 50 mL dry tetrahydrofurane was cooled to -78 °C. At this temperature, 5.5 mL hexachlorobutadiene (33 mmol) was added dropwise. After stirring for 6 h at RT, a solution of 6 mL dichlorodimethylsilane (57 mmol) in 10 mL of dry tetrahydrofurane was added by a dropping funnel at 0°C. The reaction mixture was stirred over night at RT. 1 mL of methanol was added to substitute the residual Si-Cl bonds and the

reaction was stirred for 2 h at RT After hydrolysis at 0°C, the mixture was extracted several times with *n*-pentane and dried over $MgSO_4$. The organic phase was filtered and the solvent was removed under vacuum. A brown solid was obtained. Impurities consisting of hydrolysed silicon species of the product were not further purified.

Yield: 4.2 g (91%); **^{1}H NMR** (δ [ppm], $CDCl_3$, 20°C): 0.37 (s, 12 H, Si-CH_3); **^{13}C NMR** (δ [ppm], $CDCl_3$, 20°C): 88.95 (Si-C≡C), 82.01 (Si-C≡C), 65.31 (C≡CH), -0.58 (Si-CH_3); **IR** (λ [cm^{-1}], $CHCl_3$): 2965 (s, Si-CH_3), 2072 (s C≡C); **GPC** (THF *vs.* polystyrene): M_w 535174, M_n 346466, polydispersity 2.

4.4.13 Synthesis of Iron-Containing Poly[(dimethylsilylene)diacetylene]

In a modified reaction, 0.7 g poly[(dimethylsilylene)diacetylene] was dissolved in 40 mL of dry tetrahydrofurane. After adding 0.3 g of $Fe_2(CO)_9$ (0.8 mmol) to the solution, the mixture was stirred at RT until gas evolution ceased.[172] The solvent was removed and the obtained complexed poly[(silylene)diacetylene with $Fe(CO)_x$ was washed with *n*-pentane and subsequently dried under vacuum.

Yield: 0.8 g; **IR** (λ [cm^{-1}], $CHCl_3$): 2962 (w, Si-CH_3), 2162 (s, C≡C) 2019 (br), 1994 (br) (C≡O), 1563 (w, C=O); **GPC** (THF *vs.* polystyrene): M_w 39493, M_n 12723, polydispersity 3.

4.4.14 Synthesis of Cobalt-Containing Poly[(dimethylsilylene)diacetylene]

In a typical reaction, 2.3 g poly[(dimethylsilylene)diacetylene] was dissolved in 40 mL of dry tetrahydrofurane. After adding 2.4 g of $Co_2(CO)_8$ (7 mmol) to the solution, the mixture was stirred at RT until gas evolution ceased.[83] The solvent was removed and the product was dried under vacuum.

Yield: 4.3 g; **IR** (λ [cm^{-1}], $CHCl_3$): 2964 (w, Si-CH_3), 2080 (vs), 2064 (vs), 2034 (vs) (CO), 2172 (s, C≡C); **GPC** (THF *vs.* polystyrene): M_w 438861, M_n 52669, polydispersity 8.

4.4.15 Mixture of $Mn_2(CO)_{10}$ and Poly[(dimethylsilylene)diacetylene]

A mixture of 2.3 g of $Mn_2(CO)_{10}$ (6 mmol) and 1.5 g of poly[(dimethylsilylene)diacetylene] was stirred in dry tetrahydrofurane for several hours, subsequently the solvent was removed under vacuum.

4.5 Preparation of Nanocomposites

4.5.1 Preparation of Cobalt Nanoparticles in Silica, Charcoal or Graphite

Silica (Merck, particle size 0.015–0.040 nm) was heated in air at 600°C for 24 h to remove residual water. An amount of 0.5 g (1.64 mmol) of $Co(CO)_4SiCl_3$ was thoroughly mixed with 0.7 g of SiO_2, charcoal or graphite, respectively. The mixtures were heated to 65°C under argon for 160 min to adsorb $Co(CO)_4SiCl_3$ homogeneously on SiO_2, charcoal or graphite. Thermolysis under H_2/N_2 was performed in a split tube furnace. The $Co(CO)_4SiCl_3$-loaded materials were heated under a H_2/N_2 mixture (H_2 flow 20 mL/min, N_2 flow 190 mL/min) with a heating rate of 10°C/min to 300°C and held at this temperature for 120 min at atmospheric pressure. A grey powder was obtained for the silica support. The carbon supported materials were black powders. Part of the $Co(CO)_4SiCl_3$-loaded silica was additionally heated to 600°C and 1000°C under N_2 (200 mL/min).

Table 4.3: Measured surface area by N_2-sorption experiments

	Co in silica	Co in charcoal	Co in graphite
S_{BET} (m^2/g)	414	645	10

4.5.2 Preparation of Cobalt Nanoparticles in SiO_2 by a Sol-Gel Route

To a suspension of 2 g cobalt(II)acetate (8 mmol) in 100 mL of ethanol, the specified amount of 3.56 g [*N*-(aminoethyl)aminopropyl]trimethoxysilane (16 mmol) was added.

The mixture was stirred at room temperature until a clear solution was obtained (about 1 h). After addition of 10 g TEOS (48 mmol), 32.4 mL aqueous 0.2 N ammonia was added. The resulting dark violet mixture was heated to 70°C for 72 h in a closed vessel. Then the solvent was removed at 60°C and 100 mbar. The obtained xerogel was dried at 70°C under vacuum for several hours to remove adsorbed water and residual alcohol.[161]

The polycondensate was milled, placed in a horizontal tube furnace and calcined under air flow (200 mL/min) to 550°C for 1 h with a heating rate of 10°C/min. After cooling to room temperature a dark blue material was obtained. The composite subsequently was treated with hydrogen (200 mL/min) at 500°C for 2 h (heating rate 10°C/min). By this approach a powder was received, which was still dark blue in appearance after reduction.

$\mathbf{S_{BET}}$: 346 m^2/g.

4.5.3 Preparation of Transition Metal Silicide Nanoparticles in SiC/C

All synthesised metal-containing polymers of Section 4.4 were thermolysed in a tube furnace equipped with a gas flow controller. The polymers were heated in a nitrogen atmosphere (N_2 flow 200 mL/min) and cooled under nitrogen to room temperature for further analyses.

- **10–30 nm Fe_3Si nanoparticles**

  An amount of 0.7 g of poly[(dimethylsilylene)ferrocenyldiacetylene] was thermolysed under N_2. The polymer was heated to 250°C with a heating rate of 10°C/min, held at that temperature for 1 h, heated to 400°C, held at this temperature for another hour, then heated to 850°C and held at this temperature for 3 min.

  BI Yield: 0.4 g (60 wt%); **Iron analysis**: 26.7 wt%; $\mathbf{S_{BET}}$: 206 m^2/g.

- **10–100 nm Fe_3Si nanoparticles**

  In a similar procedure, 2 g of poly(ferrocenylsilane) was thermolysed in the same way, but with a maximum temperature of 1000°C.

  CII Yield: 0.5 g (22 wt%); **Iron analysis**: 39.8 wt%; $\mathbf{S_{BET}}$: 113 m^2/g.

Thermolysis 2 g of iron-containing poly[(dimethylsilylene)diacetylene] in the same way as above (maximum temperature of 1000°C).

DII Yield: 1.3 g (64 wt%); **Iron analysis**: 17.5 wt%; $\mathbf{S_{BET}}$: 348 m^2/g.

- **500 nm Fe_3Si particles**

  In another experiment, 2 g of poly(ferrocenylsilane) was heated to 1000°C for 4 h under a nitrogen atmosphere with a heating rate of 10°C/min.

  CIII Yield: 0.2 g (12 wt%); **Iron analysis**: 50.9 wt%; $\mathbf{S_{BET}}$: 104 m^2/g.

- **10–100 nm Fe_5Si_3 nanoparticles**

  Poly[(dimethylsilylene)ferrocenyldiacetylene] (0.4 g) was heated to 250°C with a heating rate of 10°C/min, held at that temperature for 1 h, heated to 400°C, held at this temperature for another hour, then heated to 1000°C and held at this temperature for 3 min.

  BII Yield: 0.2 g (60 wt%); **Iron analysis**: 26.7 wt%; $\mathbf{S_{BET}}$: 182 m^2/g.

  The same procedure was applied to 1 g of ferrocenyl-containing poly[(siloxy)diacetylene], which also led to Fe_5Si_3 nanoparticles distributed in a SiC/C matrix.

  AII Yield: 0.6 g (55 wt%); **Iron analysis**: 14 wt%; $\mathbf{S_{BET}}$: 239 m^2/g.

- **10–100 nm Co_2Si/Co nanoparticles**

  Cobalt-containing poly[(dimethylsilylene)diacetylene] (0.8 g) was heated to 250°C with a heating rate of 10°C/min, held at that temperature for 1 h, heated to 400°C, held at this temperature for another hour, then heated to 1000°C and held at this temperature for 3 min.

  EII Yield: 0.6 g (72 wt%); **Cobalt analysis**: 42 wt%; $\mathbf{S_{BET}}$: 124 m^2/g.

- **10–100 nm Mn_5Si_3 nanoparticles**

  A mixture of $Mn_2(CO)_{10}$ and Poly[(dimethylsilylene)diacetylene] (1.5 g) was thermolysed in the same manner as the cobalt-containing material.

  FII Yield: 0.3 g (19 wt%); **Manganese analysis**: 14 wt%; $\mathbf{S_{BET}}$: 95 m^2/g.

All obtained materials were milled to powders for further characterisation.

4.5.4 Preparation of Transition Metal Nanoparticles in γ-Al_2O_3

For the preparation of transition metal nanoparticles on γ-Al_2O_3, five metals were chosen: cobalt, nickel, iron, manganese and molybdenum. The materials were all synthesised in a similar procedure, except for the molybdenum-containing material.

Preparation of metal salt solutions

- **Co** solution: to obtain the cobalt-containing composite, 2.2 g of $CoCO_3$ were suspended in 8.4 mL of H_2O. After the addition of 3.6 g of citric acid (19 mmol), CO_2 gas evolved and the mixture was refluxed for 10 min. Subsequently, the reaction was cooled to RT and 3 mL of NH_4OH solution (30%) was added. A dark violet solution was obtained.

- **Ni** solution: an amount of 2.4 g of $NiCO_3$ (20 mmol) in 3.9 g of citric acid (20 mmol) and 15 mL of H_2O were refluxed for 15 min. Subsequently, the pale green solution was concentrated to a volume of 8.4 mL.

- **Fe** solution: 5.7 g of $Fe(NH_4)$citrate was dissolved in H_2O to obtain a volume of 8.4 mL.

- **Mn** solution: for the manganese-containing material, 4.5 g of $Mn(OAc)_2$ were added to 10 mL of H_2O and refluxed for 5 min. Afterwards, the solution was concentrated to 8.4 mL.

Preparation of metal oxide in γ-Al_2O_3

The carrier material γ-Al_2O_3 (pore volume: 0.84 cm^3/g) was stored at 300°C in a furnace to avoid adsorption of H_2O. Per metal salt solution (*vide supra*), 10 g of alumina were impregnated and rolled at least over night for homogenous distribution of the solution. After the impregnation procedure, the materials were all blow-dried and subsequently calcined (first step: heating rate 2°C/min to 120°C for 1 h; second step: heating rate 450°C for 2 h). 10 wt% metal per composite were obtained.

Preparation of molybdenum-containing solutions

- **Mo1** solution: $[Mo_2(OAc)_2(en)_4]\cdot(OAc)_2\cdot en$ in ethylenediamine was synthesised by a procedure of Vollhardt and co-workers.[226] 0.4 g $Mo_2(OAc)_4$ (0.87 mmol) was dissolved in 9 mL of ethylenediamine (0.13 mol) and 10.5 g of γ-Al_2O_3 was impregnated, to obtain 1.6 wt% molybdenum on alumina. Afterwards the composite was dried under vacuum at RT over night.

- **Mo2** solution: in another procedure, $[MoCp(CO)_3]_2$ was dissolved in toluene by post impregnation steps. 1 g of the dimer was added to 100 mL of dry toluene and impregnated in seven steps. 15 mL of the solution was used for every impregnation step. In between, the solvent was removed in vacuum before every single impregnation step. A red material was obtained with a loading of about 2 wt% molybdenum.

All materials were first pestled and then sieved through a 30–80 mesh sieve, to avoid diffusion limitations during further treatments.

Temperature-Programmed Reduction

Temperature-programmed reduction (TPR) experiments were performed by a Environmental Catalyst Optimising Testing Apparatus (ECOTA II) at the Shell Technology Centre, Amsterdam. A more general description is that of an atmospheric multireactor gas phase catalyst testing unit. Additionally, the unit has 8 mass flow controllers (MFC) and a valve for the carrier gas, which was argon. Hydrogen and argon were attached to the unit and dosed using the MFC. The reduction took place at 400°C for 3 h and 600°C for 5 min, and the gas flow was at 50 mL/min. Reduction gas was a mixture of H_2/Ar (23% H_2). After cooling to 40°C in an argon atmosphere, the materials were used for further experiments. All reactors were analysed by an online mass spectrometer (MS). This was done by switching between the exhaust gases from each reactor using a valve. The system was controlled by a computer with a custom program written in LabVIEW.

- Cobalt (**Co**) and nickel-containing (**Ni**) composites were reduced at 400°C (heating rate 10°C/min) in a H_2/Ar atmosphere (23% H_2/77% Ar) and held at this temperature for 3 h for complete reduction.

- Iron (**Fe**), manganese (**Mn**) and both molybdenum-containing (**Mo1, Mo2**)

materials were reduced at 600°C (heating rate 10°C/min) in a H_2/Ar atmosphere (23% H_2/77% Ar) and held at that temperature for 4 min.

4.5.5 Tetraethylsilane Treatment of Transition Metal Nanoparticles in γ-Al_2O_3

The composites obtained from Section 4.5.4 were treated with a stream of 18% $SiEt_4$/ 5% H_2/77% Ar at 400°C (heating rate 10°C/min) for 5.5 h in the same unit where the temperature-programmed reduction took place. The exhaust gas of the reactions was monitored using a mass spectrometer by switching through the different reactors. After cooling to 40°C under argon, the catalytical activity towards ethylene hydrogenation of the samples was tested. For further analyses, the samples were ground to a fine powder.

4.6 Ethylene Hydrogenation Setup

After the TPR and tetraethysilane procedure, ethylene hydrogenation experiments were performed in the same unit and all reactors were treated in the same manner. At 40°C a mixture of ethylene 4% and hydrogen 96% was used for purging with a flow of 50 mL/min. The hydrogenation experiment took 1 h, and the exhaust gas of every reactor was analysed by a mass spectrometer.

4.7 Hydrodesulphurisation Setup

Dibenzothiophene hydrodesulphurisation experiments were carried out in a stainless steel single pass nanoflow reactor, in a six-reactor unit, at medium pressure of 40 bar (Shell Technology Centre, Amsterdam). The catalyst particles to be tested were first crushed and then sieved through a 30–80 mesh sieve to avoid diffusion limitations during the test. Catalyst intake was 385.7 mg, diluted with ZrO_2 (until a bed length of 11 cm) to ensure proper hydrodynamic behaviour. Prior to testing, the catalysts were in situ presulphided with a mixture of hexadecane and 5.4 wt% of ditertiononylpentasulphide (TNPS) at a H_2 flow rate of 250 mL/g feed, at 20°C/h to 280°C for 5 h, then 20°C/h to 340°C for 2 h. The test feed was a mixture of 5 wt% dibenzothiophene, 1.75 wt%

marker paraffin C_{12} in hexadecane over a temperature range of 270°C to 350°C and the sampling period was approximately 4 h. The flow of the feed was 0.75 mL/h and the hydrogen flow was 220 mL/min. The equilibration time was about 20 h and the products were analysed by a gas-liquid chromatograph with a flame ionisation detector.

5 Appendix

Table 5.1: Crystal data and parameters pertinent to the structure determination of $Fe_2(CO)_6(SiCl_2)_3$.

Empirical formula	$C_6Cl_6Fe_2O_6Si_3$
M_r	576.73
T, K	100
Crystal size, mm^3	0.76 x 0.08 x 0.07
Crystal system	hexagonal
Space group	$P6_3/m$
a, Å	9.4141(12)
b, Å	9.4141(12)
c, Å	11.752(3)
V, $Å^3$	902.0(3)
Z	2
ρ_{calc}, g cm^{-3}	2.123
$\mu(MoK_\alpha)$, mm^{-1}	0.9
Θ range, deg	2.50–30.50
Reflections coll./unique	10,307/969
Data/ref. parameters	969/40
$R[I \geq 2\sigma(I)]$	0.013
$wR2$	0.035
GOF on F^2	1.135
Largest diff. peak/hole, e $Å^{-3}$	0.278/-0.210

Table 5.2: Crystal data and parameters pertinent to the structure determination of $[SiCl_3(HMPA)_3]^+[Fe(CO)_4SiCl_3]^-$.

Empirical formula	$C_{22}H_{54}Cl_6FeN_9O_7P_3Si_2$
M_r	974.38
T, K	100
Crystal size, mm^3	0.36 x 0.29 x 0.29
Crystal system	orthorhombic
Space group	$Pca2_1$
a, Å	29.1479(2)
b, Å	11.4569(6)
c, Å	13.5927(7)
V, Å^3	4539.2(4)
Z	4
ρ_{calc}, g cm^{-3}	1.43
μ(MoK_α), mm^{-1}	0.9
Θ range, deg	1.49–25.00
Reflections coll./unique	45844/7983
Data/ref. parameters	7983/469
$R[I \geq 2\sigma(I)]$	0.031
$wR2$	0.060
GOF on F^2	1.023
Largest diff. peak/hole, e Å^{-3}	0.298/-0.123

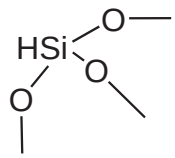

1

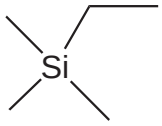

2

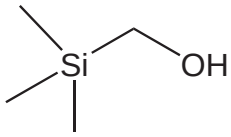

3

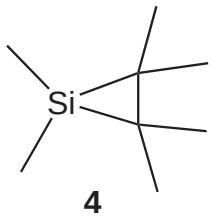

4

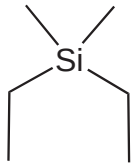

5

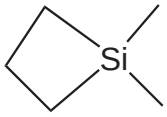

6

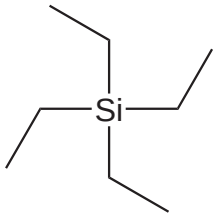

7

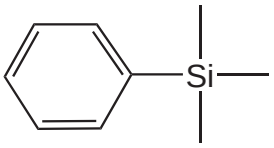

8

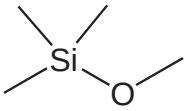

9

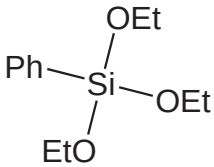

10

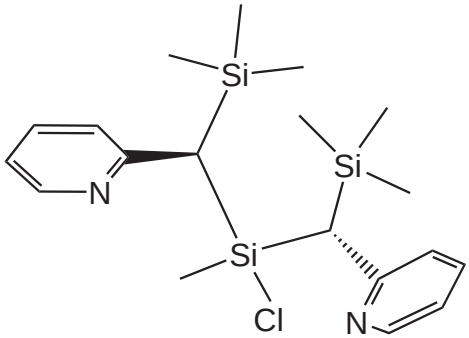

11

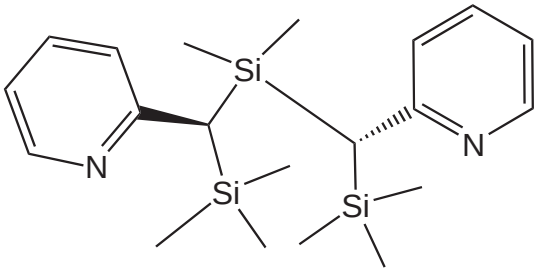

12

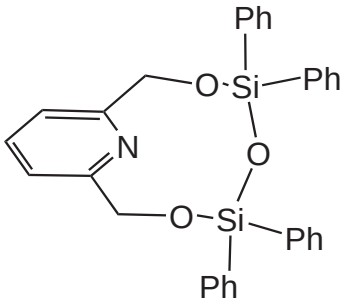

13

Figure 5.1: Structural formula of compounds **1**–**13** in Section 2.3.

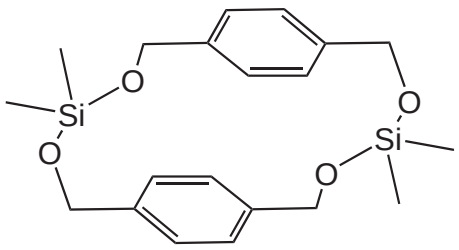

14

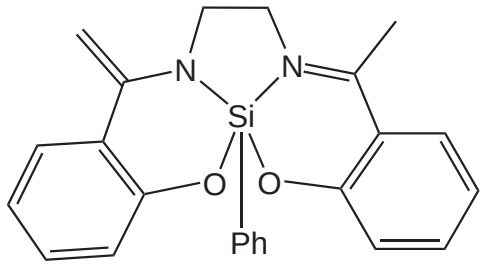

15

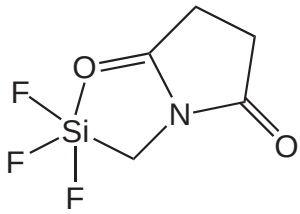

16

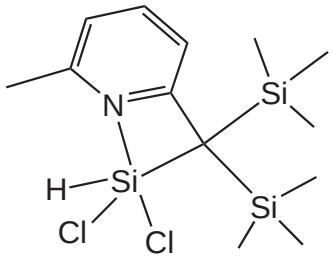

17

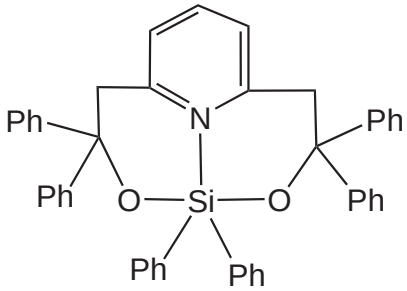

18

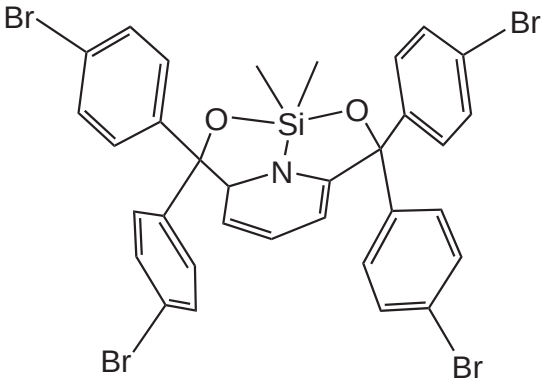

19

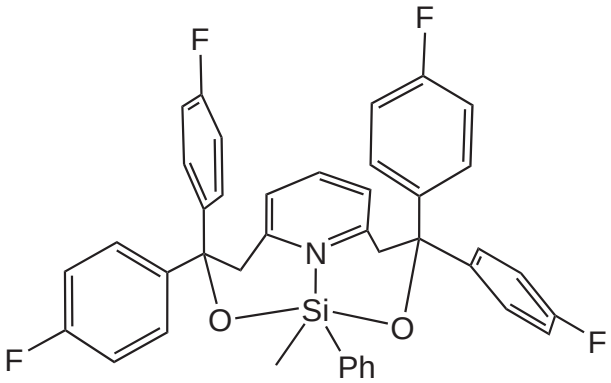

20

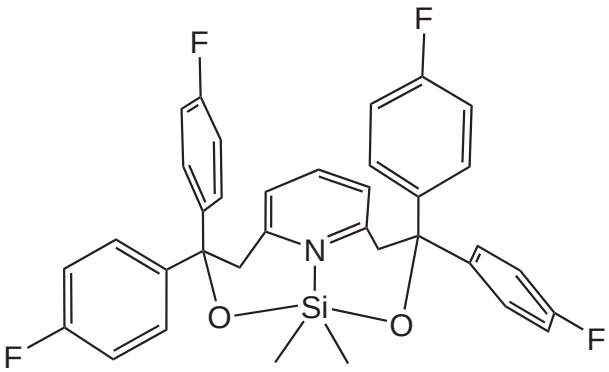

21

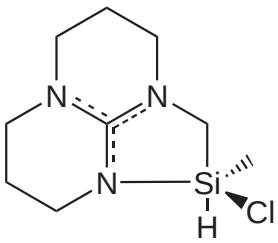

22

Figure 5.2: Structural formula of compounds **14**–**22** in Section 2.3.

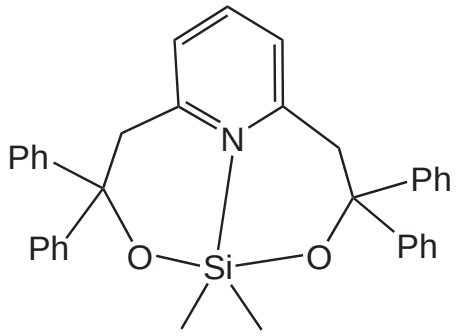

23

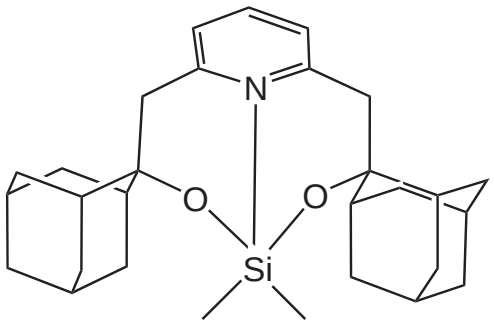

24

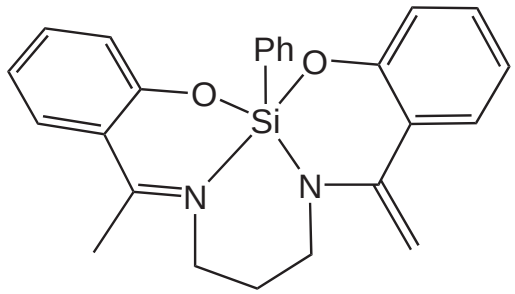

25

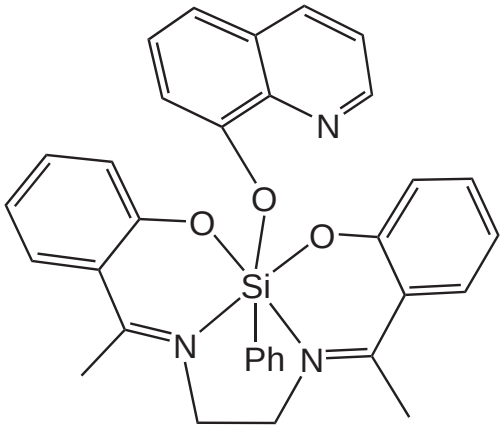

26

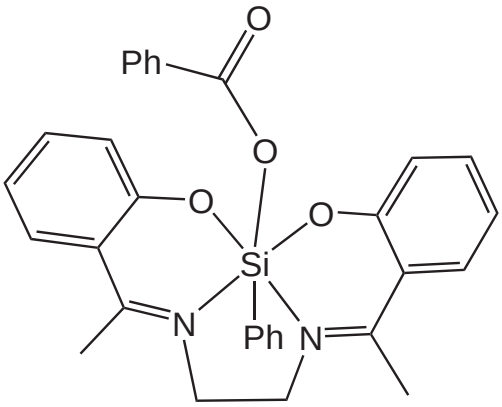

27

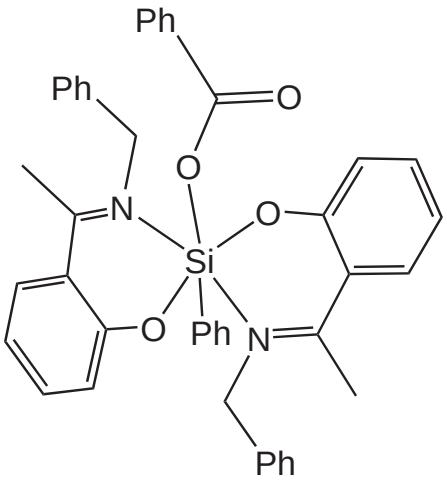

28

Figure 5.3: Structural formula of compounds **23**–**28** in Section 2.3.

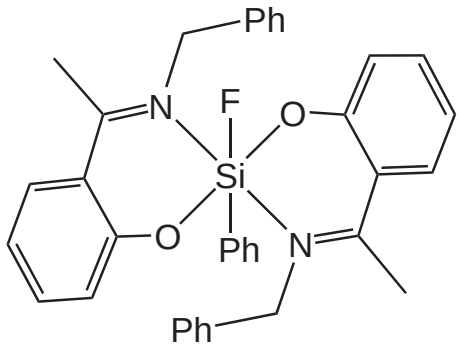

29

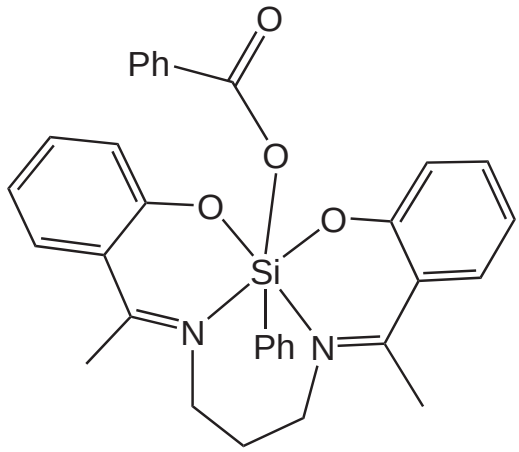

30

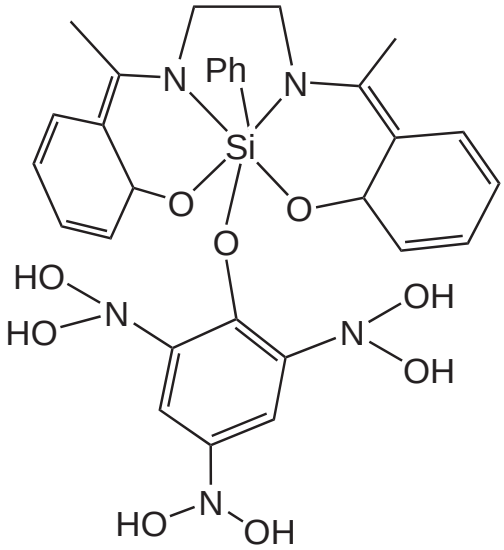

31

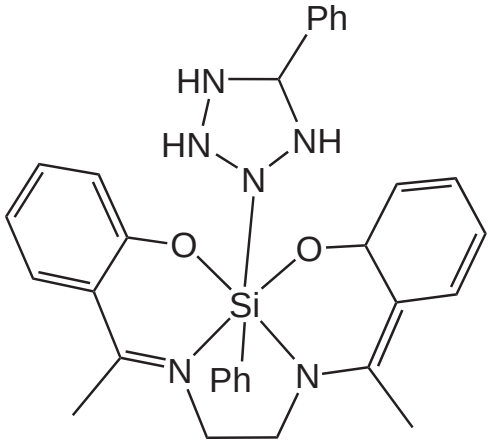

32

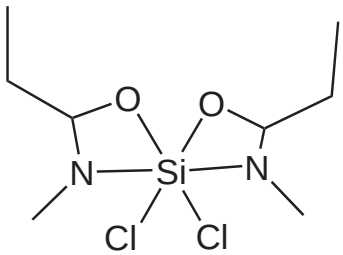

33

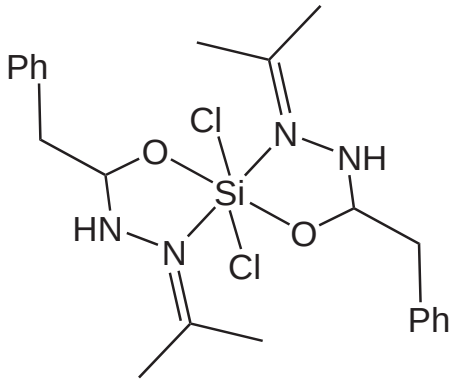

34

Figure 5.4: Structural formula of compounds **29**–**34** in Section 2.3.

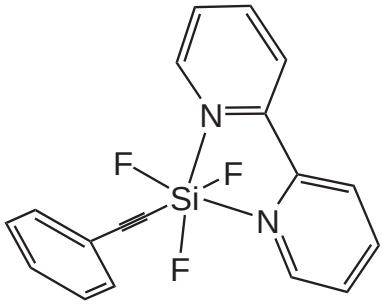

35

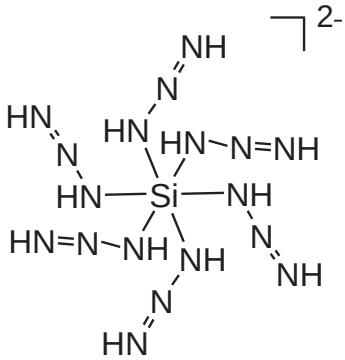

36

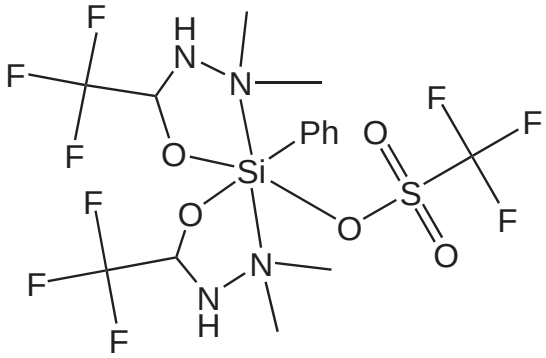

37

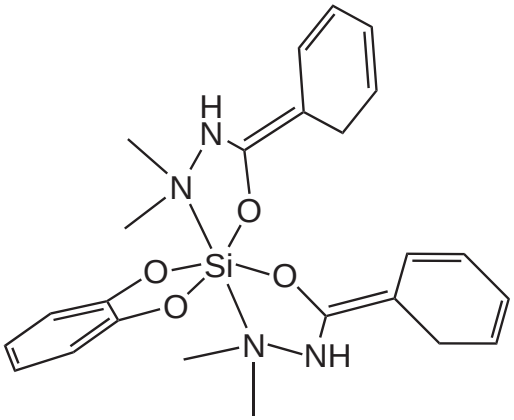

38

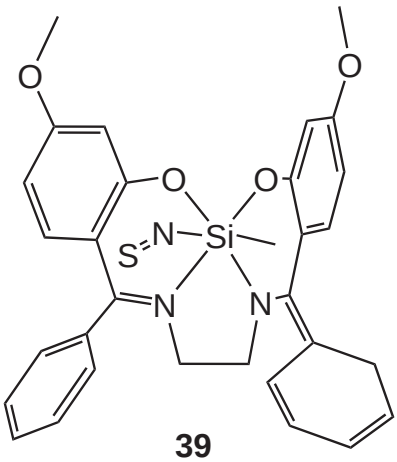

39

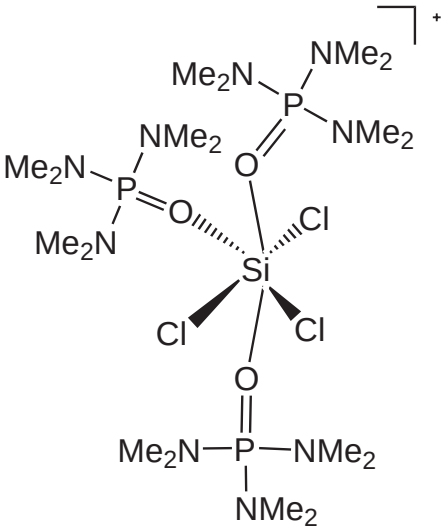

41

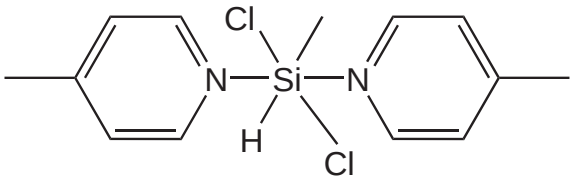

40

Figure 5.5: Structural formula of compounds **35**–**41** in Section 2.3.

Table 5.3: ^{29}Si NMR chemical shifts relative to TMS of 41 molecules and absolute isotropic shielding constants for TMS.

No	Compound Name	Exp. Shift	B3LYP			BPW91			HTCH407			Ref.
			6-31G(d,p)	LDBS	6-311 +G(2d)	6-31G(d,p)	LDBS	6-311 +G(2d)	6-31G(d,p)	LDBS	6-311 +G(2d)	
1	Trimethoxysilane	-54.9 ($CDCl_3$)	-53.0	-66.5	-72.9	-50.2	-64.9	-68.6	-55.7	-68.2	-72.1	227
2	Ethyltrimethylsilane	1.6 (10% $CDCl_3$)	5.1	6.6	2.9	5.4	3.6	3.0	4.9	2.8	4.9	228
3	Hydroxymethyltrimethylsilane	-2.5 (10% $CDCl_3$)	2.2	3.3	-1.3	1.7	-0.1	-2.0	2.2	0.1	-1.7	229
4	Hexamethylsilacyclopropane	- 49.3 ([D_8]THF)	-48.0	-53.5	-63.2	-48.9	-58.1	-63.7	-50.9	-56.3	-63.1	230
5	Diethyldimethylsilane	5.0 (10% $CDCl_3$)	7.8	8.8	3.9	7.6	5.4	3.8	7.8	4.8	3.2	228
6	1,1'-Dimethyl-silacyclobutane	18.9 (10% $CDCl_3$)	20.7	23.6	21.3	21.3	20.4	20.8	18.4	18.6	19.4	231
7	Tetraethylsilane	6.5 (10% $CDCl_3$)	14.9	14.2	8.3	14.3	10.2	8.5	14.7	8.8	7.1	228
8	Trimethylphenylsilane	-5.1 (10% $CDCl_3$)	3.2	-0.4	-5.6	3.5	-3.2	-5.3	3.3	-3.5	-5.8	232
9	Methoxytrimethylsilane	17.0 (10% $CDCl_3$)	17.5	23.3	17.1	21.0	23.3	21.2	17.1	18.4	16.5	233
10	Triethoxyphenylsilane	-55.6 ($CDCl_3$)	-53.3	-73.4	-81.0	-53.3	-72.8	-77.9	-54.4	-75.5	-80.9	234
11	Chloro-bis-[(pyridine-2-yl-trimethylsilyl)methyl]-methylsilane	22.9 (C_6D_6)	45.9	33.8	27.3	45.8	33.3	26.9	41.2	31.2	24.9	235
	Chloro-bis-[(pyridine-2-yl-trimethylsilyl)methyl]-methylsilane	1.5 (C_6D_6)	12.2, 12.5	8.2, 9.1	3.4, 5.2	13.8, 14.0	9.2, 10.1	4.5, 6.4	12.7, 12.9	9.5, 10.4	4.4, 6,4	
12	Bis-[(pyridine-2-yl-trimethylsilyl)methyl]-dimethylsilane	3.2 (C_6D_6)	19.6	11.6	07.5	18.7	11.3	7.8	17.8	11.6	8.1	235
	Bis-[(pyridine-2-yl-trimethylsilyl)methyl]-dimethylsilane	0.8 (C_6D_6)	11.3	6.0	2.9	11.2	5.9	3.1	9.9	5.9	2.7	
13	1,3-[2',6'-pyridinebis-(methyleneoxy)]-1,3-bis-(diphenyl)cyclodisiloxane	-41.6($CDCl_3$)	-13.3	-33.2	-41.0	-11.9	-30.1	-36.9	-15.0	-33.8	-40.7	236
14	1,3,10,12-tetraoxo-2,11-(dimethyl-silylene)[5.5]paracyclophane	-2.3 ($CDCl_3$)	3.7	0.02	-4.4	6.4	4.1	0.5	1.9	-1.5	-5.0	237
15	[Ethylen-N-2-hydroxyaceto-phenoniminato-N'-1-(2-hydroxyphenylato)-vinylaminato]phenylsilane	-116.1	-83.6	-111.8	-119.4	-83.5	-110.3	-115.2	-83.82	-110.9	-116.0	238
16	N-(tri-fluorosilyl-methyl)glutarimide	-75.7 (CD_2Cl_2)	-53.1	-71.9	-74.2	-46.9	-64.2	- 65.3	-52.7	-70.1	-71.1	238

Table 5.3: ^{29}Si NMR chemical shifts relative to TMS of 41 molecules and absolute isotropic shielding constants for TMS.

No	Compound Name	Exp. Shift	B3LYP			BPW91			HTCH407			Ref.
			6-31G(d,p)	LDBS	6-311 +G(2d)	6-31G(d,p)	LDBS	6-311 +G(2d)	6-31G(d,p)	LDBS	6-311 +G(2d)	
17	Dichloro-[(6-methylpyridin-2-yl)bis(trimethylsilyl))methyl]-silane	-64.8 (C_6D_6)	-7.55	-31.6	-37.9	-7.6	-32.3,	-37.7	-12.3	-32.0	-37.9	235
	Dichloro-[(6-methylpyridin-2-yl)bis(trimethylsilyl))methyl]-silane	1.9 (C_6D_6)	15.3, 13.7	8.3, 5.9	5.5, 3.0	14.8, 12.9	7.9, 5,3	5.4, 2.7	13.9, 11.0	8.1, 5.6	5.4, 2.5	
18	2,6-pyridinebis(1,1-diphenylethoxy)-diphenylsilane	-61.9 ($CDCl_3$)	-28.7	-56.2	-63.5	-28.9	-54.6	-60.8	-32.8	-56.9	-63.1	236
19	2,6-pyridinebis(1,1-di-p-bromo-phenylmethoxy)di-methylsilane	-56.5 ($CDCl_3$)	-36.1	-47.9	-54.0	-32.1	-41.9	-46.9	-34.6	-44.8	-50.4	237
20	3,3,7,7-Tetrakis-(4-fluorophenyl)-5-methyl-5-phenyl-4,6-dioxa-13-aza-5-sila-bicyclo-[7.3.1]trideca-1(12),9(13),10-triene	-48.9 ($CDCl_3$)	-26.9	-44.0	-50.5	-26.5	-42.1	-47.5	-30.8	-45.0	-50.8	239
21	3,3,7,7-Tetrakis-(4-fluorophenyl)-5,5-dimethy-4,6-dioxa-13-aza-5-sila-bicyclo[7.3.1]trideca-1(12),9(13),10-triene	-31.7 ($CDCl_3$)	-12.9	-22.0	-27.6	-11.2	-19.0	-23.8	-16.0	-23.5	-28.2	239
22	Chloro-dimethyl-(3,4,7,8-tetrahydro-2H,6H-pyrimido[1,2-a]pyrimidin-1-ylmethyl-C1, N9)-silicium	-49.1 (C_6D_6)	-51.6	-63.1	-67.5	-52.3	-62.4	-66.5	-51.2	-60.5	-64.3	240
23	2,6-Pyridinebis(1,1-diphenylethoxy)dimethylsilane	-31.4 ($CDCl_3$)	-14.5	-23.7	-29.1	-12.8	-20.6	-25.2	-17.4	-29.7	-25.1	241
24	2,6-di(2-oxy(2-adamantylidine))-ethylpyridine-dimethylsilicon	-41.9 ($CDCl_3$)	-21.9	-32.4	-38.5	-21.2	-30.2	-35.6	-25.8	-34.0	-39.4	242
25	[Trimethylen-N-2-oxy-acetophenoneiminato-N'-1-(2-oxyphenylato)vinylaminato]-phenylsilane	-107.7 ($CDCl_3$)	-67.0	-94.5	-103.0	-67.2	-93.2	-99.9	-69.0	-94.7	-101.4	243
26	Ethylene-N,N'-bis(2-oxy-acetophenoneiminato)-8-oxyquinolinato phenylsilane	-181.3 ($CDCl_3$)	-135.9	-189.2	-192.0	-142.3	-180.5	-185.3	-140.3	-178.2	-183.5	243
27	Benzoato-[ethylene-N,N'-bis(2-oxyaceto-phenoneiminato)] phenylsilane	-186.0	-149.8	-187.9	-196.1	-149.1	-185.1	-190.0	-144.9	-182.4	-188.3	243

Table 5.3: ^{29}Si NMR chemical shifts relative to TMS of 41 molecules and absolute isotropic shielding constants for TMS.

No	Compound Name	Exp. Shift	B3LYP			BPW91			HTCH407			Ref.
			6-31G(d,p)	LDBS	6-311 +G(2d)	6-31G(d,p)	LDBS	6-311 +G(2d)	6-31G(d,p)	LDBS	6-311 +G(2d)	
28	Benzoato-bis-(N-benzyl-2-oxyaceto-phenoneiminato)-phenylsilicon	-183.4 ($CDCl_3$)	-145.3	-184.7	-192.3	-143.7	-185.8	-181.6	-141.9	-178.9	-184.0	243
29	Fluoro-bis-(N-benzyl-2-oxyacetophenoneiminato)-phenylsilicon	-180.9 ($CDCl_3$)	-143.5	-180.6	-188.2	-140.9	-177.4	-180.6	-139.6	-175.8	-179.8	243
30	Benzoato-[trimethylene-N,N'-bis(2-oxyacetophenone-iminato)]phenylsilane	-184.2 ($CDCl_3$)	- 147.5	-186.2	-189.5	-146.7	-181.7	-183.2	-143.7	-178.8	-181.5	243
31	[Ethylene-N,N'-bis(2-oxy-acetophenoneiminato)]2,4,6-trinitrophenolatophenylsilane	-172	-138.7	-175.5	-181.5	-135.8	-171.7	-173.3	-134.8	-170.0	-173.2	243
32	[Ethylene-N,N'-bis(2-oxyaceto-phenoneiminato)]-2-(5-phenyl-tetrazolido)(phenyl)silicon	-175.6 ([D_6]DMSO)	-143.9	-184.2	-188.7	-143.7	-181.7	-182.6	-140.9	-179.0	-181.2	243
33	Dichloro-bis(N-methylpropionamido)-silicon	-159.9	-123.4	-157.1	-162.9	-121.2	-151.8	-157.0	-119.5	-150.3	-155.5	244
34	Dichloro-bis(N-(iso-propylideneimino)phenyl-acetimidato-N,O)silicon	-163.7 ($CDCl_3$)	-114.6	-150.9	-157.1	-110.0	-143.8	-149.3	-110.9	-142.1	-147.3	245
35	(2,2'-Bipyridyl)-trifluoro-(phenylethynyl)silane	-178.7 ($CDCl_3$)	-131.4	-171.4	-174.7	-126.2	-162.7	-164.9	-124.7	-162.9	-165.5	246
36	Hexakis(azido)-silicate	-188.7 (CD_3CN)	-161.5	-201.4	-206.1	-160.6	-195.1	-199.5	-157.3	-192.3	-197.8	247
37	Bis(N-(Dimethylamino)-trifluoroacetimidato-N,O)-phenyl-(trifluoromethane-sulfonato)-silicon	-140.6 (CD_2Cl_2)	-100.6	-138.7	-142.1	-96.8	-130.8	-138.1	-96.0	-129.5	-132.8	248
38	Bis(N-(Dimethylamino)-benzimidato-N,O)-(catecholato-O,O)-silicon	-141 ([D_8]toluene)	-101.1	-138.0	-143.3	-95.6	-128.7	-132.8	-95.8	-128.9	-133.2	249
39	[Si(salen*)Me(NCS)]	-170.8 ($CDCl_3$)	-154.6	-188.9	-193.9	-154.1	-184.1	-188.3	-149.9	-181.1	-185.4	250
40	Bis-(4-methylpyridine)methyl-hydridodichlorosilane	-135.6	-96.2	-129.2	-135.9	-93.6	-125.9	-131.8	-95.2	-121.6	-127.3	251
41	Trichloro-tris(hexamethyl-phosphoric-triamide)silicon	-205.8 ([D_8]toluene)	-129.6	-179.5	-184.8	-126.4	-172.9	-177.2	-129.2	-171.2	-176.5	72
	Tetramethylsilane	0	412.7	331.9	327.0	403.2	329.8	325.6	402.2	342.0	337.7	

References

[1] Siegel, R. W. *Nanostructured Materials* **1993**, *3*, 1–18.

[2] Feynman, R. P. *Engineering and Science* **1960**, *23*, 22–36.

[3] Berger, P.; Adelman, N. B.; Beckman, K. J.; Campbell, D. J.; Ellis, A. B.; Lisensky, G. C. *Journal of Chemical Education* **1999**, *76*, 943–948.

[4] Leslie-Pelecky, D. L.; Rieke, R. D. *Chemistry of Materials* **1996**, *4756*, 1770–1783.

[5] Gleiter, H. *Progress in Materials Science* **1989**, *33*, 223–315.

[6] Gryaznov, V.; Trusov, L. *Progress in Materials Science* **1993**, *37*, 28–401.

[7] Getzlaff, M. *Fundamentals of Magnetism, 1st ed.*; Springer, 2008.

[8] Bedanta, S.; Kleemann, W. *Journal of Physics D: Applied Physics* **2009**, *42*, 1–28.

[9] Néel, L. *Annales Geophysicae* **1949**, *5*, 99–136.

[10] Brown, W. F. *Physical Review* **1963**, *130*, 1677–1686.

[11] Wernsdorfer, W.; Orozco, E. B.; Hasselbach, K.; Benoit, A.; Barbara, B.; Demoncy, N.; Loiseau, A.; Pascard, H.; Mailly, D. *Physical Review Letters* **1997**, *78*, 1791–1794.

[12] Moser, A.; Takano, K.; Margulies, D. T.; Albrecht, M.; Sonobe, Y.; Ikeda, Y.; Sun, S.; Fullerton, E. E. *Journal of Physics D: Applied Physics* **2002**, *35*, R157.

[13] Shull, R. *IEEE Transactions on Magnetics* **1993**, *29*, 2614 –2615.

[14] Pankhurst, Q. A.; Connolly, J.; Jones, S. K.; Dobson, J. *Journal of Physics D: Applied Physics* **2003**, *36*, R167.

[15] Rijkeboer, R. *Catalysis Today* **1991**, *11*, 141–150.

[16] J. G. Calvert, R. F. S., J. B. Heywood; Seinfeld, J. J. *Science* **1991**, *261*, 37–45.

[17] Bell, A. T. *Science* **2003**, *299*, 1688–1691.

[18] Kolel-Veetil, M. K.; Keller, T. M. *Materials* **2010**, *3*, 1049–1088.

[19] Brandes, E. A. *Smithells Metal Reference Book, 6st ed.*; Butterworths & Co, 1983.

[20] Kulatov, E.; Nakayama, H.; Ohta, H. *Journal of the Physical Society of Japan* **2001**, *70*, 2199–2204.

[21] Aeppli, G.; Fisk, Z. *Comments on Condensed Matter Physics* **1992**, *16*, 155–170.

[22] Leong, D.; Harry, M.; Reeson, K. J.; Homewood, K. P. *Nature* **1997**, *387*, 686–688.

[23] Filonov, A. B.; Migas, D. B.; Shaposhnikov, V. L.; N.Dorozhkin, N.; Petrov, G. V.; Borisenko, V. E.; Henrion, W.; Lange, H. J. *Journal of Applied Physics* **1996**, *79*, 7708–7712.

[24] Sawatzky, E. *IEEE Transactions on Magnetics* **1971**, *7*, 374–376.

[25] Liou, S. H.; Malhotra, S. S.; Shen, J. X.; Hong, M.; Kwo, J.; Chen, H. S.; Mannaerts, J. P. *Applied Physics Letters* **1993**, *73*, 6766–6769.

[26] Hines, W. A.; Menotti, A. H.; Budnick, J. I.; Burck, T. J.; Lirenta, T.; Niculescu, V.; Raj, K. *Physical Review B* **1976**, *13*, 4060–4069.

[27] Rouff, R. S.; Lorents, D.; Chan, B.; Malhotra, R.; Subramoney, S. *Science* **1993**, *259*, 346–348.

[28] Shinjo, T.; Nakamura, Y.; Shikazono, N. *Journal of the Physical Society of Japan* **1963**, *18*, 797–801.

[29] Schütte, M.; Wartchow, R.; Binnewies, M. *Zeitschrift für Anorganische Allgemeine Chemie* **2003**, *629*, 1846–1850.

[30] Ishida, K.; Nishizawa, T.; Schlesinger, M. *Journal of Phase Equilibria* **1991**, *12*, 578–586.

[31] Boscherini, F.; Joyce, J. J.; Ruckman, M. W.; Weaver, J. H. *Physical Review B* **1987**, *35*, 4216–4220.

[32] Lee, J. D.; Jin, S. H.; Shim, B. C.; Park, B. G. *IEEE Electron Device Letters* **2001**, *22*, 173 –175.

[33] Zhao, Q. T.; Klinkhammer, F.; Dolle, M.; Kappius, L.; Mantl, S. *Applied Physics Letters* **1999**, *74*, 454–456.

[34] Haynes, W. M. *CRC Handbook of Chemistry and Physics, 88th ed.*; CRC Press, 2007.

[35] Bormio-Nunesa, C.; Angelo Nunesa, C.; Coelhob, A. A.; Ismênia Sodero Toledo Faria, M.; Suzuki, P. A.; Carvalho Coelho, G. *Journal of Alloys and Compounds* **2010**, *508*, 5–8.

[36] Barrett, C.; Massalski, T. B. *Structure of Metals 3rd revised ed.: Crystallographic Methods, Principles, and Data*; Pergamon Press, 1987.

[37] Seo, K.; Varadwaj, K. S. K.; Mohanty, P.; Lee, S.; Jo, Y.; Jung, M. H.; Kim, J.; Kim, B. *Nano Letters* **2007**, *7*, 1240–1245.

[38] Liang, C.; Zhao, A.; Zhang, X.; Ma, Z.; Prins, R. *Chemical Communications* **2009**, 2047–2049.

[39] Du, V. A.; Gross, S.; Schubert, U. *Chemical Communications* **2010**, *46*, 8549–8551.

[40] Okamoto, H. *Journal of Phase Equilibria* **1991**, *12*, 505–507.

[41] Jorgensen, J. E.; Rasmussen, S. E. *Powder Diffraction* **1991**, *6*, 194–195.

[42] Rado, G. T.; Suhl, H. *Magnetism, A Treatise on Modern Theory and Materials*; Academic Press, New York, 1963.

[43] Aharoni, A. *Introduction to the Theory of Ferromagnetism*; Oxford University Press, Oxford, 1996.

[44] Stoner, E. C. *Proceedings of the Royal Society A* **1938**, *165*, 372–414.

[45] Moriya, T. *Spin Fluctuations in Itinerant Electron Magnetism*; Springer Series, Berlin, 1985.

[46] Pfleiderer, C.; Reznik, D.; Pintschovius, L.; von Lohneysen, H.; Garst, M.; Rosch, A. *Nature* **2004**, *427*, 227–231.

[47] Gajdzik, M.; Sürgers, C.; Kelemen, C.; van Löhneysen, H. *Journal of Applied Physics* **2000**, *87*, 6013–6015.

[48] Karpinskii, O. G.; Evseev, B. A. *Khimicheskaya Svyaz Poluprovodn* **1969**, 267–272.

[49] Schwomma, O.; Preisinger, A.; Nowotny, H.; Wittmann, A. *Monatshefte für Chemie - Chemical Monthly* **1964**, *95*, 1527–1537.

[50] Flieher, G.; Voellenkle, H.; Nowotny, H. *Monatshefte für Chemie - Chemical Monthly* **1967**, *98*, 2173–2179.

[51] Zwilling, G.; Nowotny, H. *Monatshefte für Chemie - Chemical Monthly* **1973**, *104*, 668–675.

[52] Borders, J. S.; Picraux, S. I. *Proceedings of the IEEE* **1974**, *62*, 1224–1231.

[53] Wu, Y.; Xiang, J.; Yang, C.; Lu, W.; Lieber, C. M. *Nature* **2004**, *430*, 61–65.

[54] Yan, X. Q.; Yuan, H. J.; Wang, J. X.; Liu, D. F.; Zhou, Z. P.; Gao, Y.; Song, L.; Liu, L. F.; Zhou, W. Y.; Wang, G.; Xie, S. S. *Applied Physics A* **2004**, *79*, 1853–1856.

[55] Kim, J.; Anderson, W. A. *Thin Solid Films* **2005**, *483*, 60–65.

[56] Kim, C. J.; Kang, K.; Woo, Y. S.; Ryu, K. G.; Moon, H.; Kim, J. M.; Zang, D. S.; Jo, M. H. *Advanced Materials* **2007**, *19*, 3627–3642.

[57] Kang, K.; Kim, S. K.; Kim, C. J.; Jo, M. H. *Nano Letters* **2008**, *8*, 431–436.

[58] Liu, Z.; Zhang, H.; Wang, L.; Yang, D. *Nanotechnology* **2008**, *19*, 375602.

[59] Kim, J.; Shin, D. H.; Lee, E. S.; Han, C. S.; Park, Y. C. *Applied Physics Letters* **2007**, *90*, 253103.

[60] Lee, C. Y.; Lu, M. P.; Liao, K. F.; Wu, W. W.; Chen, L. J. *Applied Physics Letters* **2008**, *93*, 113109.

[61] Kim, J.; Lee, E. S.; Han, C. S.; Kang, Y.; Kim, D.; Anderson, W. A. *Microelectronic Engineering* **2008**, *85*, 1709–1712.

[62] Chen, X.; Zhao, A.; Shao, Z.; Li, C.; Williams, C. T.; Liang, C. *Journal of Physical Chemistry C* **2010**, *114*, 16525–16533.

[63] Ouyang, L.; Thrall, E. S.; Deshmukh, M. M.; Park, H. *Advanced Materials* **2006**, *18*, 1437–1440.

[64] Varadwaj, K. S. K.; Seo, K.; In, J.; Mohanty, P.; Park, J.; Kim, B. *Journal of the American Chemical Society* **2007**, *129*, 8594–8599.

[65] Seo, K.; Varadwaj, K. S. K.; Cha, D.; In, J.; Kim, J.; Park, J.; Kim, B. *Journal of Physical Chemistry C* **2007**, *11*, 9072–9076.

[66] Schmitt, A. L.; Higgins, J. M.; Szczech, J. R.; Jin, S. *Journal of Materials Chemistry* **2010**, *20*, 223–235.

[67] Zybill, C. E.; Huang, W. *Inorganica Chimica Acta* **1999**, *291*, 380–387.

[68] Novak, I.; Huang, W.; Luo, L.; Huang, H. H.; Ang, H.; Zybill, C. E. *Organometallics* **1997**, *16*, 1567–1572.

[69] Schmitt, A. L.; Bierman, M. J.; Schmeisser, D.; Himpsel, F. J.; Jin, S. *Nano Letters* **2006**, *6*, 1617–1621.

[70] Schmitt, A. L.; Zhu, L.; Schmeisser, D.; Himpsel, F. J.; Jin, S. *The Journal of Physical Chemistry B* **2006**, *110*, 18142–18146.

[71] Prokop, J. *Thin Solid Films* **2000**, *359*, 39–45.

[72] Du, V. A.; Baumann, S. O.; Stipicic, G. N.; Schubert, U. *Zeitschrift für Naturforschung B - A Journal of Chemical Sciences* **2009**, *3*, 1553–1557.

[73] Du, V. A.; Stipicic, G. N.; Bendová, M.; Schubert, U. *Monatshefte für Chemie - Chemical Monthly* **2010**, *6*, 671–675.

[74] Higgins, J. M.; Schmitt, A. L.; Guzei, L. A.; Jin, S. *Journal of the American Chemical Society* **2008**, *130*, 16086–16094.

[75] Pearson, W. B. *Acta Crystallographica Section B* **1970**, *26*, 1044–1046.

[76] Nowotny, H. *Crystal Chemistry of Transition Metal Defect Silicides and Related Compounds, in Chemistry of Extended Defects in Non-Metallic Solids*; North-Holland Publishing Company, Amsterdam, 1970.

[77] Zhou, S.; Liu, X.; Lin, Y.; Wang, D. *Angewandte Chemie, International Edition* **2008**, *47*, 7681–7684.

[78] Dahal, N.; Chikan, V. *Chemistry of Materials* **2010**, *22*, 2892–2897.

[79] Bourg, S.; Boury, B.; Corriu, R. J. P. *Journal of Materials Chemistry* **1998**, *8*, 1001–1006.

[80] Aylett, B. J.; Colquhoun, H. M. *Journal of the Chemical Society, Dalton Transactions* **1977**, 2058–2061.

[81] Corriu, R. J. P.; Moreau, J. J. E.; Praet, H. *Organometallics* **1989**, *8*, 2779–2786.

[82] Corriu, R. J. P.; Gerbier, P.; Guerin, C.; Henner, B. J. L.; Jean, A.; Mutin, P. H. *Organometallics* **1992**, *11*, 2507–2513.

[83] Corriu, R. J. P.; Devylder, N.; Guerin, C.; Henner, B.; Jean, A. *Organometallics* **1994**, *13*, 3194–3202.

[84] Corriu, R. J. P.; Devylder, N.; Guerin, C.; Henner, B.; Jean, A. *Journal of Organometallic Chemistry* **1996**, *509*, 249–257.

[85] Friebe, L.; Liu, K.; Obermeier, B.; Petrov, S.; Dube, P.; Manners, I. *Chemistry of Materials* **2007**, *19*, 2630–2640.

[86] Kolel-Veetil, M. K.; Qadri, S. B.; Osofsky, M.; Goswami, R.; Keller, T. M. *The Journal of Physical Chemistry C* **2009**, *113*, 14663–14671.

[87] Foucher, D. A.; Tang, B. Z.; Manners, I. *Journal of the American Chemical Society* **1992**, *114*, 6246–6248.

[88] Petersen, R.; Foucher, D. A.; Tang, B. Z.; Lough, A.; Raju, N. P.; Greedan, J. E.; Manners, I. *Chemistry of Materials* **1995**, *7*, 2045–2053.

[89] MacLachlan, M. J.; Ginzburg, M.; Coombs, N.; Coyle, T. W.; Raji, N. P.; Greedan, J. E.; Ozin, G. A.; Manners, I. *Science* **2000**, *287*, 1460–1463.

[90] Sun, Q.; Lam, J. W. Y.; Xu, K.; Xu, H.; Cha, J. A. K.; Wong., P. C. L.; Wen, G.; Zhang, X.; Jing, X.; Wang, F.; Tang, B. Z. *Chemistry of Materials* **2000**, *12*, 2617–2624.

[91] Ginzburg, M.; MacLachlan, M. J.; Yang, S. M.; Coombs, N.; Coyle, T. W.; Raju, N. P.; Greedan, J. E.; Herber, R. H.; Ozin, G. A.; Manners, I. *Journal of the American Chemical Society* **2002**, *124*, 2625–2639.

[92] Bühl, M.; Kaupp, M.; Malkina, O. L.; Malkin, V. G. *Journal of Computational Chemistry* **1999**, *20*, 91–105.

[93] Facelli, J. C. *In Modern Magnetic Resonance*; Springer Netherlands, 2006.

[94] Ramsey, N. F. *Physical Review* **1950**, *78*, 699–703.

[95] Wolinski, K.; Hinton, J. F.; Pulay, P. *Journal of the American Chemical Society* **1990**, *112*, 8251–8260.

[96] Schreckenbach, G.; Ziegler, T. *Journal of Physical Chemistry* **1995**, *99*, 606–611.

[97] Rauhut, G.; Puyear, S.; Wolinski, K.; Pulay, P. *Journal of Physical Chemistry* **1996**, *100*, 6310–6316.

[98] Kaupp, M.; Malkin, V. G.; Malkina, O. L. *Encyclopedia of Computational Chemistry*; Wiley, New York, 1998.

[99] Kaupp, M.; Malkina, O. L.; Malkin, V. G. *The Journal of Chemical Physics* **1997**, *106*, 9201–9212.

[100] Heine, T.; Goursot, A.; Seifert, G.; Weber, J. *The Journal of Physical Chemistry A* **2001**, *105*, 620–626.

[101] Corminbœuf, C.; Heine, T.; Weber, J. *Chemical Physics Letters* **2002**, *357*, 1–7.

[102] Sefcik, J.; Goddard, W. A. *Geochimica et Cosmochimica Acta* **2001**, *65*, 4435–4443.

[103] Casserly, T. B.; Gleason, K. K. *Journal of Physical Chemistry B* **2005**, *109*, 13605–13610.

[104] Karni, M.; Apeloig, Y.; Takagi, N.; Nagase, S. *Organometallics* **2005**, *24*, 6319–6330.

[105] Boese, A. D.; Handy, N. C. *The Journal of Chemical Physics* **2001**, *114*, 5497–5503.

[106] Gauss, J. *Chemical Physics Letters* **1992**, *191*, 614–620.

[107] Ambati, J.; Rankin, S. E. *The Journal of Physical Chemistry A* **2010**, *114*, 5279–5286.

[108] Holmes, R. R. *Chemical Reviews* **1996**, *96*, 927–950.

[109] Voronkov, M. G.; Trofimova, O. M.; Bolgova, Y. I.; Chernov, N. F. *Russian Chemical Reviews* **2007**, *76*, 825–845.

[110] Kost, D.; Kalikhman, I. *Accounts of Chemical Research* **2009**, *42*, 303–314.

[111] Gary, J. H.; Handwerk, G. E. *Petroleum Refining Technology and Economics, 2nd ed.*; Marcel Dekker, 1984.

[112] Speight, J. G. *The Chemistry and Technology of Petroleum*; Marcel Dekker, 1999.

[113] International Diesel Rankings - Top 100 Sulphur. http://www.ifqc.org/NM_Top5.aspx.

[114] Oil & Gas Industry Overview. http://www.ontime.methanetomarkets.org/m2mtool/index.html.

[115] Startsev, A. N. *Catalysis Reviews, Science and Engineering* **1995**, *37*, 353–423.

[116] Topsøe, H.; Clausen, B. S.; Masoth, F. E. *Catalysis Science and Technology, Vol. 11*; Springer, 1996.

[117] Whitehurst, D. D.; Isoda, T.; Mochida, I. *Advances in Catalysis* **1998**, *42*, 345–471.

[118] Shafi, R.; Hutchings, G. J. *Catalysis Today* **2000**, *59*, 423–442.

[119] Landau, M. V. *Catalysis Today* **1997**, *36*, 393–429.

[120] Sánchez-Delgado, R. A. *Organometallic Modeling of the Hydrodesulfurization and Hydrodenitrogenation Reactions*; Springer Netherlands, 2002.

[121] Weber, T.; Prins, R.; van Santen, R. A. *Transitional Metal Sulphides - Chemistry and Catalysis*; Dordrecht; Kluwer Academic Publishers, 1998.

[122] Rothenberg, G. *Catalysis: Concepts and Green Applications.*; Wiley, 2008.

[123] Pecoraro, T. A.; Chianelli, R. R. *Journal of Catalysis* **1981**, *67*, 430–445.

[124] Kasztelan, S. *Hydrotreating Technology for Pollution Control, Catalysts, Catalysis and Process, Chemical Industries*; Marcel Dekker, 1996.

[125] Tschan, R.; Schubert, M. M.; Baiker, A.; Bonrath, W.; Lansink-Rotgerink, H. *Catalysis Letters* **2001**, *75*, 31–36.

[126] Tschan, R.; Wandeler, R.; Schneider, M. S.; Schubert, M. M.; Baiker, A. *Journal of Catalysis* **2001**, *204*, 219–229.

[127] Tschan, R.; Wandeler, R.; Schneider, M. S.; Burgener, M.; Schubert, M. M.; Baiker, A. *Applied Catalysis* **2002**, *223*, 173–185.

[128] Wessel, T. J.; Rethwiseh, D. G. *Reaction Kinetics and Catalysis Letters* **1996**, *58*, 7–12.

[129] Simons, R. S.; Tessier, C. A. *Acta Crystallographica Section C* **1995**, *51*, 1997–1998.

[130] Schmid, G.; Welz, E. *Zeitschrift für Naturforschung B - A Journal of Chemical Sciences* **1979**, *34B*, 929–933.

[131] Cotton, F. A.; Troup, J. M. *Journal of the Chemical Society, Dalton Transactions* **1974**, 800–802.

[132] Scott, A. P.; Radom, L. *Journal of Physical Chemistry* **1996**, 16502–16513.

[133] Pomeroy, R. K.; Wijesekera, K. S. *Inorganic Chemistry* **1980**, *19*, 3729–3735.

[134] Straßer, C.; Knorr, M.; Schubert, U. *Journal of Organometallic Chemistry* **1991**, *411*, 75–87.

[135] Bottoni, A. *The Journal of Physical Chemistry A* **1998**, *102*, 10142–10150.

[136] Harvey, N. J. *Spin-Forbidden Reactions in Transition Metal Chemistry*; Marcel Dekker, New York, 2001.

[137] Denmark, S. E.; Eklov, B. M. *Chemistry - A European Journal* **2008**, *14*, 234–239.

[138] Bauschlicher, B. W.; Partridge, H. *Journal of Chemical Physics* **1995**, *103*, 1788–1791.

[139] Hartmann, F.; Dahelms, T.; Mootz, D. *Zeitschrift für Kristallographie* **1998**, *213*, 639–640.

[140] Garcia-Escomel, C.; Mekarbane, P.; Martin, C.; Grenouillet, P.; de Bellefon, C. *Inorganica Chimica Acta* **2003**, *350*, 407–413.

[141] Schmitt, A. L.; Zhu, L.; Schmeisser, D.; Himpsel, F. J.; Jin, S. *The Journal of Physical Chemistry B* **2006**, *110*, 18142–18146.

[142] Brouwer, D. H.; Moudrakovski, I. L.; Darton, R. J.; Morris, R. E. *Magnetic Resonance in Chemistry : MRC* **2010**, *48*, 113–121.

[143] Forsyth, A. B., David A.and Sebag *Journal of the American Chemical Society* **1997**, *119*, 9483–9494.

[144] Alkorta, I.; Elguero, J. *Structural Chemistry* **1998**, *9*, 187–202.

[145] Ruden, T. A.; Ruud, K. *Calculations of NMR and EPR Parameters. Theory and Applications*; Wiley, Weinheim, 2004.

[146] Cancés, M. T.; Mennucci, B.; Tomasi, J. *Journal of Chemical Physics* **1997**, *107*, 3032–3037.

[147] Cossi, M.; Barone, V.; Mennucci, B.; Tomasi, J. *Chemical Physics Letters* **1998**, *286*, 253–260.

[148] Mennucci, B.; J.Tomasi, *Journal of Chemical Physics* **1997**, *106*, 5151–5158.

[149] Wu, Y.; Xiang, J.; Yang, C.; Lu, W.; Lieber, C. M. *Nature* **2004**, *430*, 61–65.

[150] Zhao, A.; Zhang, X.; Chen, X.; Guan, J.; Liang, C. *The Journal of Physical Chemistry C* **2010**, *114*, 3962–3967.

[151] Wagner, C. D. *Analytical Chemistry* **1972**, *44*, 967–973.

[152] Moulder, J. F.; Stickle, W. F.; Sobol, P. E.; Bomben, K. D. *Handbook of X-Ray Photoelectron Spectroscopy*; Perkin Elmer Corp., Eden Prairie, MN, 1992.

[153] Briggs, D.; Seah, M. P. *Practical Surface Analysis, 2nd ed.*; Wiley, New York, 1990.

[154] Chuang, T.; Brundle, C.; Rice, D. *Surface Science* **1976**, *59*, 413–429.

[155] Armelao,; Barreca, D.; Gross, S.; Martucci, A.; Tieto, E.; Tondello, E. *Journal of Non-Crystalline Solids* **2001**, *477*, 293–295.

[156] Ming, H.; Baker, B. G. *Applied Catalysis A: General* **1995**, *123*, 23–36.

[157] Velu, S.; Suzuki, K.; Gopinath, C. S. *The Journal of Physical Chemistry B* **2002**, *106*, 12737–12746.

[158] Mathew, T.; Shiju, N. R.; Sreekumar, K.; Rao, B. S.; Gopinath, C. S. *Journal of Catalysis* **2002**, *210*, 405–417.

[159] Yamauchi, Y.; Yoshitake, M. *Journal of Surface Analysis* **2002**, *432*, 432–435.

[160] Murarka, S. P.; Vaidya, S. *Journal of Applied Physics* **1984**, *56*, 3404–3412.

[161] Breitscheidel, B.; Zieder, J.; Schubert, U. *Chemistry of Materials* **1991**, *3*, 559–566.

[162] Trimmel, G.; Schubert, U. *Journal of Non-Crystalline Solids* **2001**, *296*, 188–200.

[163] Sing, K. S. W.; Everett, D. H.; Haul, R. A. W.; Moscou, L.; Pierotti, R. A.; Rouquerol, J.; Siemieniewska, T. *Pure and Applied Chemistry* **1985**, *57*, 603–619.

[164] Castner, D. G.; Watson, P. R.; Chan, I. Y. *Journal of Physical Chemistry* **1990**, *94*, 819–828.

[165] Natile, M. M.; Glisenti, A. *Chemistry of Materials* **2002**, *14*, 3090–3099.

[166] Okamoto, Y.; Nagata, K.; Adachi, T.; Imanaka, T.; Inamura, K. *Journal of Physical Chemistry* **1991**, *95*, 310–319.

[167] Mekki, A.; Holland, D.; Ziq, K.; McConville, C. F. *Journal of Non-Crystalline Solids* **1997**, *220*, 267–279.

[168] Walser, R. M.; Bene, R. W. *Applied Physics Letters* **1976**, *28*, 624–625.

[169] Novet, T.; Johnson, D. *Journal of the American Chemical Society* **1991**, *113*, 3398–3403.

[170] Patterson, A. L. *Physical Review* **1939**, *56*, 978–982.

[171] Al-Jishi, R.; Dresselhaus, G. *Physical Review B* **1982**, *26*, 4514–4522.

[172] Pannell, K. H.; Crawford, G. M. *Journal of Coordination Chemistry* **1973**, *2*, 251–256.

[173] Pettersen, R. C.; Cash, G. C. *Inorganica Chimica Acta* **1979**, *34*, 261–265.

[174] Carré, F.; Corriu, R.; Guerin, C.; Henner, B.; Kolani, B.; Wong Chi Man, W. *Journal of Organometallic Chemistry* **1987**, *328*, 15–34.

[175] Corriu, R. J. P.; Douglas, W. E.; Yang, Z. X. *Polymer* **1993**, *8*, 3535–3537.

[176] Dorman, J. L.; Fiorani, D.; Tronc, E. *Advances in Chemical Physics* **1997**, *98*, 283–494.

[177] Blundell, S. *Magnetism in Condensed Matter*; Oxford University Press Inc., 2001.

[178] Stoner, E. C.; Wohlfarth, E. P. *Philosophical Transactions of the Royal Society of London. Series A, Mathematical and Physical Sciences* **1948**, *240*, 599–642.

[179] Bonder, M. J.; Huang, Y. *Advanced Magnetic Nanostructures*; Springer, 2006.

[180] Bean, C. P.; Livingston, J. D. *Journal of Applied Physics* **1959**, *30*, 120–129.

[181] Leger, J. M.; Loriers-Susse, C.; Vodar, B. *Physical Review B* **1972**, *6*, 4250–4261.

[182] Skumryev, V.; Stoyanov, S.; Zhang, Y.; Hadjipanayis, G.; Givord, D.; Nogués, J. *Nature* **2003**, *423*, 850–853.

[183] G. Ertl, J. W., H. Knözinger *Preparation of Solid Catalysts*; Wiley, Weinheim, 1999.

[184] Thomas, R.; Moulijn, J. A. *Journal of Molecular Catalysis* **1980**, *8*, 161–174.

[185] Colton, R. J.; Guzman, A. M.; Rabalais, J. W. *Journal of Applied Physics* **1978**, *49*, 409–416.

[186] Patterson, T. A.; Carver, J. C.; Leyden, D. E.; Hercules, D. M. *The Journal of Physical Chemistry* **1976**, *80*, 1700–1708.

[187] Sarma, D. D.; Rao, C. N. R. *Journal of Electron Spectroscopy and Related Phenomena* **1980**, *20*, 25–45.

[188] Wagner, C. D.; Passoja, D. E.; Hillery, H. F.; Kinisky, T. G.; Six, H. A.; Jansen, W. T.; Taylor, J. A. *Journal of Vacuum Science and Technology* **1982**, *21*, 933–944.

[189] Brainard, W. A.; Wheeler, D. R. *Journal of Vacuum Science and Technology* **1978**, *15*, 1800–1805.

[190] Farges, F.; Siewert, R.; Brown, G. E.; Guesdon, A.; Morin, G. *The Canadian Mineralogist* **2006**, *44*, 731–753.

[191] Gajardo, P.; Pirotte, D.; Defosse, C.; Grange, P.; Delmon, B. *Journal of Electron Spectroscopy and Related Phenomena* **1979**, *17*, 121–135.

[192] Shaw, L.; Abbaschian, R. *Journal of Materials Science* **1995**, *30*, 5272–5280.

[193] Kim, K. S.; Winograd, N. *Surface Science* **1974**, *43*, 625–643.

[194] McIntyre, N. S.; Cook, M. G. *Analytical Chemistry* **1975**, *47*, 2208–2213.

[195] Cao, Y.; Nyborg, L.; Jelvestam, U. *Surface and Interface Analysis* **2009**, *41*, 471–483.

[196] Valeri, S.; del Pennino, U.; Sassaroli, P. *Surface Science* **1983**, *134*, L537–L542.

[197] Červený, L. *Catalytic Hydrogenation*; Elsevier, 1986.

[198] Chorkendorff, I.; Niemantsverdriet, J. W. *Concepts of Modern Catalysis and Kinetics, 2nd ed.*; Wiley, 2007.

[199] Haagen, J. *Industrial Catalysis*; Wiley, 2006.

[200] Beeck, O. *Reviews of Modern Physics* **1945**, *17*, 61–71.

[201] Horiuti, J.; Miyahara, K. *National Standard Reference Data Series-National Bureau of Standards 13* **1968**, 1–74.

[202] Keijsper de Han, D. J. A Study to Determine the Factors Controlling the MoS_2 Dispersion in Supported Catalysts. Ph.D. thesis, University Utrecht, 2008.

[203] Gates, B. C. *Advances in Catalysis, 1st ed., Vol. 51*; Elsevier, 2007.

[204] Perrin, D. D.; Armarego, W. L. F. *Purification of Laboratory Chemicals, 3rd ed.*; Pergamon Press, New York, 1988.

[205] Sheldrick, G. M. *Program for Empirical Absorption Correction of Area Detector Data*; University of Göttingen, Göttingen (Germany), 2008.

[206] Sheldrick, G. M. *Programs for Crystal Structure Determination*; University of Göttingen, Göttingen (Germany), 1997.

[207] Sheldrick, G. M. *Acta Crystallopgraphy* **2008**, *A64*, 112–122.

[208] Frisch, M. J.; Trucks, G. W.; Schlegel, H. B.; Scuseria, G. E.; Robb, M. A.; Cheeseman, J. R.; Montgomery, J. A., Jr.; Vreven, T.; Kudin, K. N.; Burant, J. C.; Millam, J. M.; Iyengar, S. S.; Tomasi, J.; Barone, V.; Mennucci, B.; Cossi, M.; Scalmani, G.; Rega, N.; Petersson, G. A.; Nakatsuji, H.; Hada, M.; Ehara, M.; Toyota, K.; Fukuda, R.; Hasegawa, J.; Ishida, M.; Nakajima, T.; Honda, Y.; Kitao, O.; Nakai, H.; Klene, M.; Li, X.; Knox, J. E.; Hratchian, H. P.; Cross, J. B.; Bakken, V.; Adamo, C.; Jaramillo, J.; Gomperts, R.; Stratmann, R. E.; Yazyev, O.; Austin, A. J.; Cammi, R.; Pomelli, C.; Ochterski, J. W.; Ayala, P. Y.; Morokuma, K.; Voth, G. A.; Salvador, P.; Dannenberg, J. J.; Zakrzewski, V. G.; Dapprich, S.; Daniels, A. D.; Strain, M. C.; Farkas, O.; Malick, D. K.; Rabuck, A. D.; Raghavachari, K.; Foresman, J. B.; Ortiz, J. V.; Cui, Q.; Baboul, A. G.; Clifford, S.; Cioslowski, J.; Stefanov, B. B.; Liu, G.; Liashenko, A.; Piskorz, P.; Komaromi, I.; Martin, R. L.; Fox, D. J.; Keith, T.; Al-Laham, M. A.; Peng, C. Y.; Nanayakkara, A.; Challacombe, M.; Gill, P. M. W.; Johnson, B.; Chen, W.; Wong, M. W.; Gonzalez, C.; Pople, J. A. Gaussian 03, Revision C.02. Gaussian, Inc., Wallingford, CT, 2004.

[209] Granovsky, A. A. PC GAMESS version 7.1. http://classic.chem.msu.su/gran/gamess/index.html.

[210] Becke, A. D. *Physical Review A* **1988**, *38*, 3098–3100.

[211] Lee, C.; Yang, W.; Parr, R. G. *Physical Review B* **1988**, *37*, 785–789.

[212] Mitin, A. V.; Baker, J.; Pulay, P. *The Journal of Chemical Physics* **2003**, *118*, 7775–7782.

[213] Schuchardt, K. L.; Didier, B. T.; Elsethagen, T.; Sun, L.; Gurumoorthi, V.; Chase, J.; Li, J.; Windus, T. L. *Journal of Chemical Information and Modeling* **2007**, *47*, 1045–1052.

[214] Stephens, P. J.; Devlin, F. J.; Chablowski, C. F.; Frisch, M. J. *Journal of Physical Chemistry* **1994**, *98*, 11623–11627.

[215] Schmidt, M. W.; Baldridge, K. K.; Boatz, J. A.; Elbert, S. T.; Gordon, M. S.; Jensen, J. H.; Koseki, S.; Matsunaga, N.; Nguyen, K. A.; Su, S.; Windus, T. L.; Dupuis, M. *Journal of Computational Chemistry* **1993**, *14*, 1347–1363.

[216] Miertus, S.; Scrocco, E.; Tomasi, J. *Chemical Physics* **1981**, *55*, 117–129.

[217] Becke, A. D. *Journal of Physical Chemistry* **1992**, *97*, 9173–9177.

[218] Perdew, J. P.; Wang, Y. *Physical Review B* **1992**, *45*, 13244–13249.

[219] Chesnut, D. B.; Moore, K. D. *Journal of Computational Chemistry* **1989**, *10*, 648–659.

[220] Chesnut, D.; Rusiloski, B.; Moore, K.; Egolf, D. *Journal of Computational Chemistry* **1993**, *14*, 1364–1375.

[221] Chesnut, D. *Chemical Physics* **1996**, *213*, 153–158.

[222] Hamprecht, F. A.; Cohen, A. J.; Tozer, D. J.; Handy, N. C. *The Journal of Chemical Physics* **1998**, *109*, 6264–6271.

[223] Staroverov, V. N.; Scuseria, G. E.; Tao, J.; Perdew, J. P. *Journal of Chemical Physics* **2003**, *119*, 12129–12137.

[224] Ni, Y.; Rulkens, R.; Pudelski, J.; Manners, I. *Makromolekulare Chemie - Rapid Communications* **1995**, *16*, 637–638.

[225] Corriu, R. J. P.; Guerin, C.; Henner, B.; Kuhlmann, T.; Jean, A. *Chemistry of Materials* **1990**, *2*, 351–352.

[226] Bryan, W. E.; Kerby, M. C.; Haushalter, R. C.; Vollhardt, K. P. C. *Inorganic Chemistry* **1990**, *29*, 723–728.

[227] Chrusciel, J. J. C. *Polymer* **2005**, *516*, 508–516.

[228] Schraml, J.; Chvalovsky, V.; Magi, M.; Lippmaa, E. *Collection of Czechoslovak Chemical Communications* **1979**, *44*, 854–865.

[229] Schraml, J.; Chvalovsky, V.; Magi, M.; Lippmaa, E. *Collection of Czechoslovak Chemical Communications* **1978**, *43*, 3365–3372.

[230] Seyferth, D.; Annarelli, D. C.; Vick, S. C.; Duncan, D. P. *Journal of Organometallic Chemistry* **1980**, *201*, 179–195.

[231] Krapivin, A. M. *Izvestiya Akademii Nauk SSSR, Seriya Khimicheskaya* **1980**, *7*, 1950–1951.

[232] Schraml, J.; Pola, J.; Jancke, H.; Engelhardt, G.; Cerny, M.; Chvalovsky, V. *Collection of Czechoslovak Chemical Communications* **1976**, *41*, 360–367.

[233] Schraml, J. *Collection of Czechoslovak Chemical Communications* **1981**, *46*, 377–390.

[234] Pestunovich, V. A.; Tandura, S. N.; Voronkov, M. G.; Engelhardt, G.; Lippmaa, E.; Pehk, T.; Sidorkin, V. F.; Zelcans, G.; Baryshok, V. P. *Doklady Akademii Nauk SSSR* **1978**, *240*, 914–917.

[235] van den Ancker, T. R.; Raston, C. L.; Skelton, B. W.; White, A. H. *Organometallics* **2000**, *19*, 4437–4444.

[236] Gómez, E.; Santes, V.; de La Luz, V.; Farfan, N. *Journal of Organometallic Chemistry* **1999**, *590*, 237–241.

[237] Gómez, E.; Santes, V.; de La Luz, V.; Farfan, N. *Journal of Organometallic Chemistry* **2001**, *622*, 54–60.

[238] Voronkov, M. G.; Trofimova, O. M.; Chernov, N. F.; Bolgova, Y. I.; Albanov, A. I.; Chipanina, N. N.; Zelbst, E. A. *Heteroatom Chemistry* **2006**, *17*, 567–571.

[239] Gómez, E.; Hernandez, Z.; Alvarez-Toledano, C.; Toscano, R. A.; Santes, V.; Sharma, P. *Journal of Organometallic Chemistry* **2002**, *648*, 280–287.

[240] Kummer, D.; Abdel Halim, S. H. *Journal of Organometallic Chemistry* **1993**, *446*, 51–65.

[241] Prakasha, T. K.; Chandrasekaran, A.; Day, R. O.; Holmes, R. R. *Inorganic Chemistry* **1996**, *35*, 4342–4346.

[242] Edema, J. J.; Libbers, R.; Ridder, A.; Kellogg, R. M.; Spek, A. L. *Journal of Organometallic Chemistry* **1994**, *464*, 127–131.

[243] Wagler, J.; Bohme, U.; Brendler, E.; Thomas, B.; Goutal, S.; Mayr, H.; Kempf, B.; Remennikov, G.; Roewer, G. *Inorganica Chimica Acta* **2005**, *358*, 4270–4286.

[244] Yang, J.; Verkade, J. *Journal of Organometallic Chemistry* **2002**, *651*, 15–21.

[245] Kalikhman, I.; Gostevskii, B.; Girshberg, O.; Sivaramakrishna, A.; Kocher, N.; Stalke, D.; Kost, D. *Journal of Organometallic Chemistry* **2003**, *686*, 202–214.

[246] Nakash, M.; Goldvaser, M.; Goldberg, I. *Inorganic Chemistry* **2004**, *43*, 5792–5794.

[247] Filippou, A. C.; Portius, P.; Schnakenburg, G. *Journal of the American Chemical Society* **2002**, *124*, 12396–12397.

[248] Kost, D.; Kingston, V.; Gostevskii, B.; Ellern, A.; Stalke, D.; Walfort, B.; Kalikhman, I. *Organometallics* **2002**, *21*, 2293–2305.

[249] Kalikhman, I.; Kingston, V.; Girshberg, O.; Kost, D. *Organometallics* **2001**, *20*, 4713–4720.

[250] González-García, G.; Alvarez, E.; Marcos-Fernández, A.; Gutiérrez, J. A. *Inorganic Chemistry* **2009**, *48*, 4231–4238.

[251] Fester, G. W.; Wagler, J.; Brendler, E.; Böhme, U.; Gerlach, D.; Kroke, E. *Journal of the American Chemical Society* **2009**, *131*, 6855–6864.